nature materials

ARTICLES

PUBLISHED ONLINE: 8 DECEMBER 2013 | DOI: 10.1038/NMAT3819

A nanoparticle-based strategy for the imaging of a broad range of tumours by nonlinear amplification of microenvironment signals

Yiguang Wang[1], Kejin Zhou[1], Gang Huang[1], Christopher Hensley[2], Xiaonan Huang[1], Xinpeng Ma[1], Tian Zhao[1], Baran D. Sumer[3], Ralph J. DeBerardinis[2] and Jinming Gao[1]*

Stimuli-responsive nanomaterials are increasingly important in a variety of applications such as biosensing, molecular imaging, drug delivery and tissue engineering. For cancer detection, a paramount challenge still exists in the search for methods that can illuminate tumours universally regardless of their genotypes and phenotypes. Here we capitalized on the acidic, angiogenic tumour microenvironment to achieve the detection of tumour tissues in a wide variety of mouse cancer models. This was accomplished using ultra pH-sensitive fluorescent nanoprobes that have tunable, exponential fluorescence activation on encountering subtle, physiologically relevant pH transitions. These nanoprobes were silent in the circulation, and then strongly activated (>300-fold) in response to the neovasculature or to the low extracellular pH in tumours. Thus, we have established non-toxic, fluorescent nanoreporters that can nonlinearly amplify tumour microenvironmental signals, permitting the identification of tumour tissue independently of histological type or driver mutation, and detection of acute treatment responses much more rapidly than conventional imaging approaches.

Responsive polymer materials are of great interest and importance in a variety of optical, electrical, thermal and mechanical systems in a wide range of applications such as sensing, adaptable surface adhesion, self-healing and drug delivery[1,2]. In biology and medicine, high-performance and bioresponsive materials that can respond and, furthermore, amplify pathophysiological signals have shown great promise to differentiate diseased and healthy tissues, a major challenge in any diagnostic or therapeutic applications[3,4]. In tumour visualization, a variety of nanomaterials have been reported with functionalities in fluorescence, Raman imaging, magnetic resonance imaging and photoacoustics[5–9]. Compared with small molecular tracers, one of the main advantages of nanoprobes is the ultrasensitive detection at nanomolar–picomolar particle concentrations[7,8]. Although this increased sensitivity improves the physical detection limit, achieving high biological specificity to differentiate tumours from normal tissues remains a significant challenge. Many present cancer imaging agents target cancer-cell-specific biomarkers such as Her2/neu, EGFR, and folate receptors to achieve specificity[10–12]. Despite reports of successful imaging outcomes that stratify patients towards personalized therapy, broad tumour applicability in a wide range of cancers is often not possible as cancer-cell-specific biomarkers are frequently expressed in only a subset of patients (for example, <25% of breast cancer patients have Her2/neu expression)[13,14]. In addition, antibody–dye conjugates require a long clearance time (for example, >24 h) owing to the persistent blood circulation of humanized antibody and the high blood background from the always-ON mode of probe design.

In this study, we report a nonlinear signal amplification strategy to greatly increase the detection accuracy of pathophysiological signals of the tumour microenvironment to achieve a broad specificity of tumour visualization (Fig. 1). We chose two established tumour microenvironment signals, namely angiogenic tumour vasculature[15,16] and low extracellular pH (pH_e; ref. 17), to demonstrate the proof of principle. Tumour angiogenesis and aerobic glycolysis (also known as the Warburg effect) are recognized hallmarks of cancer, which are ubiquitous in solid tumours, regardless of cancer type.

To accomplish this goal, we established a series of ultra pH-sensitive (UPS) nanoprobes to specifically image the tumour extracellular milieu and angiogenic tumour vessels. The UPS platform is comprised of three independently controlled functional components. The first component is an ultra pH-sensitive core that renders a tunable sharp pH response ($\Delta pH_{ON/OFF} < 0.25$ (ref. 18), as compared with 2 pH units for small molecular pH sensors). This unique hydrophobic micellization-induced nanoscale phenomenon is essential for imaging acidic tumour pH_e (6.5–6.8; ref. 17), which is not markedly different from blood pH (7.4). Many previously reported pH-sensitive nanosystems do not have a sharp response in this pH range and in many cases take a long time (for example, 24 h) to respond[19–23]. The second component is a series of fluorophores (for example, tetramethyl rhodamine (TMR) and cyanine (Cy) family dyes) with a large emission range from green to near-infrared (500–820 nm). Homo-fluorescence resonance energy transfer (homoFRET)-induced fluorescence quenching results in large fluorescence decrease, crucial for suppressing blood signals and for achieving nonlinear amplification of signals in the tumour. The multicoloured design also allows simultaneous imaging of multiple tumour targets in space and time. The third component is a targeting unit

[1]Department of Pharmacology, Simmons Comprehensive Cancer Center, University of Texas Southwestern Medical Center, 5323 Harry Hines Boulevard, Dallas, Texas 75390, USA, [2]Children's Medical Center Research Institute, University of Texas Southwestern Medical Center, 5323 Harry Hines Boulevard, Dallas, Texas 75390, USA, [3]Department of Otolaryngology, University of Texas Southwestern Medical Center, 5323 Harry Hines Boulevard, Dallas, Texas 75390, USA. *e-mail: jinming.gao@utsouthwestern.edu

© 2013 Macmillan Publishers Limited. All rights reserved.

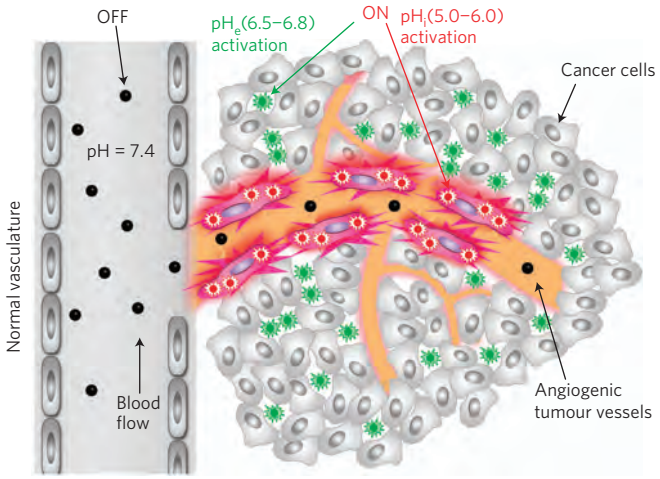

Figure 1 | A schematic of imaging the tumour microenvironment using UPS nanoprobes. The UPS nanoprobes stay 'OFF' at pH 7.4 during blood circulation. After reaching tumours, the UPS nanoprobes are turned ON by acidic extracellular pH$_e$ (6.5–6.8) in the tumour milieu, or endocytic organelles (pH$_i$, 5.0–6.0) in the tumour endothelial cells after receptor-mediated endocytosis.

(for example, Arg-Gly-Asp; RGD), which binds to cell surface receptors and internalizes nanoprobes to allow signal amplification in acidic endocytic organelles. Our present UPS nanoprobes carry ~1,600 dye molecules per micelle[24]. Assuming that it takes 10 $\alpha_v\beta_3$ integrins to internalize one micelle, this represents >100-fold dye payload amplification on a per $\alpha_v\beta_3$ basis. Consequently, we demonstrate a broad tumour specificity with a large tumour-to-blood ratio (>300-fold) in a diverse set of animal tumour models with different cancer types and organ sites. Tumour-specific imaging was accomplished in the first hour after intravenous nanoprobe injection and in tumours as small as 1 mm^3. These capabilities, together with the broad cancer specificity, make the present strategy particularly powerful in image-guided resection of tumours and post-therapy monitoring of drug efficacy.

We first performed a series of experiments to systematically investigate the influence of pH-sensitive segment and dye content on the performance of the nanoprobes (detailed results are summarized in Supplementary Tables 1–3 and Fig. 1). On the basis of these data, we selected UPS compositions that meet the following criteria: sharp pH transition ($\Delta pH_{10-90\%} < 0.25$), large fluorescence ON/OFF ratio, high reproducibility, low critical micelle concentration, relatively small particle size (<30 nm) to allow tumour tissue penetration, and optimal pH transitions.

To distinguish the small pH differences between acidic tumour pH$_e$ (6.5–6.8; ref. 17) and blood (7.4), we synthesized an extracellular pH-activatable (UPS$_e$) nanoprobe from the poly(ethylene glycol)-b-poly(2-(hexamethyleneimino)ethyl methacrylate) copolymer (Fig. 2a and Supplementary Table 4). A near-infrared dye, Cy5.5 ($\lambda_{ex}/\lambda_{em}$ = 675/710 nm), was conjugated to the ionizable block of the copolymer (Supplementary Scheme 1). The UPS$_e$ nanoprobe had a pH transition at 6.9 and a sharp pH response ($\Delta pH_{10-90\%}$, the pH difference between 10 to 90% fluorescence activation was 0.23). The fluorescence activation ratio (R_F) was 102-fold between pH 6.7 and 7.4. In contrast, a theoretical calculation based on the Henderson–Hasselbach equation for a small molecular pH sensor (pK_a = 6.9) yielded only 2.6-fold fluorescence increase in this pH range (Fig. 2b). At blood pH, UPS$_e$ nanoprobes were present as self-assembled micelles with a diameter of 25.3 ± 1.5 nm and a spherical morphology (left panel, Fig. 2d). HomoFRET-induced fluorescence quenching was responsible for complete silencing of the fluorophores in the micelle state (Fig. 2c)[24]. Micelle dissociation at acidic pH$_e$ (right panel, Fig. 2d) resulted in a marked increase in fluorescence signals (Fig. 2c,e).

To achieve selective activation in the acidic endocytic organelles (for example, endosomes and lysosomes, pH = 5.0–6.0), we established an intracellular pH-activatable (UPS$_i$) nanoprobe from the poly(ethylene glycol)-b-poly(2-(diisopropyl amino)ethyl methacrylate) copolymer (Fig. 2a). For imaging of $\alpha_v\beta_3$-expressing angiogenic tumour endothelial cells, we functionalized the UPS$_i$ surface with 10% cRGDfK (cyclic RGD (cRGD)) peptide through thiol–maleimide linkage (Supplementary Scheme 2 and Fig. 2). The cRGD-UPS$_i$ nanoprobe had a pH transition at 6.2 with a $\Delta pH_{10-90\%}$ value of 0.21. The fluorescence ON/OFF activation ratio was 128-fold (Supplementary Table 4). The cRGD-encoded UPS$_i$ nanoprobes (24.5 ± 1.1 nm) were stable at blood pH and acidic tumour pH$_e$, but can be selectively activated inside the lysosomes of tumour endothelial cells on receptor-mediated endocytosis (see data below). Both UPS$_e$ and UPS$_i$ nanoprobes were stable in freshly prepared mouse serum as indicated by the negligible change in fluorescence intensity over 24 h incubation (Fig. 2e and Supplementary Fig. 2e).

To investigate whether UPS dilution (for example, in blood after injection) affects the pH response, we examined the concentration dependence of UPS$_e$/UPS$_i$ properties (Supplementary Fig. 3). For UPS$_e$ and UPS$_i$, the plasma concentrations 24 h after intravenous injection are approximately 15 and 100 μg ml^{-1}, respectively (calculated from the 10 mg kg^{-1} injection dose and micelle pharmacokinetics). Data show that fluorescence intensity in the ON state (lower pH) decreased at lower probe concentrations as expected; however, the R_F values remained high (>60-fold) even at 10 μg ml^{-1}. Normalization of fluorescence signals showed superimposable, sharp pH transitions, indicating high fidelity of UPS$_i$/UPS$_e$ in the physiologically relevant concentration range.

A three-dimensional plot of fluorescence intensity versus probe concentration and pH illustrates the pH-modulated signal amplification/suppression strategy orthogonal to probe concentration (Supplementary Fig. 4). Along the concentration axis, higher probe concentration results in larger fluorescence signals (tumour accumulation is still a prerequisite of achieving UPS signals). Along the pH axis, homoFRET-induced quenching abolished fluorescence signals at the normal tissue or blood pH (7.2–7.4). On reaching the targeted pH environments, UPS probes are activated, leading to exponentially increased signals.

To investigate the specificity of UPS$_e$ nanoprobes for pH$_e$ imaging, we first evaluated two inhibitors of tumour glycolysis and examined their effects on extracellular pH in cell culture. The first agent, 2-deoxy-D-glucose (2-DG), competitively inhibits glucose uptake through cell surface glucose transporters and subsequent phosphorylation by hexokinases; the second agent, α-cyano-4-hydroxycinnamate (CHC), is a suicide inhibitor of monocarboxylate transporter that prevents the secretion of lactic acid from cancer cells (Fig. 3a)[25]. *In vitro* cell culture experiments show that both agents significantly decreased lactate secretion in A549 lung cancer cells (Fig. 3b). Moreover, we also observed that 2-DG and CHC treatment retarded the acidification of cell culture medium (ΔpH was 0.41, 0.17 and 0.16 for vehicle, 2-DG and CHC, respectively. Fig. 3c).

For *in vivo* tumour imaging studies, UPS$_e$ nanoprobes (10 mg kg^{-1}) were injected intravenously into mice bearing subcutaneous A549 lung cancer xenografts (n = 4 for each group). For glycolysis inhibition control, 2-DG or CHC (250 mg kg^{-1}) was injected 12 h before the UPS$_e$ administration. An always-ON nanoprobe control with the same particle size and core composition, but no pH-sensitive fluorescence response, was also used (see Supplementary Fig. 5 for detailed description). As early as the first hour after UPS$_e$ injection, a significant tumour contrast (tumour/normal tissue ratio ~4, $P < 0.05$ compared with the three other controls)

© 2013 Macmillan Publishers Limited. All rights reserved.

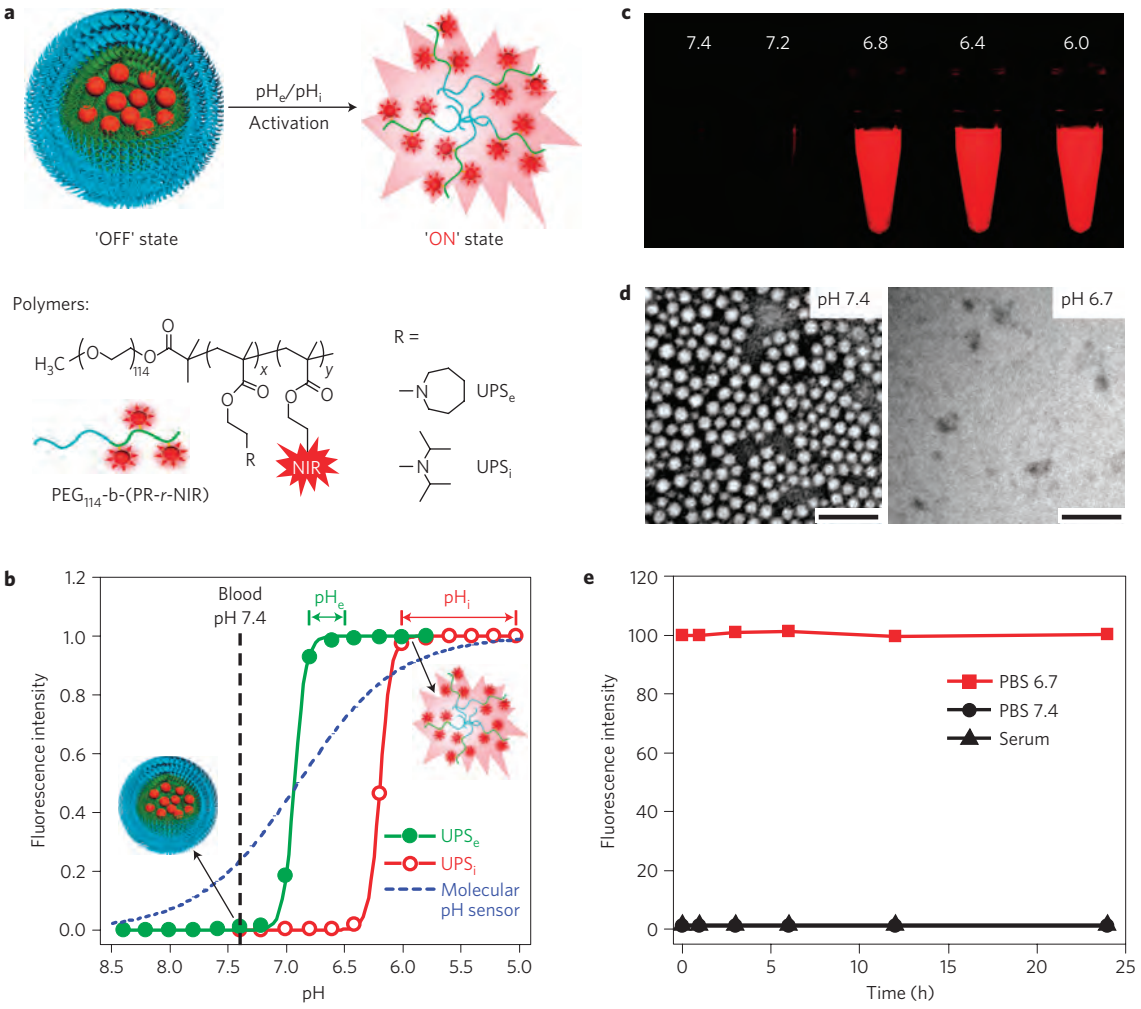

Figure 2 | Synthesis and characterization of UPS nanoprobes. a, Structural composition of two types of nanoprobe, UPS_e and UPS_i, with pH transitions at 6.9 and 6.2, respectively. The UPS_e is specifically designed to activate in acidic tumour extracellular fluid ($pH_e = 6.5$–6.8). The UPS_i can be activated inside acidic endocytic organelles (for example $pH_i = 5.0$–6.0). Cy5.5 is used as the near-infrared fluorophore in most of the animal studies. **b**, Normalized fluorescence intensity as a function of pH for UPS_e and UPS_i nanoprobes. At high pH (for example, 7.4), both probes stay silent. At pH below their transitions (that is 6.9 and 6.2), the nanoprobes can be activated as a result of micelle dissociation. The blue dashed line simulates the pH response of a small molecular pH sensor with a pK_a of 6.9 based on the Henderson–Hasselbach equation. For UPS, the pH response ($\Delta pH_{10-90\%}$) is extremely sharp (<0.25 pH unit between ON/OFF states) with >100-fold signal amplification. In contrast, small molecular pH sensors require 3 pH units for a comparable signal change. **c**, Fluorescent images of UPS_e–Cy5.5 nanoprobe solution in different pH buffers ($\lambda_{ex}/\lambda_{em} = 675/710$ nm). **d**, Transmission electron micrographs of UPS_e nanoprobes at pH 7.4 and 6.7 (polymer concentration, 1 mg ml^{-1}; scale bars, 100 nm). **e**, UPS_e nanoprobes remain stable in fresh mouse serum over 24 h at 37 °C.

was observed (Fig. 3e). Over 24 h, fluorescence signals in the UPS_e group increased considerably whereas the signals from control groups remained relatively unchanged. The near-infrared fluorescence intensity in the tumour increased 10.9 ± 1.7-fold from 5 min to 24 h. The always-ON nanoprobe control showed highly elevated fluorescence background in normal tissues and low tumour/tissue contrast (<1.2-fold over 24 h, Supplementary Fig. 6), which suggest that the enhanced permeability and retention effect[26] alone is not sufficient to yield high tumour contrast. Pretreatment with metabolic inhibitors resulted in significant signal decrease in tumours compared with UPS_e alone (for example, 2.3 ± 0.7-fold decrease for 2-DG ($P = 0.004$), and 3.2 ± 0.6-fold for CHC ($P = 0.007$)). After 24 h, the mice were euthanized and the excised organs were imaged (Supplementary Fig. 7). The fluorescence signal of each organ/tissue was normalized over the nanoprobe dose in the corresponding tissue as measured by ^{3}H-labelled nanoparticles. The value was further normalized to blood to yield the organ to blood ratio (OBR; Supplementary Table 5). A549 tumour had a large OBR (355; Fig. 3f), demonstrating the effectiveness of signal amplification in tumours and background suppression in blood. These data strongly support the hypothesis that UPS_e nanoprobes can specifically detect acidic tumour pH_e, and that the probes can sense metabolic alterations within 24 h after initiating therapy.

Immunostaining of the whole-mount tumour sections (Fig. 3g) showed a qualitative correlation between the UPS_e signal (red) with the hypoxia stain by pimonidazole, which agrees with previous reports that hypoxic regions of the tumours are more acidic[27]. The nanoprobe activation map extended beyond the region of hypoxia detected by pimonidazole, probably because low pH, particularly <6.8, significantly reduces pimonidazole binding to cancer cells[28]. Interestingly, the UPS_e signal did not correlate as well with the tumour vascular density (CD31 stain, mostly at tumour periphery) or the cell proliferation marker Ki-67 (Supplementary Fig. 8).

For specific imaging of angiogenic tumour vasculature, we constructed cRGD-encoded UPS_i nanoprobes (cRGD-UPS_i, Fig. 4a) to image $\alpha_v\beta_3$ integrins, an established angiogenic biomarker. cRGD

© 2013 Macmillan Publishers Limited. All rights reserved.

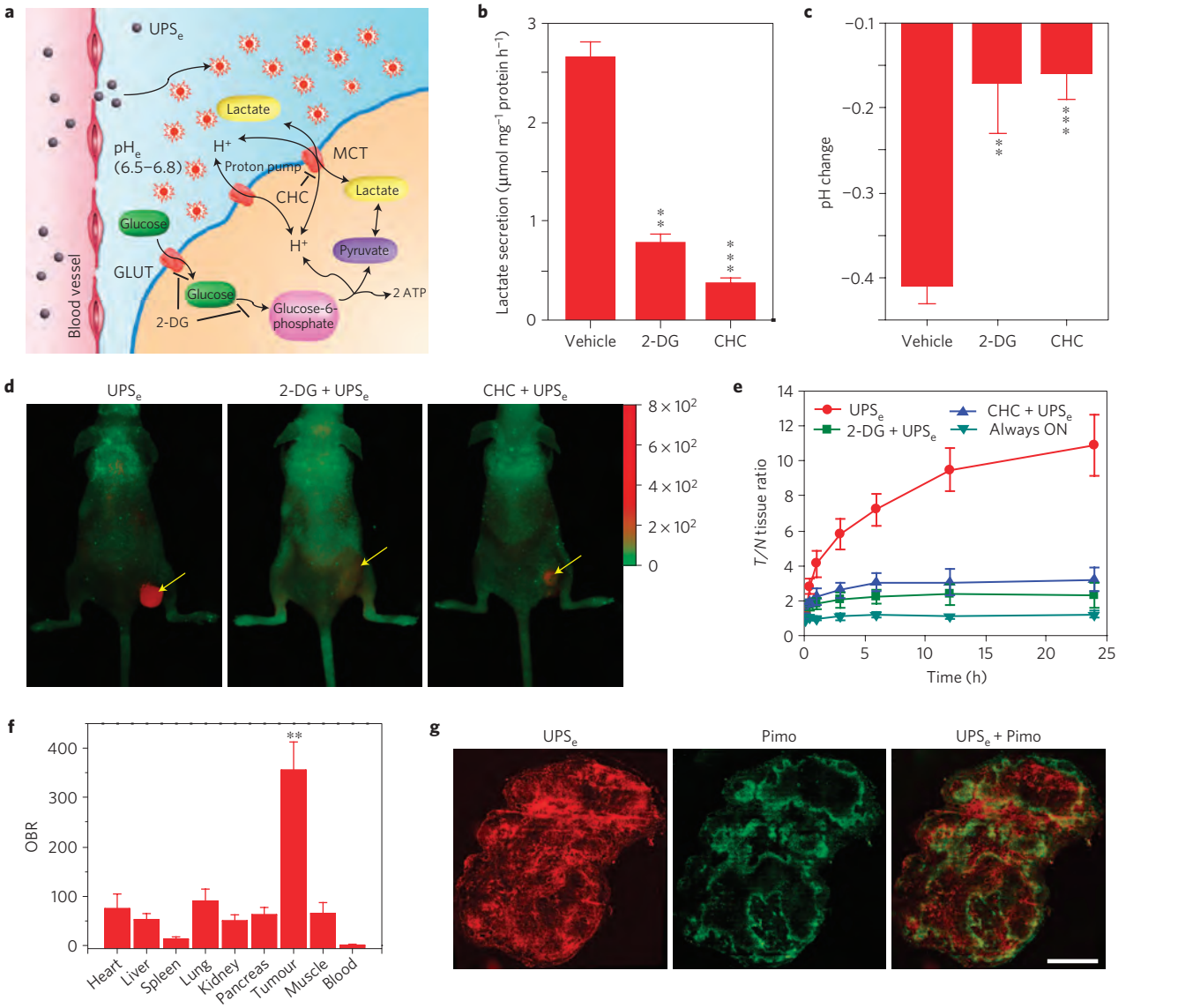

Figure 3 | UPS_e nanoprobes can specifically image acidic tumour pH_e. **a**, Aerobic glycolysis converts glucose to lactate in cancer cells. 2-DG and CHC are metabolic inhibitors for glucose uptake and lactic acid secretion, respectively. GLUT, glucose transporter; MCT, monocarboxylate transporter. **b**, Effect of 2-DG or CHC on the rate of lactic acid secretion in A549 cells. **c**, Acidification of A549 cell culture medium in the presence of 2-DG or CHC after 6 h incubation ($n = 4$). $^{**}P < 0.01$, $^{***}P < 0.001$, compared with the vehicle group. **d**, Overlaid fluorescent images of A549-tumour-bearing mice at 24 h post-injection of UPS_e nanoprobes (10 mg kg^{-1}). In the control groups, 2-DG (250 mg kg^{-1}) or CHC (250 mg kg^{-1}) was injected 12 h before UPS_e nanoprobe administration. Cy5.5 (red) and autofluorescence (green) are separately shown in the composite images. Yellow arrows indicate the tumour location. **e**, Near-infrared fluorescence intensity ratio between tumour and normal tissues (T/N ratio) as a function of time after UPS_e injection. Data are presented as mean ± s.d. ($n = 4$). **f**, OBRs (see data in Supplementary Table 5) 24 h post-injection of UPS_e ($n = 4$). A549 tumour has a 355-fold signal amplification over blood by UPS_e. $^{**}P < 0.01$, compared with other organs. **g**, Hypoxia bands qualitatively correlate with activation pattern of UPS_e in A549 tumour xenograft. Whole-mount images of tumour slices stained for hypoxia (green). All images were obtained from the adjacent sections at ×200 magnification. Scale bar, 2 mm.

peptides bind to $\alpha_v\beta_3$ integrins, resulting in receptor-mediated endocytosis and uptake into the acidic endocytic organelles (Fig. 4b). Human umbilical vein endothelial cells were treated with cRGD-UPS_i, cRGD-free UPS_i (UPS_i), and a 50-fold molar excess of free cRGD peptide followed by cRGD-UPS_i nanoprobes to demonstrate the proof of concept. As the nanoprobes were 'silent' in cell culture medium, we can directly measure the kinetics of nanoprobe internalization and activation without removing the medium. Thirty minutes after cRGD-UPS_i incubation, punctate fluorescence activation was observed inside the human umbilical vein endothelial cells. At 3 h, an 11-fold fluorescence increase in the cRGD-UPS_i group was observed over the UPS_i and cRGD competition control groups (Supplementary Fig. 9). Almost all of the fluorescent punctates in cells treated with cRGD-UPS_i colocalized with LysoTracker (Supplementary Fig. 10), demonstrating that cRGD-UPS_i nanoprobes became activated in the endosomes/lysosomes. Finally, A549 and MCF-7 cells with low $\alpha_v\beta_3$ expression levels showed significantly reduced fluorescence signals after incubation with cRGD-UPS_i (Supplementary Fig. 11).

For *in vivo* tumour imaging studies, cRGD-UPS_i, UPS_i and cRGD-encoded always-ON nanoprobes were injected intravenously into A549 tumour-bearing mice ($n = 4$). As an additional control, a blocking dose of cRGD peptide (25 mg kg^{-1}) was injected 30 min before the cRGD-UPS_i administration. As early as 30 min

© 2013 Macmillan Publishers Limited. All rights reserved.

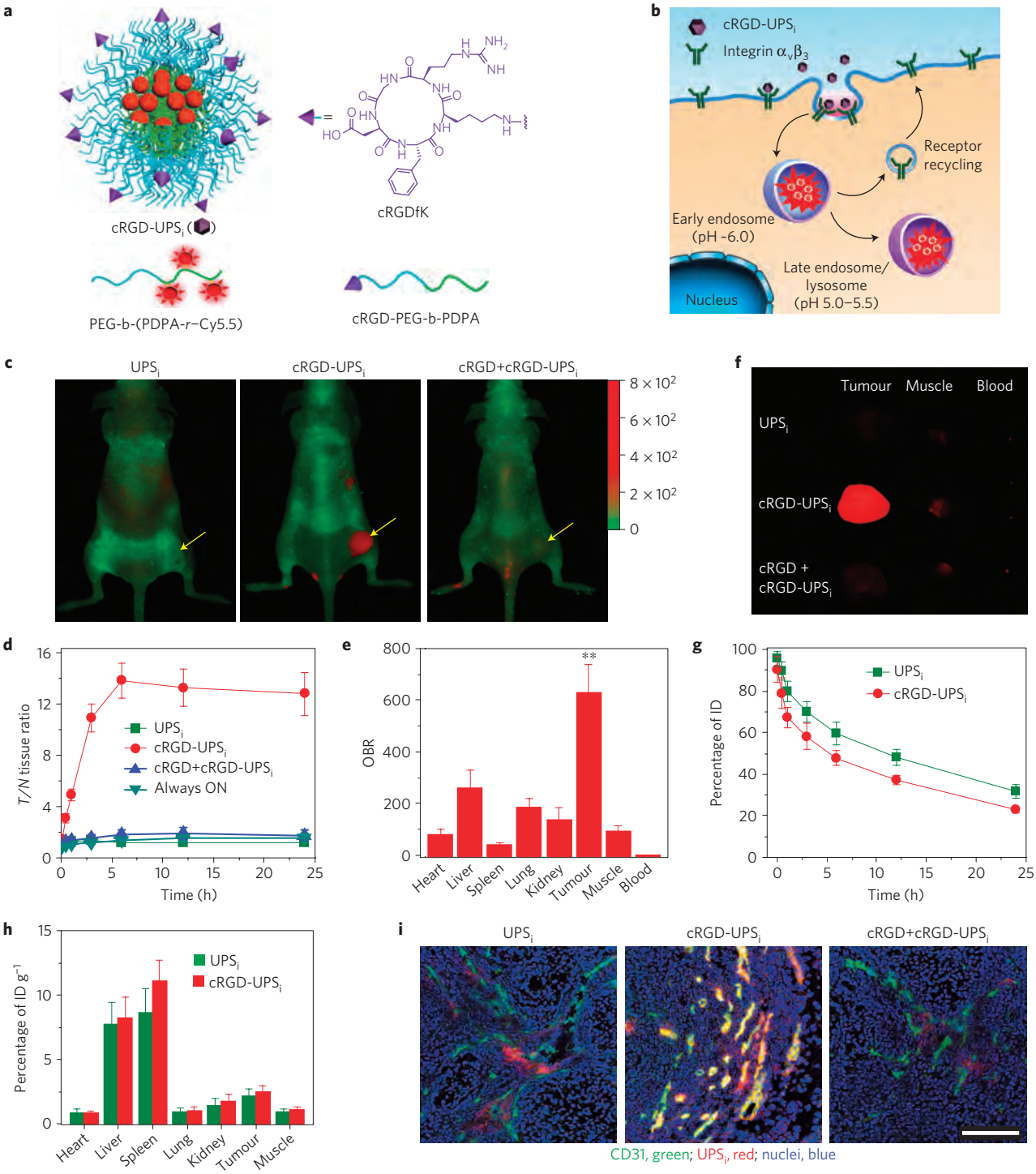

Figure 4 | cRGD-UPS$_i$ nanoprobes can specifically image angiogenic tumour vasculature. a, Design of the cRGD-UPS$_i$ nanoprobe. **b**, Schematic of internalization and activation of cRGD-UPS$_i$ nanoprobes after $\alpha_v\beta_3$-mediated endocytosis in tumour endothelial cells. The nanoprobes are accumulated in the endosomes or lysosomes, where the acidic pH activates the nanoprobes. **c**, Superimposed fluorescent images of A549-tumour-bearing mice at 6 h post-injection of cRGD-UPS$_i$ or UPS$_i$ nanoprobe (10 mg kg^{-1}). In the competition group, a blocking dose of cRGD peptide (25 mg kg^{-1}) was injected 30 min before cRGD-UPS$_i$ administration. Cy5.5 (red) and autofluorescence (green) are separately shown in the composite images. **d**, T/N ratio after injection of nanoprobes as a function of time. Data are presented as mean ± s.d. ($n = 4$). **e**, OBRs (see data in Supplementary Table 7) 6 h post-injection of cRGD-UPS$_i$ nanoprobe ($n = 4$). A549 tumour has a 628-fold signal amplification over blood by cRGD-UPS$_i$. $^{**}P < 0.01$, compared with other organs. **f**, Representative images of *ex vivo* tumours, muscles and blood at 6 h post-injection of nanoprobes. **g**, Plasma concentration versus time curves ($n = 4$) for cRGD-UPS$_i$ and UPS$_i$ nanoprobes. **h**, Biodistribution profiles ($n = 4$) of cRGD-UPS$_i$ and UPS$_i$ nanoprobes 6 h after intravenous injection. **i**, Correlation of nanoprobe activation with tumour vasculature (anti-CD31). The co-localization between nanoprobe and tumour vasculature is indicated by the yellow colour in the merged images (green, blood vessels; red, nanoprobes; blue, nuclei. Scale bar, 100 μm). The error bars in **e**,**g**,**h** were calculated as the standard deviations from four replicate experiments.

© 2013 Macmillan Publishers Limited. All rights reserved.

post-injection, the cRGD-UPS$_i$ group produced significantly higher fluorescence contrast in tumours (T/N ratio ~3) than the control groups (~1, $P < 0.05$, Fig. 4d and Supplementary Fig. 12). The fluorescence contrast reached a maximum at 6 h post-injection ($T/N \sim 14$). UPS$_i$, cRGD-always-ON and free cRGD competition controls had minimal fluorescence increase in the tumour over the 6 h span (<2-fold). The OBR value was 628 for cRGD-UPS$_i$ in tumours, which is significantly higher than other organs/tissues (Fig. 4e). Despite comparable tumour accumulation percentages (for example, 2.49 ± 0.44% versus 2.11 ± 0.59% injected dose per gram (ID g^{-1}) for cRGD-UPS$_i$ and UPS$_i$ 6 h post-injection, respectively. Fig. 4h), the OBR value was significantly smaller for the UPS$_i$ control (78, $P < 0.01$. Supplementary Table 6 and Fig. 13). This difference (628 versus 78) confirms that cell internalization is primarily responsible for the larger OBR for cRGD-UPS$_i$. The always-ON nanoprobe control showed strong fluorescence background and low tumour/tissue contrast (<1.6-fold over 24 h, Supplementary Fig. 14). The strategy of signal amplification by the cRGD-UPS$_i$ nanoprobes in angiogenic tumour vasculature was more markedly illustrated when compared with a small molecular cRGD–IRDye 800CW conjugate, where a maximum of 2-fold T/N ratio was observed in the 24 h span (Supplementary Fig. 15).

We performed immunostaining of tumour sections (Fig. 4i and Supplementary Fig. 16) to verify the locations of cRGD-UPS$_i$ activation. Tumour vessels were stained with Alexa Fluor 488-labelled anti-CD31. For cRGD-UPS$_i$, most nanoprobe activation was found to colocalize with tumour vasculature (yellow colour in Fig. 4i). In contrast, low levels of nanoprobe activation were observed in the UPS$_i$ and free cRGD blocking control groups. In these tumour sections, sporadic spots of nanoprobe activation were found outside the tumour vasculature, suggesting that non-vascular cells may also pick up a small population of nanoprobes through $\alpha_v\beta_3$-independent pathways.

To characterize the pharmacokinetics and biodistribution of UPS$_e$/UPS$_i$ nanoprobes, we synthesized ^{3}H-labelled nanoprobes through acetylation (−COCT$_3$) of the free amino groups in the corresponding copolymers. ^{3}H-labelled UPS$_e$, cRGD-UPS$_i$ and UPS$_i$ nanoprobes were injected at the same dose (10 mg kg^{-1}, or 2.0 mCi kg^{-1}) as in imaging studies ($n = 5$). For all three compositions, plasma concentration–time curves showed a two-phase behaviour over 24 h (Fig. 4g and Supplementary Fig. 17). The α-phase half-lives ($t_{1/2,\alpha}$) were 1.0 ± 0.2, 2.3 ± 0.5 and 4.3 ± 0.7 h for UPS$_e$, cRGD-UPS$_i$ and UPS$_i$, respectively. The β-phase half-lives ($t_{1/2,\beta}$) were 7.5 ± 0.3, 17.0 ± 1.8 and 19.6 ± 2.1 h for UPS$_e$, cRGD-UPS$_i$ and UPS$_i$, respectively. The faster clearance of UPS$_e$ may be a result of higher critical micelle concentration (2.38 μg ml^{-1}) than that of the UPS$_i$ (1.32 μg ml^{-1}). Between the two UPS$_i$ probes, cRGD surface functionalization resulted in decreased blood half-lives, consistent with other cRGD-encoded nanoparticle systems[29].

Biodistribution studies show that tumour uptake (2–3% ID g^{-1} tissue) of UPS$_e$/UPS$_i$ nanoparticles was higher than most normal tissues (heart, lung, kidney and muscle; Supplementary Tables 5–7). Meanwhile, the reticuloendothelial system (RES; that is, liver and spleen) was responsible for the uptake of most of the nanoprobes. Interestingly, for both UPS$_i$ groups, higher uptake was observed in the spleen than the liver; however, probe activation was much greater in the liver than spleen (for example, OBR >250 in liver whereas <50 in spleen 6 h post-injection). To help understand this discrepancy, we co-injected a mixture of always-ON nanoprobe (labelled with Cy3) and UPS$_i$ (Cy5.5) with the anticipation of using the always-ON probe to benchmark the tissue distribution of nanoparticles regardless of tissue environment, whereas the UPS$_i$ probe shows signals arising from cell uptake in these organs. The results were striking (Supplementary Fig. 18). First, UPS$_i$ activation occurred only sporadically in cell punctates (most likely spleen macrophages)[30] in the red pulps of the spleen but was largely absent in the white pulps. In contrast, the always-ON probes showed widespread distributions in both pulps. In the liver, we observed UPS$_i$ activation in most hepatocytes. This surprising combination (that is, lack of nanoprobe activation in a major spleen component and unexpected activation in most liver hepatocytes) explains the divergent behaviours of UPS$_i$ in these two organs. Further studies are warranted to further elucidate the mechanism of unexpected patterns of cell uptake in these organs.

To evaluate nanoprobe toxicity, we investigated the changes in animal body weight, liver and kidney functions, and histology of the RES at 24 h and 7 d after nanoprobe injection (10 mg kg^{-1}). The results showed no weight loss, statistically insignificant changes of hepatic and kidney functions (for example, aspartate transaminase and glutamic oxaloacetic transaminase; Supplementary Fig. 19) and normal RES histology (data not shown), demonstrating the safety of these nanoparticles.

To explore the potential synergy in simultaneous imaging of tumour pH$_e$ and vasculature, we investigated the spatial pattern of UPS$_e$ and cRGD-UPS$_i$ activation in the tumour microenvironment. We employed intravital microscopy and subcutaneous A549 lung tumour xenograft in mice as our model system. To differentiate the two nanoprobes, we used TMR ($\lambda_{ex}/\lambda_{em}$ = 550/580 nm) and rhodamine G (RhoG, $\lambda_{ex}/\lambda_{em}$ = 502/527 nm) to label the UPS$_e$ and cRGD-UPS$_i$, respectively. The dual nanoprobes were co-injected intravenously and imaged over time. Fig. 5a shows complementary spatial activation patterns at 6 h post-injection: cRGD-UPS$_i$–RhoG activation was mostly restricted to tumour vessels, whereas UPS$_e$–TMR was illuminated in the interstitial space in the tumour parenchyma. Neither nanoprobe showed observable fluorescence inside tumour vasculature lumen, demonstrating that they remained 'silent' in blood.

To exploit the synergy of pH$_e$ and tumour vasculature activation, we constructed an integrated cRGD-UPS$_e$–Cy5.5 nanoprobe (iUPS) and investigated its tumour imaging efficacy in 10 different tumour models. These models include a transgenic MMTV-PyMT breast cancer (multi-foci along mammary glands), several orthotopic cancers (lung, head and neck, prostate) and various subcutaneous cancer models (brain, pancreatic cancers). In all 10 of the tumour models, we observed universal nanoprobe activation in the tumour microenvironment over surrounding normal tissues/organs (Fig. 5b,c and Supplementary Fig. 20a–j). In 3LL lung cancer (Fig. 5c), explanted tissues showed effective detection of small metastatic nodules (<1 mm). These data highlight the success of targeting the tumour microenvironment as a more robust and universal strategy to achieve broad tumour specificity.

Cancer is a diverse set of diseases with vastly different genotypes and phenotypes. Cancer-specific biomarkers and their expression levels can vary considerably among cancer types and organ sites[31]. This heterogeneity makes it challenging to establish a universal strategy for tumour detection using cancer-cell-centric approaches, despite the availability of many ligands with high affinity and specificity (for example, herceptin for Her2/neu). Compared with cancer-cell-targeted approaches, the tumour microenvironment contains biomarkers that are more consistent across a range of cancer types. Acidic pH$_e$ resulting from dysregulated glycolysis is a hallmark of cancer that has been associated with enhanced cell proliferation, evasion of apoptosis, invasion and metastasis[17,32]. Angiogenesis represents another hallmark of cancer, which is essential for sustained tumour growth and exchange of nutrients and metabolic waste. Although targeting the tumour microenvironment provides a promising strategy for broad tumour detection, the challenge resides in how to achieve sensitive visualization with high biological specificity. Imaging acidic tumour pH$_e$ (6.5–6.8) is difficult because it is not markedly different from blood (7.4). Small molecular pH sensors yield only <3-fold signal difference in this pH range (Fig. 2b). A

© 2013 Macmillan Publishers Limited. All rights reserved.

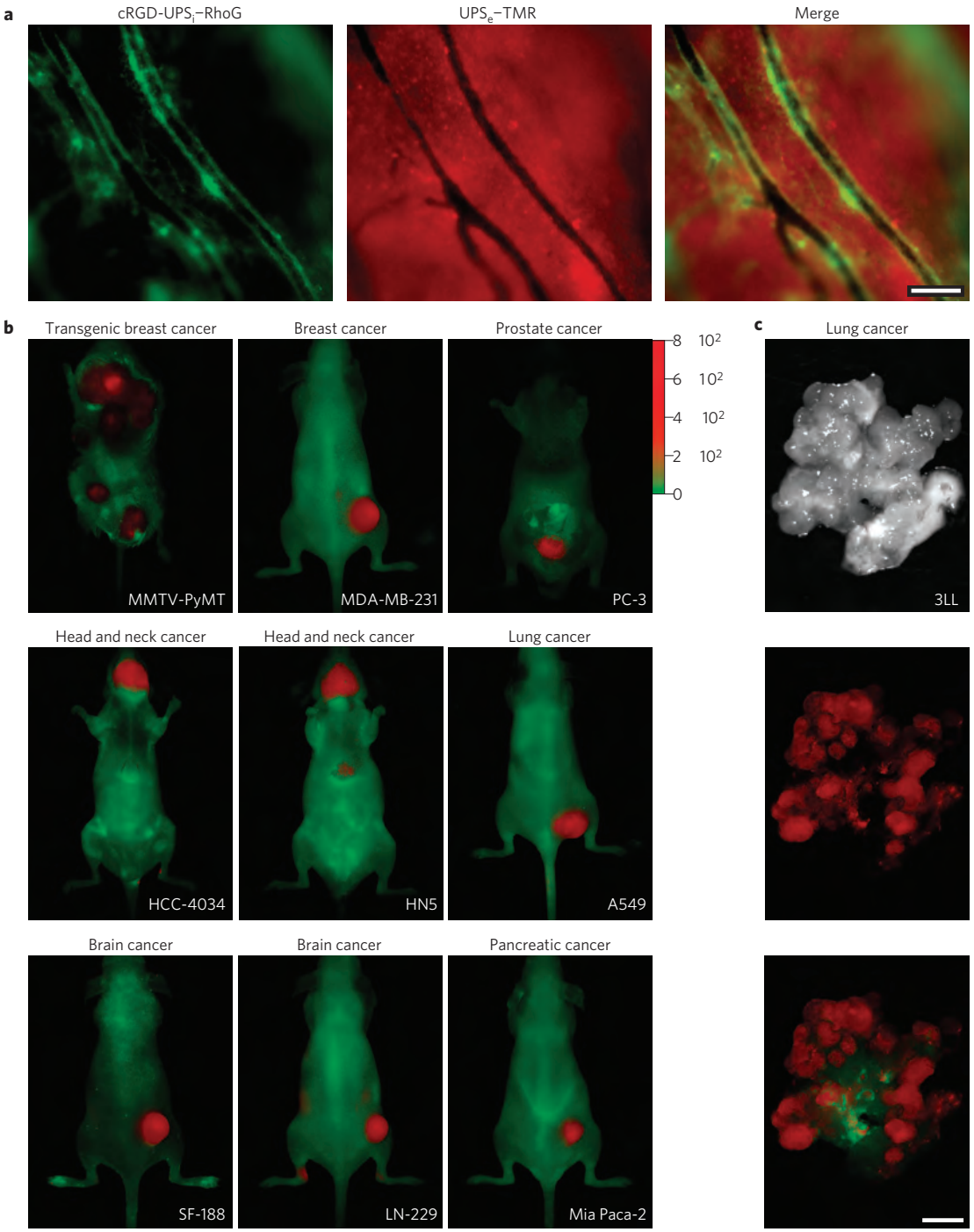

Figure 5 | iUPS nanoprobes target both acidic pH$_e$ and tumour vasculature with broad tumour specificity. a, Intravital fluorescent images show a complementary pattern of spatial activation of cRGD-UPS$_i$–RhoG (green) and UPS$_e$–TMR (red) inside tumour vasculature and parenchyma, respectively. The dual nanoprobes were co-injected intravenously and the images were taken 6 h post-injection. Scale bar, 100 μm. **b**,**c**, iUPS nanoprobes show broad tumour imaging specificity and efficacy in ten different tumour models of different cancer types (breast, prostate, head and neck, lung, brain and pancreatic cancers) and organ sites. In the 3LL lung cancer model (**c**), explanted lung was shown to illustrate the effective detection of small metastatic nodules (<1 mm). Scale bar, 2 mm. In each model, high *T*/*N* ratios were observed, demonstrating the success of targeting tumour microenvironment signals as a universal strategy to achieve broad tumour specificity (see Supplementary Fig. 20a–j).

considerably sharper pH response is necessary to differentiate the pH difference in tumour versus normal tissues. Meanwhile, tumour vasculature is comprised of a small volume fraction (~1.5%)[33,34], which necessitates an amplification strategy for robust detection.

Our iUPS design exploits amplification of tumour microenvironmental signals and background suppression to impact tumour imaging outcome. Compared with many small molecular imaging tracers (for example, folate–FITC, one dye molecule per tracer or cancer target), the nanoprobe design allows for a marked increase of dye payloads (for example, 1,600 dye per particle) and thus delivers more imaging beacons for signal amplification (as demonstrated by the superior imaging outcome by cRGD-UPS$_i$ over cRGD–IRDye 800CW). Most nanoprobes have a high background in the blood and low tumour contrast due to slow clearance compared with small

© 2013 Macmillan Publishers Limited. All rights reserved.

molecular tracers. Our present UPS design solved this problem through homoFRET-induced fluorescence quenching where the blood signal is abolished, leading to large OBR values (>300-fold). Ultra pH response is essential for the achieved imaging efficacy. Many previous studies on pH-sensitive nanoparticles showed improved antitumour response in drug delivery applications[19–23]. Most of these approaches were based on the breaking of pH-sensitive covalent bonds to induce nanoparticle degradation, which is time-consuming (for example, 24 h) and not very pH responsive. The present UPS design uses proton transfer and non-covalent self-assembly that renders a fast (<5 ms) and tunable response[18]. Consequently, UPS has an exquisite pH sensitivity over existing systems, as demonstrated by >100-fold ON/OFF activation within 0.25 pH unit with signal suppression in blood. When an appropriate pH threshold is selected (for example, 6.9), the UPS platform illustrated a powerful differentiation of subtle pH transitions between blood and tumour microenvironment. This approach seems to be robust and universal, as demonstrated in 10 different tumour models with diverse cancer phenotypes and organ sites. Preliminary animal studies show negligible toxicities, and the approach avoids the exposure to radioactivity (for example, ^{18}FDG) required for positron emission tomography. Potentially, the UPS platform and fluorescence imaging can provide high-resolution delineation of primary and metastatic tumours to achieve complete tumour resections during surgery. Finally, this nanoplatform can also serve as a valuable research tool to investigate cancer metabolism, to monitor acute perturbations of the microenvironment induced by metabolic inhibitors, and to illuminate the spatiotemporal dynamics of tumour hypoxia and acidic pH for the development of new therapies.

Methods

All animal procedures were approved by the Institutional Animal Care and Use Committee at the University of Texas Southwestern Medical Center. Pharmacokinetic experiments involving radioactive materials (^{3}H) were approved by the Radiation Safety Committee at the University of Texas Southwestern Medical Center.

Synthesis and characterization of UPS nanoprobes. Dye-conjugated MeO-PEG-b-PDPA and MeO-PEG-b-PC7A, and maleimide-terminated block copolymers were synthesized by the atom transfer radical polymerization method (Supplementary Methods). cRGD-UPS$_i$ nanoprobes were prepared following a previously published procedure[35]. In a typical procedure, 2 mg of MAL-PEG-b-PDPA and 18 mg of MeO-PEG-b-PDPA–Cy5.5 were dissolved in 1 ml THF. Then, the mixture was added into 4 ml of Milli-Q water under sonication. The mixture was filtered four times to remove THF using a micro-ultrafiltration system. After micelle formation, an excess amount of c(RGDf(ε-acetylthiol)K) and 0.05 M hydroxylamine in 0.05 M HEPES/0.01 M EDTA aqueous solution were added. The conjugation was allowed to occur for 4 h followed by filtration to remove any precipitates in the micelle solution. The cRGD-UPS$_i$ nanoprobe was filtered six times to remove free peptide. To prepare the UPS$_i$ or UPS$_e$ nanoprobes, 20 mg of MeO-PEG-b-PDPA–Cy5.5 or MeO-PEG-b-PC7A–Cy5.5 was dissolved in THF. The solution was added into water under sonication. Then, the mixture was filtered four times to remove THF. To prepare the always-ON PEG-b-PC7A nanoprobes, 19 mg of MeO-PEG-b-PC7A and 1 mg of MeO-PEG-b-PC7A–Cy5.5 were dissolved in THF, added into water, and filtered by ultrafiltration. To prepare the always-ON cRGD-encoded PEG-b-PDPA nanoprobes, 2 mg of MAL-PEG-b-PDPA, 17 mg of MeO-PEG-b-PDPA and 1 mg of MeO-PEG-b-PDPA–Cy5.5 were dissolved in THF, and the same procedure as shown above was used for cRGD conjugation. ^{1}H-NMR spectroscopy was used to confirm the formation of core–shell structure and conjugation of cRGD peptide to the micelle surface. The successful conjugation of cRGD on the surface of micelles was validated by the appearance of phenyl protons of cRGD at 7.4 ppm. Transmission electron microscopy was carried out with 1% phosphotungstic acid negative staining and visualized on a JEOL 1200EX electron microscope (JEOL 1200EX).

Fluorescence activation of UPS nanoprobes. Fluorescence emission spectra of UPS nanoprobes in different pH buffer solutions were obtained on a Hitachi fluorometer (F-7500 model). For each UPS nanoprobe, the sample (5 mg ml^{-1}) was prepared in Milli-Q water. Then, the solution was diluted in 50 mM phosphate-buffered saline (PBS) buffer with different pH values. The final polymer concentration was controlled at 0.1 mg ml^{-1}. The nanoprobe was excited at 675 nm, and the emission spectra were collected from 690 to 770 nm. The emission intensity at 710 nm was used to quantify the signal amplification for UPS nanoprobes. Fluorescent images of UPS$_i$ and UPS$_e$ nanoprobe solutions (0.1 mg ml^{-1}) at different pH values were captured on a Maestro *in vivo* imaging system (CRI) using the 'orange' filter (645–820 nm).

***In vitro* serum stability.** Fresh mouse serum was collected and filtered through 0.22 μm syringe filters. Then, 0.2 ml of cRGD-UPS$_i$ or UPS$_e$ nanoprobe (2 mg ml^{-1}) was added to 2 ml of serum. The mixture was incubated at 37 °C in a humidified chamber. At each designated time point, 100 μl aliquots of serum mixture were collected and immediately imaged by the Maestro *in vivo* imaging system under identical settings to quantify the fluorescence intensity.

Cell culture. The tumour cell lines used for *in vivo* implantation include A549 lung carcinoma, MDA-MB-231 breast cancer, HN5 and HCC4034 head–neck cancer, SF-188 glioma, LN-229 glioma, 3LL lung carcinoma, Mia Paca-2 pancreatic cancer and PC-3 prostate cancer cells. Cells were cultured in DMEM with 10% fetal bovine serum and antibiotics.

Animal models. Female athymic *nu/nu* mice (18–22 g) were purchased from Charles River. Mice were inoculated subcutaneously on the right flank with A549 cells (5×10^6 per mouse). Three to four weeks after implantation, animals with tumour size of 200–300 mm^3 were used for pharmacokinetic, biodistribution and imaging studies. To demonstrate the universal imaging applications of the integrated nanoprobe, orthotopic tumour models, including HN5 and HCC4034 head–neck cancers, PC-3 prostate cancer and 3LL Lewis lung carcinoma were developed. MMTV-PyMT transgenic mice bearing multifocal mammary tumours were established by R.J.D's laboratory. Subcutaneous tumour models, including MDA-MB-231 breast cancer, SF-188 glioma, LN-229 glioma and Mia Paca-2 pancreatic carcinoma, were established.

Pharmacokinetics and biodistribution studies. ^{3}H-labelled cRGD-UPS$_i$ were prepared from 90% MeO-PEG-b-PDPA-C(O)CT$_3$ and 10% MAL-PEG-b-PDPA. UPS$_i$ and UPS$_e$ were prepared from MeO-PEG-b-PDPA-C(O)CT$_3$ and MeO-PEG-b-PC7A-C(O)CT$_3$, respectively. For pharmacokinetic experiments, mice bearing A549 tumours were randomly divided into three groups ($n = 4$–5 for each group) for cRGD-UPS$_i$, UPS$_i$ and UPS$_e$. The mice were injected intravenously with micelle solutions. Blood was collected at 2 min, 30 min, 1, 3, 6, 12 and 24 h after injection. Plasma (20 μl) was isolated by centrifugation at 5,000*g* for 10 min. Plasma was subsequently mixed with a tissue solubilizer solution (1 ml, BTS-450; Beckman) at room temperature for 12 h followed by addition of a liquid scintillation mixture (10 ml, Ready Organic, Beckman) for 24 h. The amount of radioactive isotope was measured by a liquid scintillation counter (Beckman LS 6000 IC). Biodistribution of cRGD-UPS$_i$, UPS$_i$ and UPS$_e$ nanoprobes in tumour and other organs was performed in a separate group of A549-tumour-bearing mice ($n = 4$ for each group). Mice were perfused with PBS buffer (30 ml) at pre-designated time points (6 and 24 h). Dissected organs were weighed, homogenized and treated with scintillation mixtures. The nanoprobe distribution in different organs/tissues was calculated as the percentage of injected dose per gram of tissue.

***In vivo* and *ex vivo* near-infrared fluorescence imaging.** For tumour vasculature imaging, cRGD-UPS$_i$ or UPS$_i$ (10 mg kg^{-1}) was administrated intravenously into the A549-tumour-bearing mice ($n = 4$ for each group). Time-course fluorescent images were captured on a Maestro *in vivo* imaging system using the 'orange' filter. To elucidate the role of $\alpha_v\beta_3$-mediated endocytosis, a group of mice were injected with cRGDfK (25 mg kg^{-1}) 30 min before cRGD-UPS$_i$ injection. To demonstrate the enhanced permeability and retention effect, always-ON nanoprobe was also used as a control.

For pH$_e$ imaging, UPS$_e$ (10 mg kg^{-1}) was injected into A549-tumour-bearing mice ($n = 4$ for each group). Time-lapse near-infrared images were captured on a Maestro system using the 'orange' filter. As controls, 2-DG (250 mg kg^{-1}) or CHC (250 mg kg^{-1}) was injected 12 h before the UPS$_e$ nanoprobe administration. Then, the mice were monitored at pre-designated time points.

Ten tumour models described above were used to demonstrate the universal application of cRGD-UPS$_e$–Cy5.5 integrated nanoprobe in tumour microenvironment imaging. Integrated nanoprobe (10 mg kg^{-1}) was administrated intravenously into tumour-bearing mice ($n = 4$ for each tumour model). Fluorescent images were captured at 24 h post-injection.

Tumour/normal tissue (T/N) ratios were determined by comparing the average fluorescence intensities in the tumour and the whole body except the tumour site. After imaging, the mice were euthanized. Excised tumour and organs were imaged by the Maestro system. Fluorescence intensities of *ex vivo* tumours were quantified and normalized to the value of the muscle and blood.

Intravital imaging. Mice bearing A549 tumours were anaesthetized with isoflurane and fixed under a Nikon ECLIPSE intravital microscope (Nikon) with a two-channel method in which one channel was used to image the activation of the cRGD-UPS$_i$ nanoprobe in tumour vasculature and the other channel was used to probe the signal amplification of UPS$_e$ nanoprobe in acidic tumour microenvironment. Mixtures of cRGD-UPS$_i$–RhoG (10 mg kg^{-1}, green) and UPS$_e$–TMR (10 mg kg^{-1}, red) were intravenously injected into tumour-bearing mice ($n = 4$). Images were captured with a resolution of 1,024 × 768 pixels with ×10 Nikon objectives.

© 2013 Macmillan Publishers Limited. All rights reserved.

Immunofluorescence staining. In tumour vasculature imaging studies, the mice were euthanized at 6 h post-injection. Tumours were snap frozen and cut into 8-μm sections. The slices were fixed in cold acetone and rinsed with PBS three times, and blocked with 10% BSA for 1 h at room temperature. Subsequently, the slices were incubated with rat anti-mouse CD31 antibody (BD Biosciences) at 4 °C overnight. Then, Alexa Flour 488-conjugated secondary antibody was added to stain the slices. The slides were mounted with DAPI-containing medium. The images were captured on a fluorescence microscope (Nikon ECLIPSE TE2000-E).

In pH_e imaging studies, the tumour-bearing mice were intravenously injected with UPS_e (10 mg kg^{-1}). At 5 h post-injection, the animals were injected with pimonidazole (60 mg kg^{-1}). One hour later, tumours were collected, frozen and cut into 8-μm sections. Adjacent tumour sections were exposed to primary antibody for 1 h at room temperature. Primary antibodies used were as follows: FITC-conjugated murine antipimonidazole monoclonal antibody (HPI); rat anti-mouse CD31 antibody; and rabbit anti-mouse Ki-67 antibody (Millipore). Sections were washed three times with PBS and incubated with the appropriate secondary antibodies for 1 h. CD31 was detected with Alexa Flour 488-conjugated secondary antibody. Ki-67 was detected with Cy2-conjugated goat anti-rabbit antibody. The sections were scanned on an image analysis system consisting of a Nikon fluorescence microscope using a computer-controlled motorized stage with a digital camera. All images were scanned at ×200 magnification. Composite images of sections were generated by the software from individual microscopic images.

Statistical analysis. Data were expressed as mean ± s.d. Differences between groups were assessed using the paired, two-sided Student *t*-test. $^{*}P < 0.05$ was considered significant, and $^{**}P < 0.01$ was considered highly significant.

Received 7 March 2013; accepted 24 October 2013; published online 8 December 2013

References

1. Stuart, M. A. *et al.* Emerging applications of stimuli-responsive polymer materials. *Nature Mater.* **9,** 101–113 (2010).
2. De Las Heras Alarcon, C., Pennadam, S. & Alexander, C. Stimuli responsive polymers for biomedical applications. *Chem. Soc. Rev.* **34,** 276–285 (2005).
3. Von Maltzahn, G. *et al.* Nanoparticles that communicate *in vivo* to amplify tumour targeting. *Nature Mater.* **10,** 545–552 (2011).
4. Bellomo, E. G., Wyrsta, M. D., Pakstis, L., Pochan, D. J. & Deming, T. J. Stimuli-responsive polypeptide vesicles by conformation-specific assembly. *Nature Mater.* **3,** 244–248 (2004).
5. Welsher, K. *et al.* A route to brightly fluorescent carbon nanotubes for near-infrared imaging in mice. *Nature Nanotech.* **4,** 773–780 (2009).
6. So, M. K., Xu, C., Loening, A. M., Gambhir, S. S. & Rao, J. Self-illuminating quantum dot conjugates for *in vivo* imaging. *Nature Biotechnol.* **24,** 339–343 (2006).
7. Kircher, M. F. *et al.* A brain tumour molecular imaging strategy using a new triple-modality MRI-photoacoustic-Raman nanoparticle. *Nature Med.* **18,** 829–834 (2012).
8. Qian, X. *et al. In vivo* tumour targeting and spectroscopic detection with surface-enhanced Raman nanoparticle tags. *Nature Biotechnol.* **26,** 83–90 (2008).
9. Olson, E. S. *et al.* Activatable cell penetrating peptides linked to nanoparticles as dual probes for *in vivo* fluorescence and MR imaging of proteases. *Proc. Natl Acad. Sci. USA* **107,** 4311–4316 (2010).
10. Urano, Y. *et al.* Selective molecular imaging of viable cancer cells with pH-activatable fluorescence probes. *Nature Med.* **15,** 104–109 (2009).
11. Van Dam, G. M. *et al.* Intraoperative tumour-specific fluorescence imaging in ovarian cancer by folate receptor-α targeting: First in-human results. *Nature Med.* **17,** 1315–1319 (2011).
12. Ke, S. *et al.* Near-infrared optical imaging of epidermal growth factor receptor in breast cancer xenografts. *Cancer Res.* **63,** 7870–7875 (2003).
13. Paik, S. *et al.* HER2 and choice of adjuvant chemotherapy for invasive breast cancer: National surgical adjuvant breast and bowel project protocol B-15. *J. Natl Cancer Inst.* **92,** 1991–1998 (2000).
14. Jacobs, T. W., Gown, A. M., Yaziji, H., Barnes, M. J. & Schnitt, S. J. HER-2/neu protein expression in breast cancer evaluated by immunohistochemistry. A study of interlaboratory agreement. *Am. J. Clin. Pathol.* **113,** 251–258 (2000).
15. Weis, S. M. & Cheresh, D. A. Tumour angiogenesis: Molecular pathways and therapeutic targets. *Nature Med.* **17,** 1359–1370 (2011).
16. Folkman, J. Angiogenesis: An organizing principle for drug discovery? *Nature Rev. Drug Discov.* **6,** 273–286 (2007).
17. Webb, B. A., Chimenti, M., Jacobson, M. P. & Barber, D. L. Dysregulated pH: A perfect storm for cancer progression. *Nature Rev. Cancer* **11,** 671–677 (2011).
18. Zhou, K. *et al.* Tunable, ultrasensitive pH-responsive nanoparticles targeting specific endocytic organelles in living cells. *Angew. Chem. Int. Ed.* **50,** 6109–6114 (2011).
19. Bachelder, E. M., Beaudette, T. T., Broaders, K. E., Dashe, J. & Frechet, J. M. Acetal-derivatized dextran: An acid-responsive biodegradable material for therapeutic applications. *J. Am. Chem. Soc.* **130,** 10494–10495 (2008).
20. Bae, Y., Fukushima, S., Harada, A. & Kataoka, K. Design of environment-sensitive supramolecular assemblies for intracellular drug delivery: Polymeric micelles that are responsive to intracellular pH change. *Angew. Chem. Int. Ed.* **42,** 4640–4643 (2003).
21. Griset, A. P. *et al.* Expansile nanoparticles: Synthesis, characterization, and *in vivo* efficacy of an acid-responsive polymeric drug delivery system. *J. Am. Chem. Soc.* **131,** 2469–2471 (2009).
22. Lee, E. S., Na, K. & Bae, Y. H. Super pH-sensitive multifunctional polymeric micelle. *Nano Lett.* **5,** 325–329 (2005).
23. Potineni, A., Lynn, D. M., Langer, R. & Amiji, M. M. Poly(ethylene oxide)-modified poly(beta-amino ester) nanoparticles as a pH-sensitive biodegradable system for paclitaxel delivery. *J. Control. Release* **86,** 223–234 (2003).
24. Zhou, K. *et al.* Multicolored pH-tunable and activatable fluorescence nanoplatform responsive to physiologic pH stimuli. *J. Am. Chem. Soc.* **134,** 7803–7811 (2012).
25. Sonveaux, P. *et al.* Targeting lactate-fueled respiration selectively kills hypoxic tumor cells in mice. *J. Clin. Invest.* **118,** 3930–3942 (2008).
26. Maeda, H., Wu, J., Sawa, T., Matsumura, Y. & Hori, K. Tumor vascular permeability and the EPR effect in macromolecular therapeutics: A review. *J. Control. Release* **65,** 271–284 (2000).
27. Gatenby, R. A. & Gillies, R. J. Why do cancers have high aerobic glycolysis? *Nature Rev. Cancer* **4,** 891–899 (2004).
28. Kleiter, M. M. *et al.* A comparison of oral and intravenous pimonidazole in canine tumors using intravenous CCI-103F as a control hypoxia marker. *Int. J. Radiat. Oncol. Biol. Phys.* **64,** 592–602 (2006).
29. Huang, X. *et al.* A reexamination of active and passive tumor targeting by using rod-shaped gold nanocrystals and covalently conjugated peptide ligands. *ACS Nano* **4,** 5887–5896 (2010).
30. Moghimi, S. M., Hedeman, H., Muir, I. S., Illum, L. & Davis, S. S. An investigation of the filtration capacity and the fate of large filtered sterically-stabilized microspheres in rat spleen. *Biochim. Biophys. Acta* **1157,** 233–240 (1993).
31. Polyak, K. Heterogeneity in breast cancer. *J. Clin. Invest.* **121,** 3786–3788 (2011).
32. Vander Heiden, M. G., Cantley, L. C. & Thompson, C. B. Understanding the Warburg effect: The metabolic requirements of cell proliferation. *Science* **324,** 1029–1033 (2009).
33. Dhanabal, M. *et al.* Endostatin induces endothelial cell apoptosis. *J. Biol. Chem.* **274,** 11721–11726 (1999).
34. Folkman, J. What is the evidence that tumors are angiogenesis dependent? *J. Natl Cancer Inst.* **82,** 4–6 (1990).
35. Nasongkla, N. *et al.* Multifunctional polymeric micelles as cancer-targeted, MRI-ultrasensitive drug delivery systems. *Nano Lett.* **6,** 2427–2430 (2006).

Acknowledgements

This work is supported by the NIH (R01EB013149 and R01CA129011) and Cancer Prevention and Research Institute of Texas (RP120094). Animal imaging work is supported by the UT Southwestern Small Animal Imaging Resource Grant (U24 CA126608) and Simmons Cancer Center Support Grant (P30 CA142543). We thank H. Zhou for help with the Maestro imaging, X. Luo for assistance with animal handling, and J. T. Hsieh and L. Gandee for help with histology.

Author contributions

Y.W. and J.G. are responsible for all phases of the research; K.Z., G.H., X.H., X.M. and T.Z. helped with synthesis of different dye-conjugated polymers and characterization of UPS nanoprobes; C.H. and R.J.D. designed metabolic inhibition experiments and performed *in vitro* cell studies; R.J.D. supplied the transgenic MMTV-PyMT breast tumour model; B.D.S. guided the preclinical development of the experiments. Y.W. and G.H. wrote the initial draft. R.J.D., B.D.S. and J.G. revised the final draft.

Additional information

Supplementary information is available in the online version of the paper. Reprints and permissions information is available online at www.nature.com/reprints. Correspondence and requests for materials should be addressed to J.G.

Competing financial interests

The authors declare no competing financial interests.

© 2013 Macmillan Publishers Limited. All rights reserved.

nature materials

SUPPLEMENTARY INFORMATION

DOI: 10.1038/NMAT3819

A nanoparticle-based strategy for the imaging of a broad range of tumours by nonlinear amplification of microenvironment signals

Yiguang Wang[1], Kejin Zhou[1], Gang Huang[1], Chris Hensley[2], Xiaonan Huang[1], Xinpeng Ma[1], Tian Zhao[1], Baran D. Sumer[3], Ralph J. DeBerardinis[2], Jinming Gao[1,*]

[1]*Department of Pharmacology, Simmons Comprehensive Cancer Center,* [2]*Children's Medical Center Research Institute, and* [3]*Department of Otolaryngology, University of Texas Southwestern Medical Center, 5323 Harry Hines Blvd., Dallas, Texas 75390, USA*

Correspondence should be addressed to J.G. (jinming.gao@utsouthwestern.edu)

© 2013 Macmillan Publishers Limited. All rights reserved.

DOI: 10.1038/NMAT3819

Materials

Cyclic RGDfK (cRGDfK) peptide was purchased from Peptides International Inc. (Kentucky, USA). LysoTracker® Green, MitoTracker® Green, Hoechest 33342, fetal bovine serum, penicillin streptomycin, and cell culture media were obtained from Invitrogen Inc. (OR, USA). Amicon ultra-15 centrifugal filter tubes (MWCO = 100 K) were from Millipore. Cy5.5 NHS ester was obtained from Lumiprobe company. Monomers 2-(diisopropyl amino) ethyl methacrylate (DPA-MA), 2-aminoethyl methacrylate (AMA) were from Polyscience Company. 2-(Hexamethyleneimino) ethyl methacrylate (C7A-MA) and PEG macroinitiator (MeO-PEG5k-Br) were prepared according to the method described in our previous work[1]. Other organic solvents were analytical grade from Sigma-Aldrich or Fisher Scientific Inc.

Syntheses of dye-conjugated block copolymers

Two different block copolymers (i.e. PEG-*b*-(PR-*co*-AMA)) (**Scheme 1**) were synthesized by atom transfer radical polymerization (ATRP) method[2]. The dye-free copolymers were used in polymer characterizations (Table S1). For the conjugation of near infrared fluorescent dye

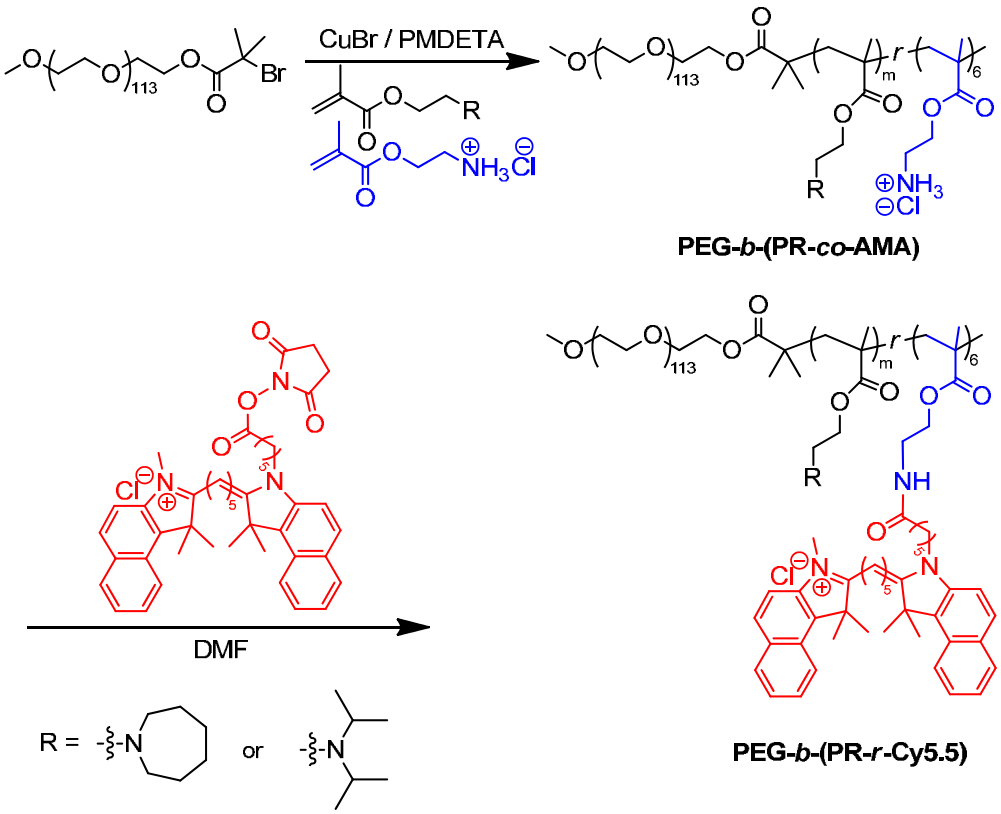

Scheme S1: Synthesis of dye-conjugated block copolymers.

© 2013 Macmillan Publishers Limited. All rights reserved.

(Cy5.5) or tritium (^{3}H or T) labeling, aminoethyl methacrylate (AMA) was used in the copolymer synthesis. The primary amino groups were introduced into each polymer chain by controlling the feeding ratio of the AMA monomer to the initiator (molar ratio = 1, 3, or 6). The polymer chain length of PR fragment was controlled by changing the feeding ratio of the monomer to the initiator (molar ratio = 40, 60, 80, or 100). PEG-*b*-P(DPA-*co*-AMA_6) is used as an example to illustrate the procedure. First, diisopropylaminoethyl methacrylate (DPA, 1.71 g, 8 mmol), AMA (100 mg, 0.6 mmol), PMDETA (21 μL, 0.1 mmol), and MeO-PEG_{114}-Br (0.5 g, 0.1 mmol) were charged into a polymerization tube. Then a mixture of 2-propanol (2 mL) and DMF (2 mL) was added to dissolve the monomer and initiator. After three cycles of freeze-pump-thaw to remove oxygen, CuBr (14.4 mg, 0.1 mmol) was added into the reaction tube under nitrogen atmosphere, and the tube was sealed *in vacuo*. The polymerization was carried out at 40 ^{o}C for 12 h. After polymerization, the reaction mixture was diluted with 10 mL THF, and passed through an Al_2O_3 column to remove the catalyst. The THF solvent was removed by rotovap. The residue was dialyzed in distilled water and lyophilized to obtain a white powder. The resulting PEG-*b*-P(DPA-*co*-AMA_6) copolymers were characterized by ^{1}H 500 MHz NMR, gel permeation chromatography (Viscotech GPCmax, PLgel 5μm MIXED-D columns by Polymer Labs, THF as eluent at 1 mL/min). **Table S1** and **Table S2** enlist the yield, molecular weights (M_n and M_w) and polydispersity index (PDI) of each PEG-*b*-P(DPA-*co*-AMA) copolymer. Molecular weight (M_n and $M_{w)}$ and PDI of PEG-*b*-P(C7A-*co*-AMA_6) were 18.7 kD, 22.4 kD, and 1.19, respectively.

For Cy5.5 conjugation, 50 mg of PEG-*b*-P(DPA-*co*-AMA_6) or PEG-*b*-P(C7A-*co*-AMA_6) was first dissolved in 2 mL of anhydrous DMF. Then, Cy5.5 NHS ester (1.5 equivalents to the molar amount of the primary amino group) was added. The reaction mixture was stirred at room temperature for two days. The polymer conjugates were purified by preparative gel permeation chromatography (PLgel Prep 10μm 10E3Å, 300×25mm column by varian, THF as eluent at 5 mL/min) to remove the free dye molecules. The resulting polymer conjugates were lyophilized and stored at -20 °C.

Synthesis of maleimide-terminated poly(ethylene glycol)-*b*-poly(2-(diisopropylamino) ethyl methacrylate) (MAL-PEG-*b*-PDPA)

First, *N*-Maleoyl-*β*-alanine **1** (250 mg, 1.5 mmol) and furan (2.2 mL, 30 mmol) were dissolved in 10 mL benzene. The solution was refluxed overnight. After reaction, the solution was concentrated and then purified by flash chromatography to yield compound **2**. ^{1}H NMR

© 2013 Macmillan Publishers Limited. All rights reserved.

DOI: 10.1038/NMAT3819

(TMS, $CDCl_3$, ppm): 6.52 (2H, =C*H*CH(O-))-), 5.28 (2H, =CHC*H*(O-))-), 3.66 (2H, -NC*H2*CH2-), 2.87 (2H, -(-O)CHC*H*(CH)-), 2.55 (2H, -NCH2C*H2*-). Yield: 65 %. Then, compound **2** (48 mg, 0.20 mmol) and *N*-hydroxymaleimide (25 mg, 0.22 mmol) were dissolved in 5 mL dichloromethane (DCM). *N*,*N*′-dicyclohexylcarbodiimide (50 mg, 0.24 mmol) was added to the above solution. After the solution was stirred for 2 h at room temperature, HO-PEG_{5K}-NH_2 (500 mg, 0.1 mmol) was added and the reaction solution was stirred continuously overnight. The reaction solution was filtered and the filtrate was poured into 50 mL cold diethyl ether. The precipitation was collected and dried for next reaction. The above product was dissolved in 5 mL DCM with the addition of triethylamine (70 µL, 0.5 mmol). Then *α*-bromoisobutyryl bromide (65 µL, 0.5 mmol) was added and the solution was stirred overnight. The reaction solution was poured into 50 mL cold diethyl ether and the precipitate was collected. The product was further purified by two dissolve-and-precipitation cycles and then dried. ^{1}H NMR (TMS, $CDCl_3$, ppm): 6.52 (2H, =C*H*CH(O-))-), 5.26 (2H, =CHC*H*(O-))-), 4.33 (2H, -C*H2*OC(O)2-), 3.93~3.30 (460H, -NC*H2*C*H2*O(C*H2*C*H2*O)$_{114}$-), 2.87 (2H, -(-O)CHC*H*(CH)-), 2.55 (2H, -NCH2C*H2*-), 1.92 (6H, -C(O)C(C*H3*)$_2$Br). Yield: 59%. DPA (479 mg, 2.24 mmol), PMDETA (7.0 µL, 0.034 mmol), and proMAL-PEG_{114}-Br (150 mg, 0.028 mmol) were charged into a polymerization tube. Then a mixture of 2-propanol (0.50 mL) and DMF (0.50 mL) was added to dissolve the monomer and initiator. After three cycles of freeze-pump-thaw to remove oxygen, CuBr (4.5 mg, 0.031 mmol) was added into the reaction tube under nitrogen atmosphere, and the tube was sealed in vacuum. The polymerization was carried out at 50 °C for 8 h. After polymerization, the reaction mixture was diluted with 10 mL THF, and passed through an Al_2O_3 column to remove the catalyst. The THF solvent was removed by rotovap. The residue was dialyzed in distilled water and lyophilized to obtain a white powder with 65% yield. The proMAL-PEG-*b*-PDPA copolymer was characterized by ^{1}HNMR (500 MHz), gel permeation chromatography (Viscotech GPCmax, PLgel 5µm MIXED-D columns by Polymer Labs, THF as eluent at 1 mL/min). Finally, 200 mg proMAL-PEG-*b*-PDPA copolymer was dissolved in 10 mL toluene. The reaction solution was refluxed overnight. The toluene was removed. The conversion was quantitative. The residue was dialyzed in distilled water and lyophilized to obtain a white powder with 95% yield. MAL-PEG-*b*-PDPA copolymer was characterized by ^{1}HNMR. The complete conversion was verified by the appearance of the characteristic resonance of maleimide protons at 6.71 ppm. Molecular weight (M_n and $M_{w)}$ and polydispersity index (PDI) of MAL-PEG-*b*-PDPA were 22.8 kD, 27.8 kD, and 1.22, respectively.

© 2013 Macmillan Publishers Limited. All rights reserved.

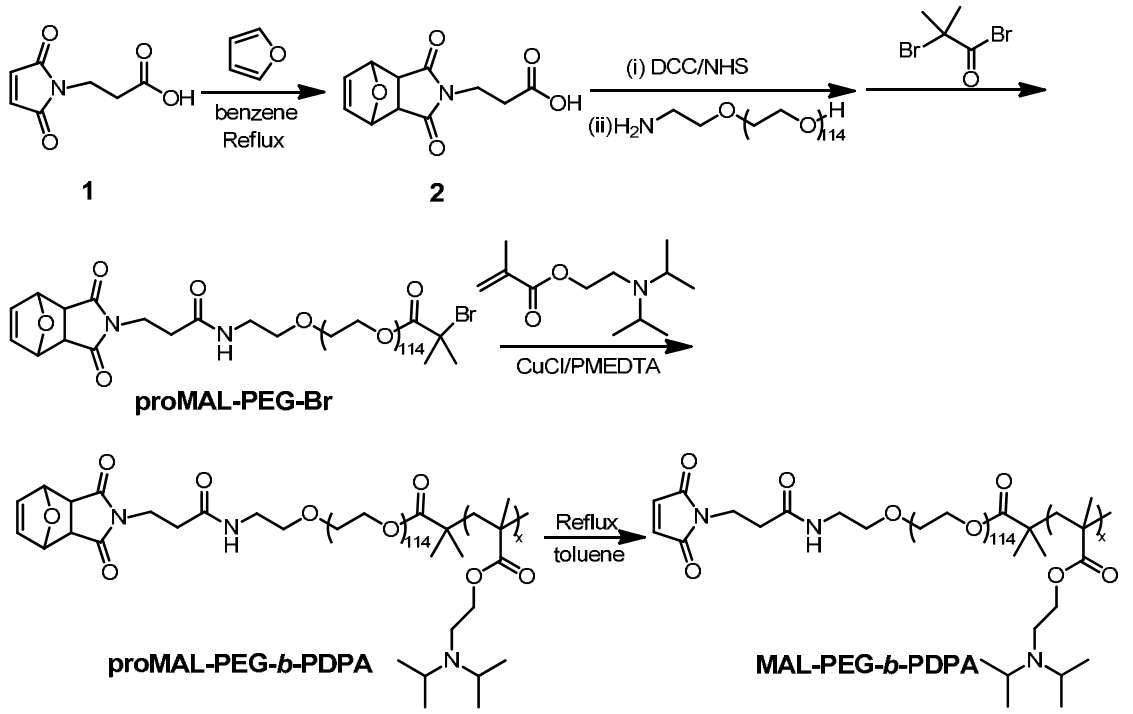

Scheme S2: Synthesis of maleimide-terminated poly(ethylene glycol)-*b*-poly(2-(diisopropylamino) ethyl methacrylate).

Effect of micelle dilution on pH response

To investigate whether UPS dilution will affect its pH response, we examined the concentration-dependent properties of UPS_e/UPS_i nanoprobes. For each nanoprobe, the sample (5 mg/mL) was prepared in Milli-Q water. The solution was diluted in 50 mM PBS buffer (pH 7.4) to obtain a series of concentrations for each nanoprobe (0.5, 1, 2, 2.5, 3, 4, and 5 mg/mL). Then, the nanoprobe solution was diluted in 50 mM PBS buffer with different pH values. The final polymer concentrations are 10, 20, 40, 50, 60, 80, and 100 μg/mL. The nanoprobe was excited at 675 nm, and the emission spectra were collected from 690 to 770 nm. The emission intensity at 710 nm was used to quantify the signal amplification for the UPS nanoprobes.

Preparation and characterization of always-ON nanoprobes

Nanoprobes were prepared following a previously published procedure. Firstly, a series of molecularly mixed micelles of PEG-*b*-(PR-*co*-$Cy5.5_6$) and PEG-*b*-(PR-*co*-AMA_6) with different molar ratios from 1:1 to 1:19 were prepared. In an example of mixed micelle of PEG-*b*-P(DPA_{80}-*co*-$Cy5.5_6$) and PEG-*b*-P(DPA_{80}-*co*-AMA_6) with 1:1 molar ratio, PEG-*b*-P(DPA_{80}-*co*-$Cy5.5_6$)

© 2013 Macmillan Publishers Limited. All rights reserved.

DOI: 10.1038/NMAT3819

(2.3 mg) and PEG-*b*-P(DPA$_{80}$-*co*-AMA$_6$) (2 mg) were first dissolved in 0.5 mL THF and then added into 4 mL distilled water dropwise under sonication. THF was removed through micro-ultrafiltration system (100 kD) for 4 times. Then, the distilled water was added to adjust the final polymer concentration to 5 mg/mL for further fluorescence characterization.

After fluorescence characterization, molecularly mixed micelles with fluorescence ON/OFF ratio with ~ 1 were selected as optimized formulations to prepare the always ON nanoprobes. In a typical procedure, mixed micelle of PEG-*b*-P(DPA$_{80}$-*co*-Cy5.5$_6$) and PEG-*b*-P(DPA$_{80}$-*co*-AMA$_6$) with 1:19 molar ratio were prepared as an always ON nanoprobe. The particle size and morphology of always-On nanoprobes were characterized by transmission electron microscopy (JEOL 1200EX). Zeta-potential of nanoprobes was determined by Malvern Zetasizer Nano-ZS instrument (He-Ne laser, λ = 632 nm).

Measurement of critical micelle concentration (CMC)

CMC of each copolymer was measured in 0.1 M phosphate buffer saline (PBS, pH 7.4). First, a copolymer stock solution (5 mg/mL) was diluted to different concentrations in the same buffer. In each solution, 5μL pyrene in THF solution (2×10^{-4} mol/L) was added to 2 mL polymer solution to produce the final pyrene concentration at 5×10^{-7} mol/L. The fluorescence spectra were recorded on a Hitachi fluoremeter (F-7500 model) with the excitation wavelength of 339 nm and the excitation and emission slits at 10.0 nm and 1.0 nm, respectively. The I_1 and I_3 values were measured as the maximum emission intensity at ca. 372 and 382 nm, respectively. I_1/I_3 ratio was plotted as a function of polymer concentration at different pH values. I_1/I_3 ratio reflects the polarity of the pyrene environment where partition of pyrene in the hydrophobic micelle core leads to decreased I_1/I_3 values[3,4]. The CMC values at pH 7.4 were listed in **Table S1** and **Table S2**.

Histology analysis of liver and spleen

Healthy nude mice (n = 3) were co-injected with UPS$_i$ nanoprobe (10 mg/kg) and Cy3-labeled always-ON nanoprobe (20 mg/kg) via the tail vein. The mice were sacrificed at 6 hours post-injection. Liver and spleen were immediately collected, snap frozen, and cut into 8-μm sections. The fluorescence images were captured on a fluorescence microscope (Nikon ECLIPSE, Japan). Cy5.5 and Cy3 were imaged using TRITIC and Cy5 filters, respectively. All images were

© 2013 Macmillan Publishers Limited. All rights reserved.

captured at ×100 and × 200 magnifications. After acquisition of fluorescence images, the same tissue sections were stained with H&E and imaged by light microscopy.

In vitro metabolic studies

Stock solutions of alpha-cyano-4-hydroxycinnamic acid (CHC, 1 M) and 2-deoxyglucose (2-DG, 1 M) dissolved in PBS buffer were used. Metabolism studies were performed as previously described with minor modifications[5]. Briefly, A549 cells (1.2×10^6/well) were seeded in 6 well plates and incubated for 24 h before inhibition studies. Media were removed and replaced at the beginning of experiments with media containing inhibitors or vehicle controls. Concentration of lactate in the culture media was subsequently measured with an automated electrochemical analyzer (BioProfile Basic-4 analyzer, NOVA). Protein concentrations were analyzed from cell pellets using a Pierce BCA protein assay kit. Metabolic assays were conducted 6 h after inhibitor addition. The pH of the media was measured with a pH meter (Mettler-Toledo International Inc., Columbus, OH) at 24 h after inhibitor addition.

Fluorescence activation of UPS_i nanoprobes and their localization in HUVEC cells

Human umbilical vein endothelial cells (HUVECs) were obtained from Lonza and maintained in EBM with EGM singlequots. HUVECs were used in exponential growth phase, and all the experiments were conducted at passage <6. Confocal scanning microscopy was used to investigate the cellular uptake and intracellular distribution of cRGD-UPS_i nanoprobe in HUVECs. Toward this, cells were plated in glass bottom dishes (MatTek, MA) in 2 mL complete medium and incubated with cRGD-UPS_i or UPS_i at a polymer concentration of 0.2 mg/mL at pH 7.4. Confocal images were captured at 3 h after addition of micelles. In the competitive experiment, HUVECs were pretreated with a 50-fold molar excess of cRGDfK, and the cRGD-UPS_i were subsequently incubated with the cells for 3 h. The images were analyzed using Image-J software. Five independent measurements were presented as the mean ± standard deviation.

To further demonstrate the targeting specificity of cRGD-UPS_i nanoprobe, cell lines with different integrin αvβ3 expression levels were incubated with 0.2 mg/mL cRGD-UPS_i nanoprobe for 3 hours. The fluorescence activation from each cell line was then captured and analyzed. To examine the integrin αvβ3 expression of each cell line, the cells were cultured, fixed with acetone, and incubated with Alexa Fluor®488-conjugated mouse anti-human integrin αvβ3

© 2013 Macmillan Publishers Limited. All rights reserved.

DOI: 10.1038/NMAT3819

antibody (Millipore, MA) for 1 h, followed by three PBS washes and image capture by confocal microscope.

For colocalization experiments, cells were incubated with LysoTracker® green (50 nM) or MitoTracker® green (100 nM) for 15 min at the end of uptake study for lysosome and mitochondria labeling, respectively. The cells were then washed thrice with PBS. The cells were imaged by a Nikon ECLIPSE TE2000-E confocal microscope with identical settings for each confocal study.

Acute toxicity

Fifteen athymic nude mice (20-24 g, 6-8 weeks) were randomly divided into two groups. The control group contains 5 mice and the experiment group contains 10 mice. *i*UPS integrated nanoprobes (10 mg/kg) were intravenously administrated to the mice in the experiment group via tail vein. Following exposure, the vital signs and mortality of mice in each group were recorded. Half of the mice in the experiment group were sacrificed on day 1 and the remaining half were killed on day 7. The blood samples (~0.8-1 mL/mouse) were centrifuged at 5,000 g for 10 min to separate serum. Liver function was evaluated based on the serum levels of alanine transaminase (ALT) and glutamic oxaloacetic transaminase (GOT). Nephrotoxicity was determined by blood urea nitrogen (BUN) and creatinine (Cr). The tissues of heart, liver, spleen, lung, and kidney were collected and immediately fixed in 10% formalin for histopathological examinations.

References

1. Zhou, K., Wang, Y., Huang, X., Luby-Phelps, K., Sumer, B.D., Gao, J. Tunable, ultrasensitive pH-responsive nanoparticles targeting specific endocytic organelles in living cells. *Angew. Chem. Int. Ed.* 50, 6109-6114 (2011).
2. Tsarevsky, N.V. & Matyjaszewski, K. "Green" atom transfer radical polymerization: from process design to preparation of well-defined environmentally friendly polymeric materials. *Chem. Rev.* **107**, 2270-2299 (2007).
3. Kalyanasundaram, K.; Thomas, J. K., Environmental Effects on Vibronic Band Intensities in Pyrene Monomer Fluorescence and Their Application in Studies of Micellar Systems. *J. Am. Chem. Soc.* **1977,** *99*, 2039-2044.
4. Winnik, F. M., Photophysics of Preassociated Pyrenes in Aqueous Polymer-Solutions and in Other Organized Media. *Chem. Rev.* **1993,** *93*, 587-614.
5. Yang C., Sudderth J., Dang T., Bachoo R.G., McDonald J.G., DeBerardinis R.J. Glioblastoma Cells Require Glutamate Dehydrogenase to Survive Impairments of Glucose Metabolism or Akt Signaling. *Cancer Res.* 69, 7986-93 (2009).

© 2013 Macmillan Publishers Limited. All rights reserved.

Supplementary Table S1. Characterization of PEG_{114}-*b*-P(DPA_m-*co*-$Cy5.5_3$) copolymers with different repeating units of PDPA segment but the same dye content (i.e. 3 Cy5.5) and the resulting nanoprobe properties.

Copolymer	M_n (kDa)[a]	Repeat unit[b]	CMC (μg/mL)	Particle size (nm)	pH_t	$\Delta pH_{10\text{-}90\%}$	R_F (F_{max}/F_{min})[c]
$PDPA_{40}$-$(Cy5.5)_3$	13.4	39	2.48	15.5±1.4	6.24	0.29	145
$PDPA_{60}$-$(Cy5.5)_3$	17.6	59	1.27	17.4±1.7	6.22	0.23	110
$PDPA_{80}$-$(Cy5.5)_3$	22.3	81	1.18	25.6±2.8	6.21	0.20	82
$PDPA_{100}$-$(Cy5.5)_3$	26.3	100	0.79	36.9±4.7	6.17	0.20	59

[a] Number-averaged molecular weights (M_n) were determined by GPC using THF as the eluent; [b]Repeating unit was calculated based on integrations of -CH_2-O- groups on PDPA to the methylene groups on PEG using ^{1}HNMR; [c]Determined by Cy5.5 fluorescence emission intensity.

Supplementary Table S2. Characterization of PEG_{114}-*b*-P(DPA_{80}-*co*-$Cy5.5_n$) copolymers with different Cy5.5 content but the same repeating unit of PDPA and the resulting nanoprobe properties.

Copolymer	M_n (kDa)[a]	Repeat unit[b]	CMC (μg/mL)	Particle size (nm)	pH_t	$\Delta pH_{10\text{-}90\%}$	R_F (F_{max}/F_{min})[c]
$PDPA_{80}$-$(Cy5.5)_1$	23.1	85	0.88	27.2±2.1	6.18	0.19	6.6
$PDPA_{80}$-$(Cy5.5)_3$	22.3	81	1.18	25.6±2.8	6.21	0.20	82
$PDPA_{80}$-$(Cy5.5)_6$	21.5	77	1.32	25.9±1.8	6.20	0.20	134

[a] Number-averaged molecular weights (M_n) were determined by GPC using THF as the eluent; [b]Repeating unit was calculated based on integrations of -CH_2-O- groups on PDPA to the methylene groups on PEG using ^{1}HNMR; [c]Determined by Cy5.5 fluorescence emission intensity.

© 2013 Macmillan Publishers Limited. All rights reserved.

DOI: 10.1038/NMAT3819

Supplementary Table S3. Test of batch reproducibility of PEG_{114}-*b*-P(DPA_{80}-*co*-$Cy5.5_6$) copolymers and resulting nanoprobes (4 batches were synthesized at different times using the same theoretical compositions).

Batch	M_n, GPC (kDa) [a]	M_w, GPC (kDa) [a]	M_n, ^{1}H-NMR (kDa)	PDI	pH_t	$\Delta pH_{10\text{-}90\%}$	R_F (F_{max}/F_{min}) [b]
Batch 1	20.1	23.1	21.0	1.15	6.20	0.20	135
Batch 2	21.0	24.8	21.6	1.18	6.20	0.21	128
Batch 3	21.2	25.6	21.8	1.21	6.21	0.20	125
Batch 4	21.5	25.8	21.2	1.20	6.21	0.20	134

[a] Number-averaged (M_n) were determined by GPC using THF as the eluent; [b] Determined by Cy5.5 fluorescence emission intensity.

Supplementary Table S4. Characterization of UPS nanoprobes and always-ON nanoprobes that are used for the biological studies.

Nanoprobes	Particle Size (nm)[a]	Zeta potential (mV)	R_F (F_{max}/F_{min}) [b]	$\Delta pH_{10\text{-}90\%}$	pH_t
UPS_e	25.3 ± 1.5	-0.72 ± 1.07	102	0.23	6.90
UPS_i	24.9 ± 0.8	-3.52 ± 0.60	135	0.21	6.21
cRGD-UPS_i	24.5 ± 1.1	-2.79 ± 0.30	128	0.21	6.21
PC7A always-ON	25.8 ± 1.7	-0.26 ± 0.49	1.05	-	-
cRGD-encoded PDPA always-ON	25.5 ± 0.9	-2.13 ± 0.65	1.15	-	-

[a] Measured from TEM, mean ± s.d.; [b] Determined by Cy5.5 fluorescence emission intensity.

© 2013 Macmillan Publishers Limited. All rights reserved.

Supplementary Table S5. Biodistribution and tissue fluorescence of the UPS_e nanoprobes (n = 4) at 24 h.

Organs	NIRF signal	%ID/g tissue	NIRF signal/ (%ID/g) ratio [a]
Blood	4 ± 1	6.62±0.14	1
Heart	26 ± 11	0.54±0.11	74
Liver	1071 ± 276	32.1±2.82	52
Spleen	166 ± 50	19.9±4.34	13
Lung	91 ± 25	1.57±0.23	90
Kidney	60 ± 17	1.90±0.21	49
Tumor	545 ± 88	2.42±0.73	355
Muscle	42 ± 15	1.03±0.21	64
Pancreas	9 ± 2	0.21±0.06	63

[a] Tumor and organ NIRF signal/(%ID/g) ratios were normalized to blood to yield the organ to blood ratios (OBRs).

© 2013 Macmillan Publishers Limited. All rights reserved.

DOI: 10.1038/NMAT3819

Supplementary Table S6. Biodistribution and tissue fluorescence of the UPS_i nanoprobes (n = 4) at 6 and 24 h.

Organs	NIRF signal (6 h)	%ID/g tissue (6 h)	%ID/g tissue (24 h)	NIRF signal/ (%ID/g) ratio [a]
Blood	22 ± 5	59.1±5.42	31.6±3.18	1
Heart	27 ± 13	0.83±0.28	1.02±0.18	88
Liver	864 ± 189	7.71±1.71	7.92±1.78	299
Spleen	122 ± 28	8.63±1.83	10.92±2.13	37
Lung	56 ± 17	0.89±0.35	2.18±1.01	168
Kidney	84 ± 24	1.39±0.56	2.57±0.95	162
Tumor	62 ± 19	2.11±0.59	3.04±1.25	78
Muscle	40 ± 8	0.90±0.22	1.44±0.47	119

[a] Tumor and organ NIRF signal/(%ID/g) ratios were normalized to blood to yield the organ to blood ratios (OBRs).

Supplementary Table S7. Biodistribution and tissue fluorescence of the cRGD-UPSi nanoprobes (n = 4) at 6 and 24 h.

Organs	NIRF signal (6 h)	%ID/g tissue (6 h)	%ID/g tissue (24 h)	NIRF signal/ (%ID/g) ratio [a]
Blood	24 ± 7	47.7±3.57	22.9±1.39	1
Heart	32 ± 8	0.80±0.19	1.04±0.33	80
Liver	1049 ± 302	8.16±1.70	10.07±2.74	257
Spleen	213 ± 61	11.1±1.60	16.12±3.07	38
Lung	94 ± 19	1.02±0.32	1.92±0.77	184
Kidney	117 ± 43	1.74±0.59	2.00±0.31	134
Tumor	783 ± 136	2.49±0.44	3.42±1.08	628
Muscle	49 ± 12	1.07±0.24	1.32±0.51	91

[a] Tumor and organ NIRF signal/(%ID/g) ratios were normalized to blood to yield the organ to blood ratios (OBRs).

© 2013 Macmillan Publishers Limited. All rights reserved.

Supplementary Figures:

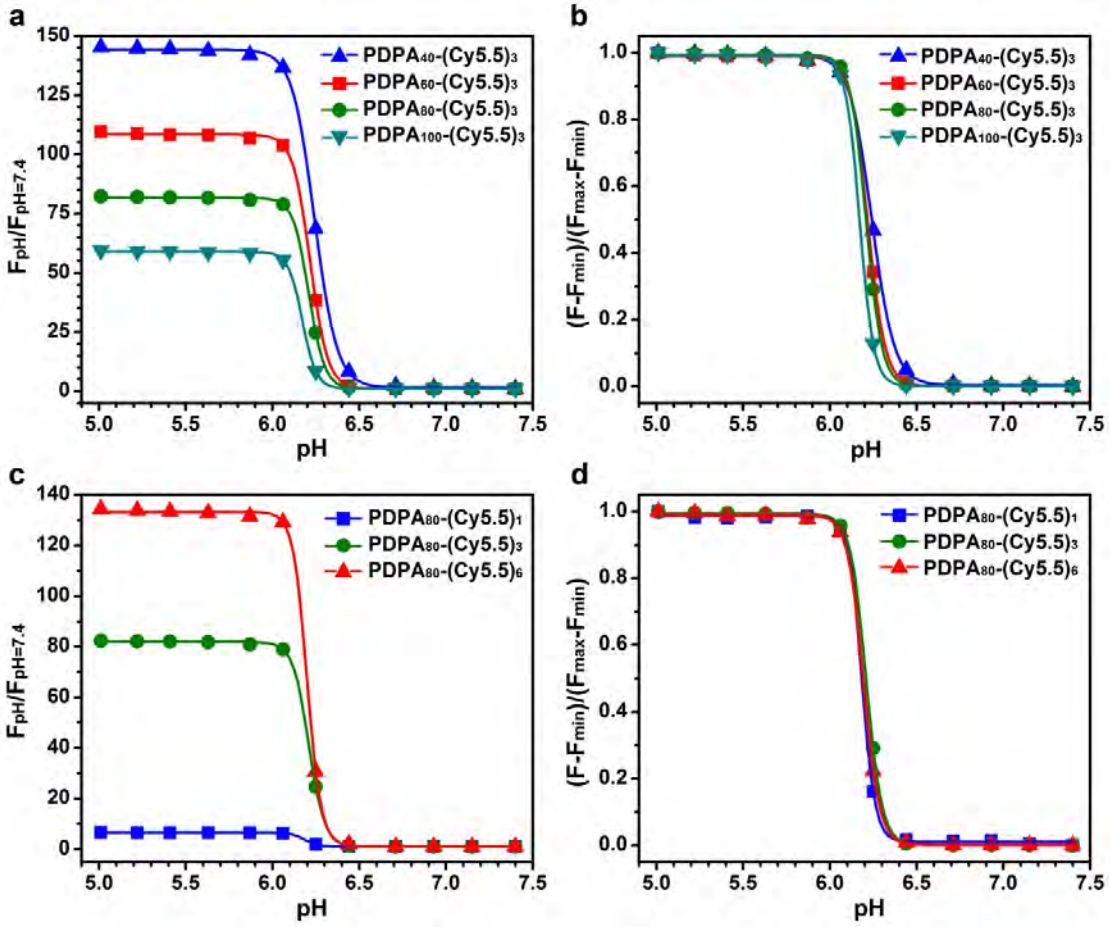

Supplementary Figure S1. Investigation of the influence of pH-sensitive segment (**a**-**b**) and dye content (**c**-**d**) on the nanoprobe properties using PEG_{114}-*b*-P(DPA_m-*co*-$Cy5.5_n$) as a model copolymer. (**a**) Fluorescence activation ratio and (**b**) normalized fluorescence intensity of PEG_{114}-*b*-P(DPA_m-*co*-$Cy5.5_3$) micelles as a function of pH. m is the repeating unit of PDPA and was controlled at 40, 60, 80 and 100. The Cy5.5 number was kept at 3 per polymer. In **b**, the pH_t of PEG_{114}-*b*-P(DPA_m-*co*-$Cy5.5_3$) micelles varies from 6.17 to 6.24. The sharpness of pH transition slightly decreased at shorter PDPA chain length. (**c**) Fluorescence activation ratio and (**d**) normalized fluorescence intensity of PEG_{114}-*b*-P(DPA_{80}-*co*-$Cy5.5_n$) nanoprobes. The repeating unit of PDPA is kept at 80 and the Cy5.5 number is controlled at 1, 3 and 6 per polymer. The pH_t of PEG_{114}-*b*-P(DPA_{80}-*co*-$Cy5.5_n$) micelles is between 6.18 to 6.21. The sharpness of nanoprobes is from 0.19 to 0.20. Each sample was excited at 675 nm, and emission spectrum was collected from 690 to 780 nm. The polymer concentrations were 0.1 mg/mL.

© 2013 Macmillan Publishers Limited. All rights reserved.

DOI: 10.1038/NMAT3819

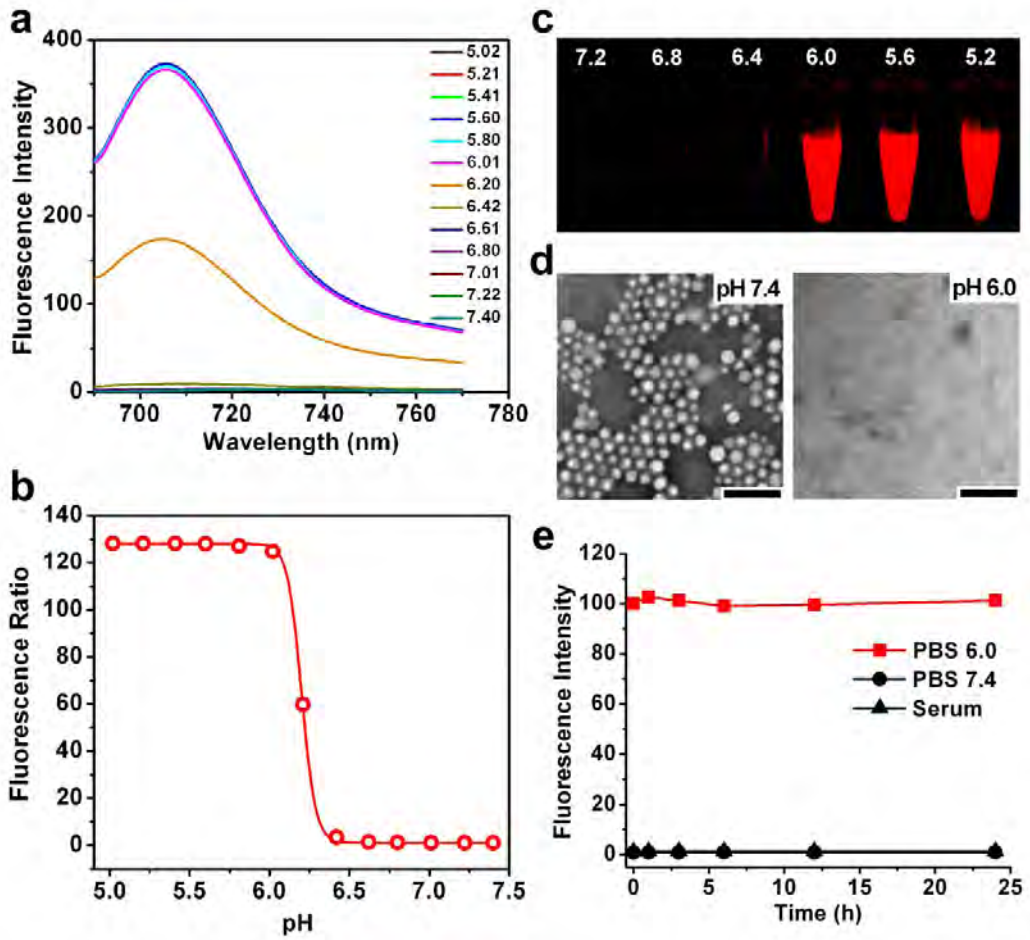

Supplementary Figure S2. Characterization of cRGD-UPS$_i$ nanoprobes. (**a**) pH-dependent fluorescence spectra of cRGD-UPS$_i$ nanoprobes. Each sample is excited at 675 nm, and emission spectra are collected from 690 to 780 nm. The polymer concentrations were 0.1 mg/mL. (**b**) Fluorescence ratio as a function of pH for cRGD-UPS$_i$ nanoprobes. The pH response ($\Delta pH_{10\text{-}90\%}$) is 0.21 pH unit and signal amplification is 128-fold. (**c**) Fluorescence signal amplification of cRGD-UPS$_i$ nanoprobes as a function of pH. Fluorescence images were captured on Maestro *in vivo* imaging system (CRI) using the "orange" filter (640-820 nm). (**d**) Transmission electron microscopes of cRGD-UPS$_i$ nanoprobes in pH 7.4 and 6.0 buffers at the polymer concentration of 1 mg/mL. Scale bar is 100 nm. (**e**) cRGD-UPS$_i$ nanoprobes remain stable in fresh mouse serum over 24 h at 37 °C.

© 2013 Macmillan Publishers Limited. All rights reserved.

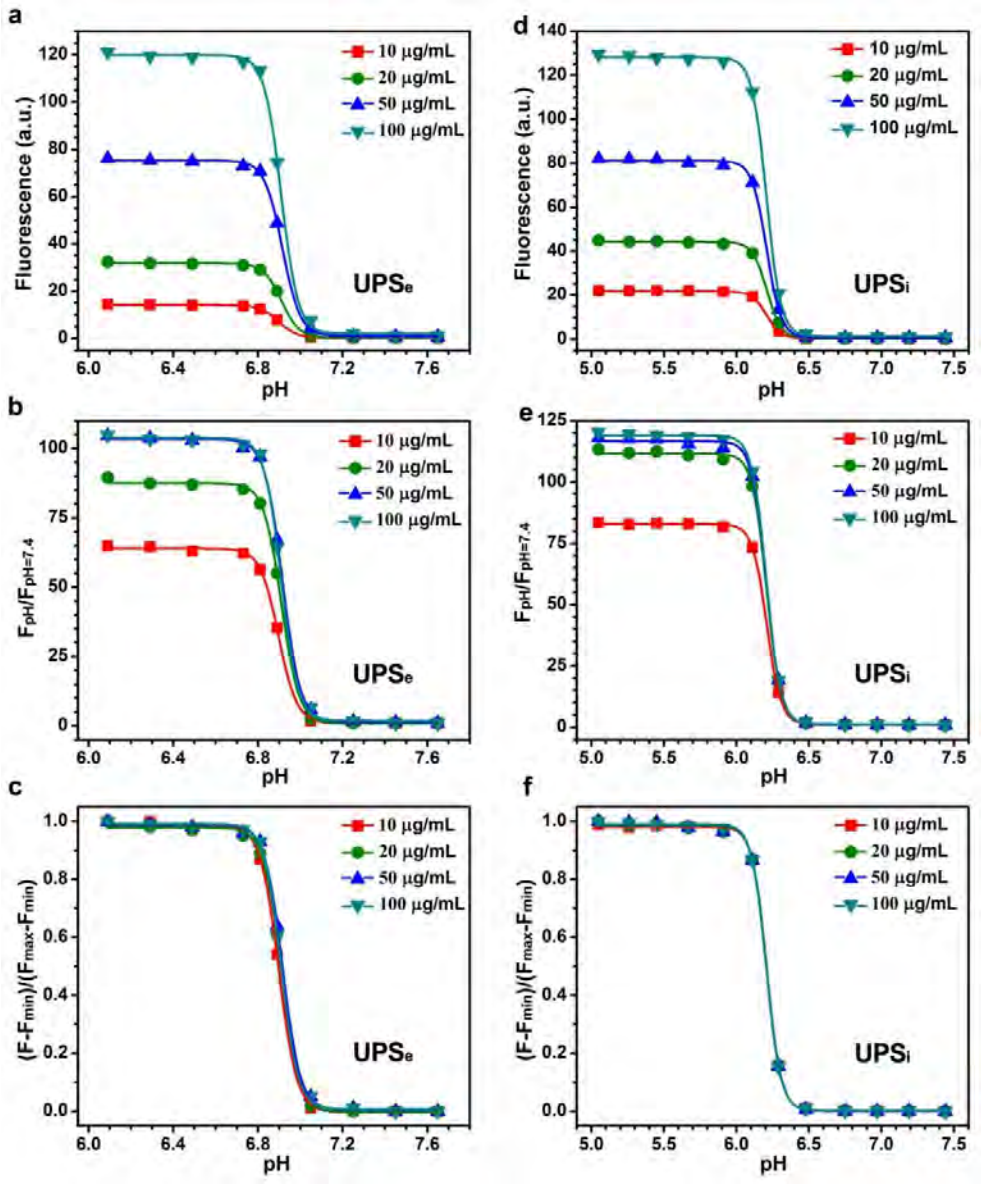

Supplementary Figure S3. Investigation of UPS_e/UPS_i dilution on the nanoprobe performance. For UPS_e nanoprobes, fluorescence intensity (**a**), fluorescence activation ratio (**b**) and normalized fluorescence intensity (**c**) were plotted as a function of pH at different polymer concentrations from 10 to 100 μg/mL. For UPS_i nanoprobes, fluorescence intensity (**d**), fluorescence activation ratio (**e**) and normalized fluorescence intensity (**f**) were plotted as a function of pH at different polymer concentrations from 10 to 100 μg/mL. Results show that fluorescence intensity decreased at lower probe concentrations as expected, but the ON/OFF activation ratio remained high (>60-fold) even at 10 μg/mL. Normalization of fluorescence signals showed superimposable, sharp pH transitions in this concentration range, indicating high fidelity of the current UPS platform. Each sample is excited at 675 nm, and emission spectra are collected from 690 to 780 nm.

© 2013 Macmillan Publishers Limited. All rights reserved.

DOI: 10.1038/NMAT3819

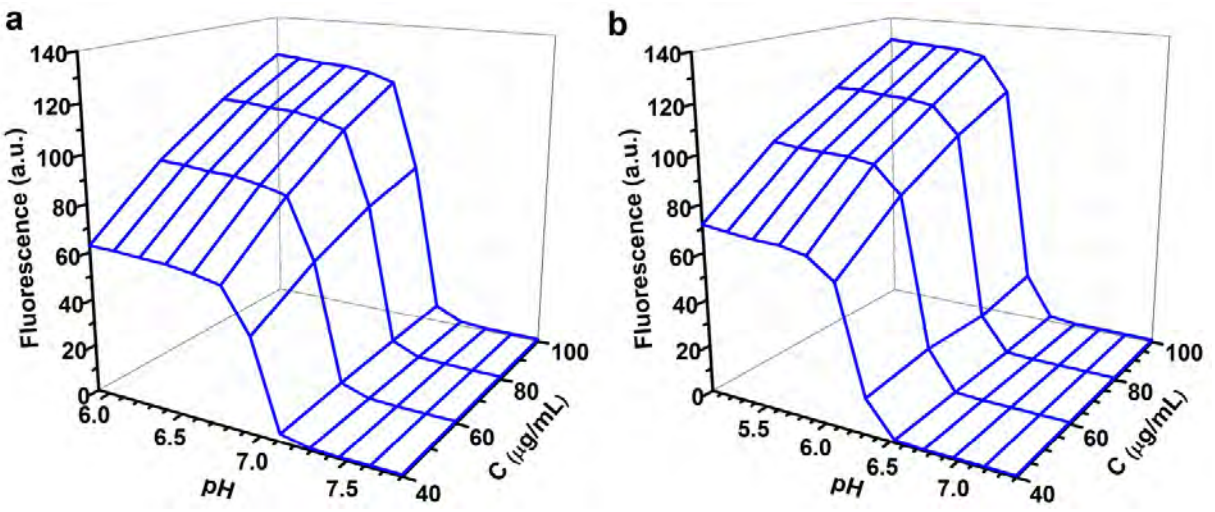

Supplementary Figure S4. Three dimensional (3-D) plots of fluorescence intensity as a function of UPS_e (**a**) and UPS_i (**b**) nanoprobe concentration and pH. These 3-D plots illustrate the pH-modulated signal amplification/suppression strategy orthogonal to dose accumulation. In normal tissue and blood pH (7.2-7.4), the nanoprobes are silent due to the homo-FRET induced fluorescence quenching. Below the transition pH (i.e., 6.9 and 6.2 for UPS_e and UPS_i, respectively), the fluorescence intensity exponentially increased as a result of micelle dissociation.

© 2013 Macmillan Publishers Limited. All rights reserved.

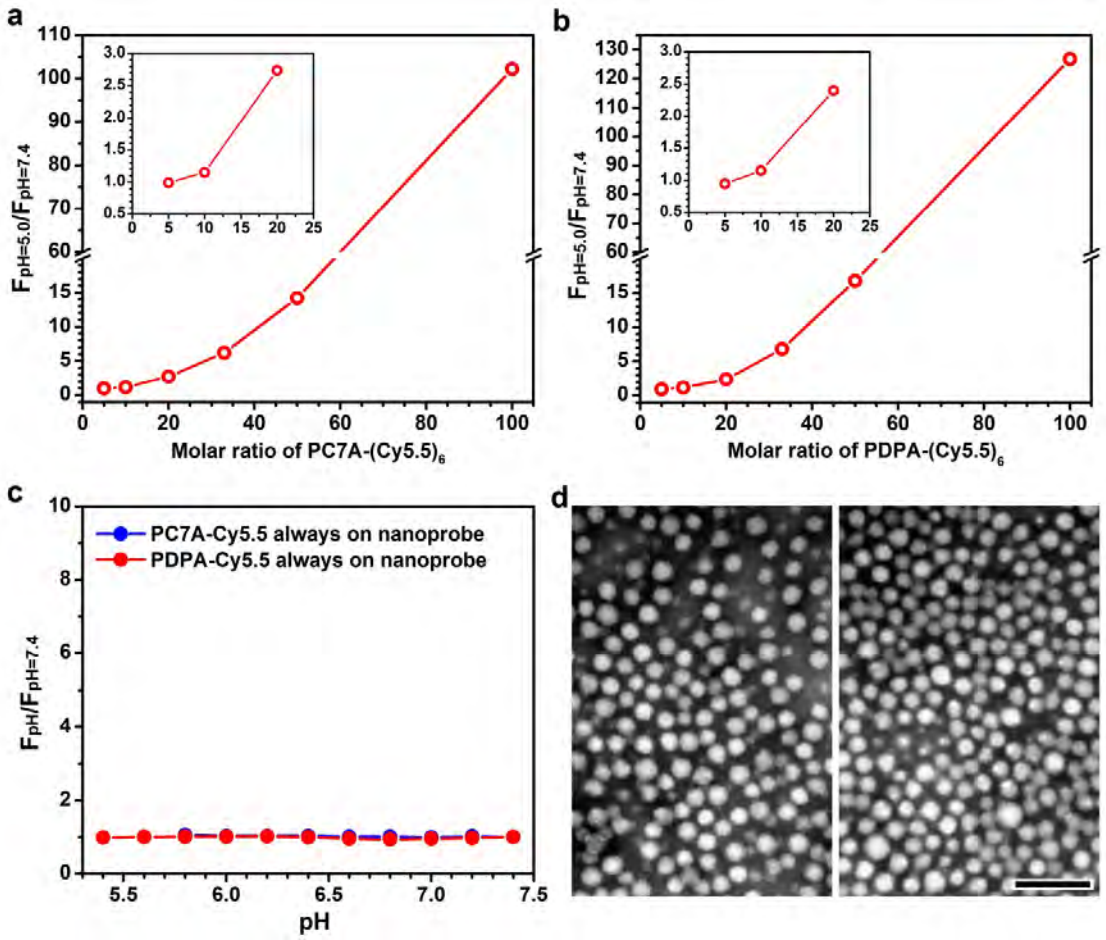

Supplementary Figure S5. Development and characterization of always-ON nanoprobe controls for UPS_e and UPS_i. (**a**) Fluorescence intensity ratio as a function of molar ratio of PEG-*b*-P($C7A_{65}$-*co*-$Cy5.5_6$) over dye-free PEG-*b*-P($C7A_{65}$-*co*-AMA_6) in the co-mixed micelles. (**b**) Fluorescence intensity ratio as a function of molar ratio of PEG-*b*-P(DPA_{80}-*co*-$Cy5.5_6$) over dye-free PEG-*b*-P(DPA_{80}-*co*-AMA_6) in the co-mixed micelles. The insets in **a** and **b** showed the fluorescence intensity ratios were ~1.0 with 5mol% of dye-conjugated polymers, and therefore were chosen as the always-ON controls. (**c**) Fluorescence activation ratios of the two always-ON nanoprobes showing no pH-sensitive response. Each sample is excited at 675 nm, and emission spectra are collected from 690 to 780 nm. The polymer concentrations were 0.1 mg/mL. (**d**) TEM images of PC7A always-ON (left) and cRGD-encoded PDPA always-ON (right) nanoprobes from their solutions at pH 7.4. The scale bar is 100 nm. These always-ON controls showed comparable particle diameter and surface zeta potential (**Table S4**) as their corresponding UPS_e/UPS_i nanoprobes.

© 2013 Macmillan Publishers Limited. All rights reserved.

DOI: 10.1038/NMAT3819

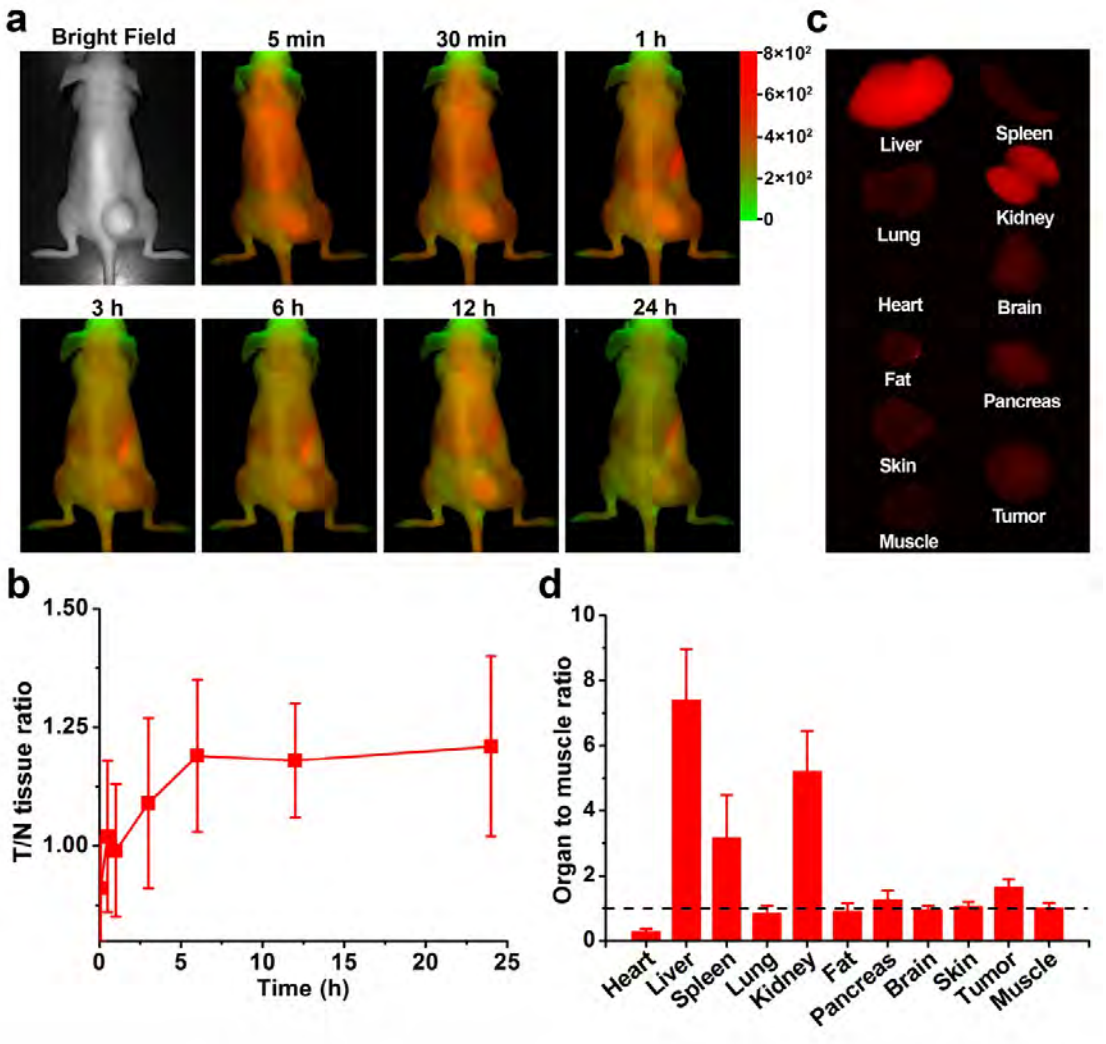

Supplementary Figure S6. Cy5.5-labeled PEG-*b*-PC7A always-ON nanoprobe for A549 tumor imaging *in vivo* and *ex vivo*. (a) Nude mice bearing A549 tumors were injected with a dosage of 25 mg/kg always-ON nanoprobe and, NIR fluorescence images at selected time-points were captured. The mice autofluorescence is color coded green while the unmixed probe signal is coded red. (b) *In vivo* time-dependent average fluorescence intensity ratio between tumor and normal tissue after the probe injection. (c) At 24 h post-injection, mice were sacrificed and collected organs were visualized. (d) Organ to muscle ratios for always-ON nanoprobe in A549 tumor-bearing mice. The fluorescent signal of organs was normalized to the fluorescent signal in the muscle. Data are presented as mean ± s.d. (n = 3).

© 2013 Macmillan Publishers Limited. All rights reserved.

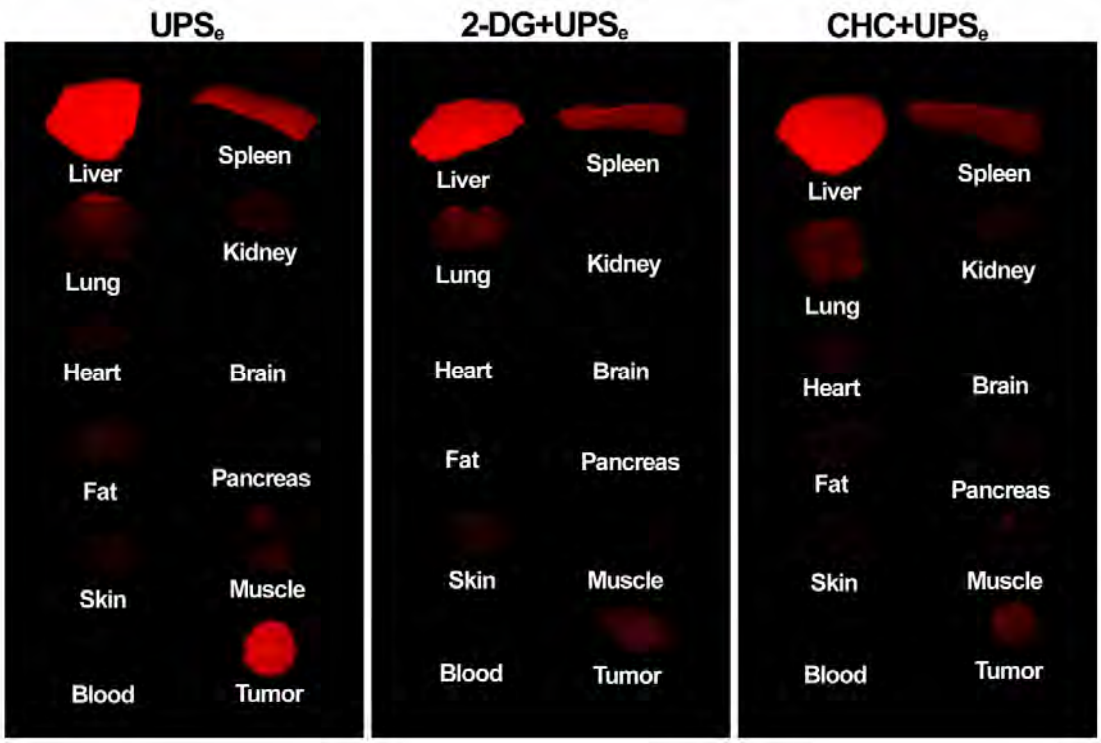

Supplementary Figure S7. Representative *ex vivo* fluorescence images of dissected tumors and organs of A549 tumor-bearing mice sacrificed at 24 h post-injection. A549 tumor-bearing mice were intravenously administered with UPS_e nanoprobes at a dose of 10 mg/kg and, 24 h later, organs were collected for NIR imaging. In the control groups, 2-DG (250 mg/kg) or CHC (250 mg/kg) was injected 12 h before the UPS_e nanoprobe administration.

© 2013 Macmillan Publishers Limited. All rights reserved.

DOI: 10.1038/NMAT3819

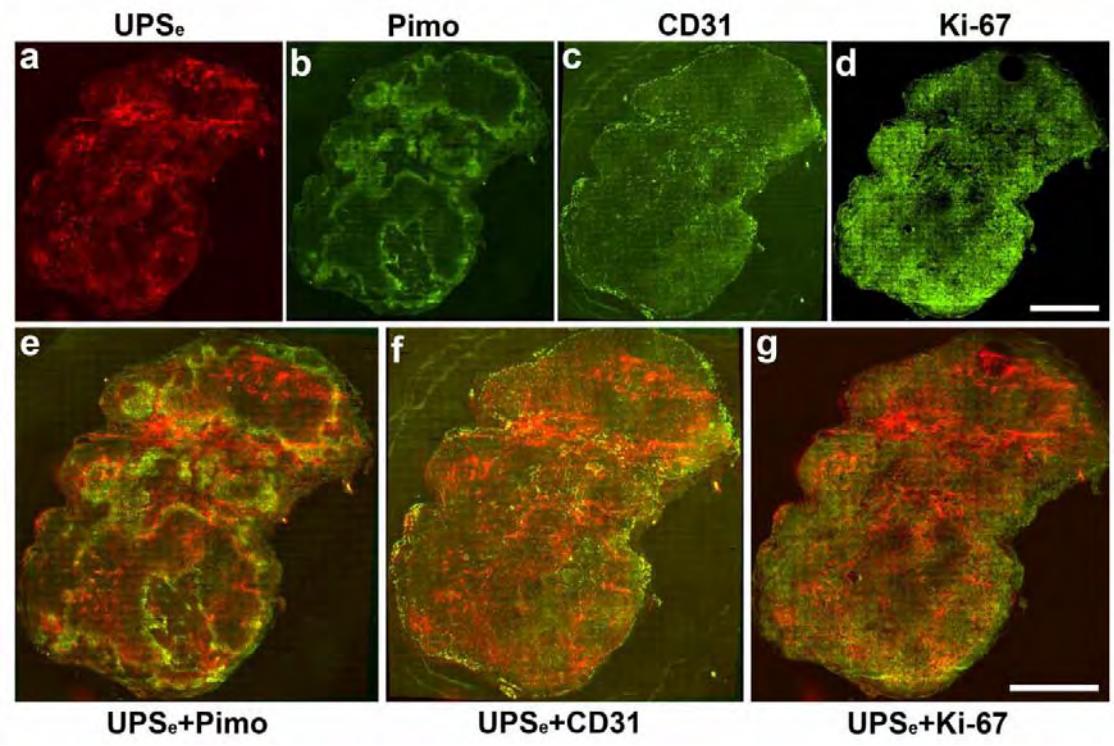

Supplementary Figure S8. Representative correlation of UPS_e nanoprobe images with histologically stained whole mount cryosections. Top (from left to right), (**a**) UPS_e nanoprobe signals, (**b**) pimonidazole for hypoxia staining, (**c**) tumor vasculature stained with CD31 antibody, (**d**) Ki-67 for cell proliferation staining. Bottom, merged images (from left to right), (**e**) UPS_e nanoprobe (red) and pimonidazole (green); (**f**) UPS_e nanoprobe (red) and CD31 (green); (**g**) UPS_e nanoprobe (red) and Ki-67 (green). All images were obtained from the adjacent sections at ×200 magnification. Scale bar is 2 mm.

© 2013 Macmillan Publishers Limited. All rights reserved.

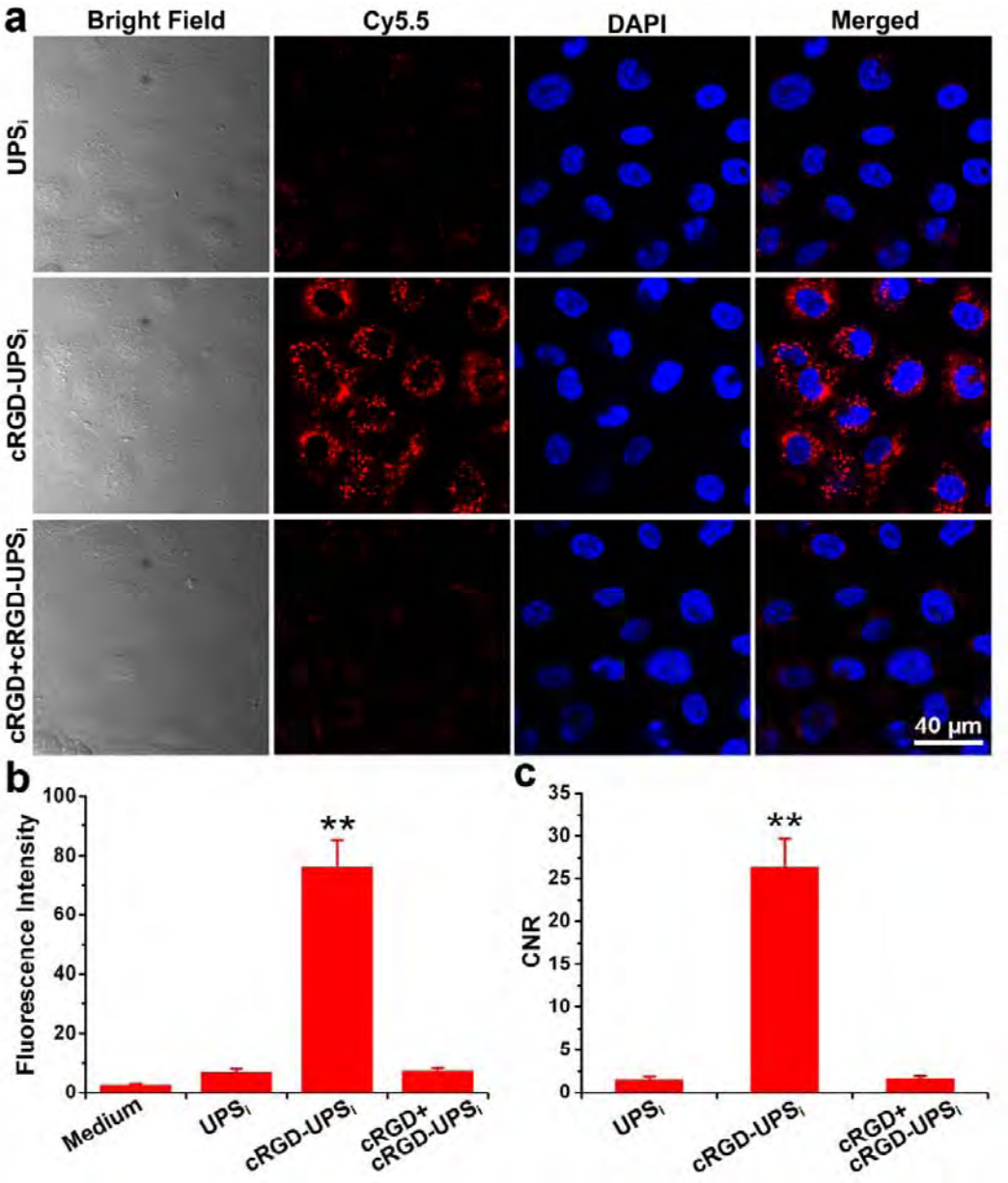

Supplementary Figure S9. Fluorescence activation of cRGD-UPS_i nanoprobes in HUVEC cells. (**a**) Representative confocal images of "activated" cRGD-UPS_i nanoprobes in HUVEC cells. UPS_i and free cRGD block were used as controls. (**b**) Fluorescence intensity of HUVEC cells treated with different nanoprobes (N > 100 for each group) and cell culture medium. (**c**) Contrast to noise ratio (CNR) of HUVEC cells treated with cRGD-UPS_i over the UPS_i and free cRGD+cRGD-UPS_i controls. $^{**}P < 0.01$, compared with other two groups.

© 2013 Macmillan Publishers Limited. All rights reserved.

DOI: 10.1038/NMAT3819

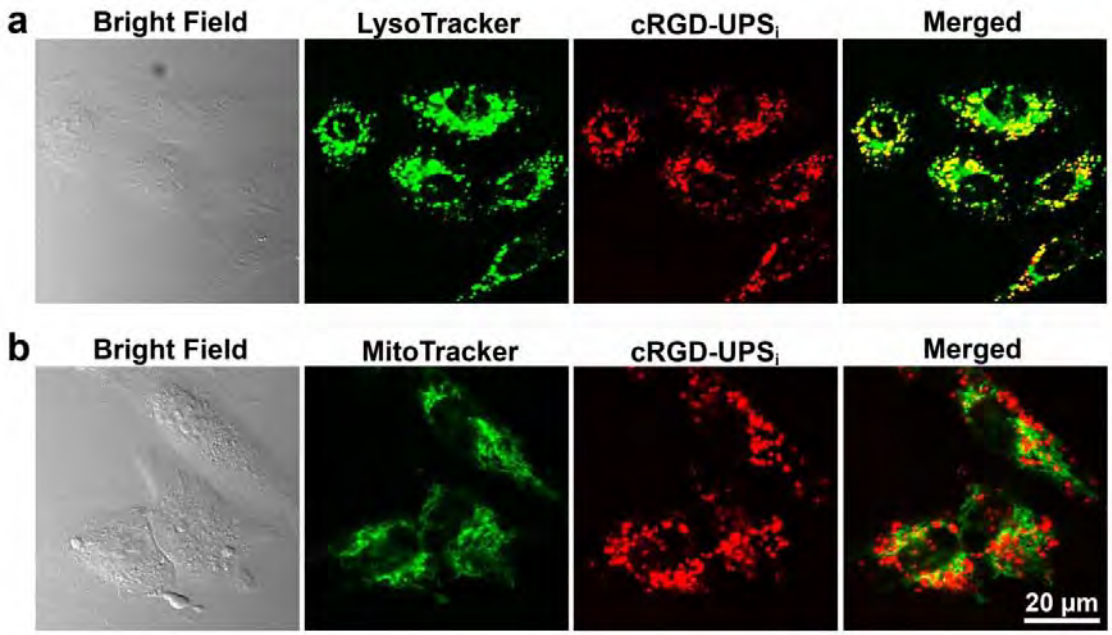

Supplementary Figure S10. Subcellular activation and distribution of cRGD-UPS_i nanoprobes in HUVECs. HUVECs were incubated in the presence of cRGD-UPS_i for 3 h. Confocal images of cells stained with either (**a**) LysoTracker DND-26 (green) or (**b**) MitoTracker Green FM (green) were captured and the pictures were superimposed. Red color represents the nanoprobe signals. Yellow color is an indication for colocalization of nanoprobes with lysosomes.

© 2013 Macmillan Publishers Limited. All rights reserved.

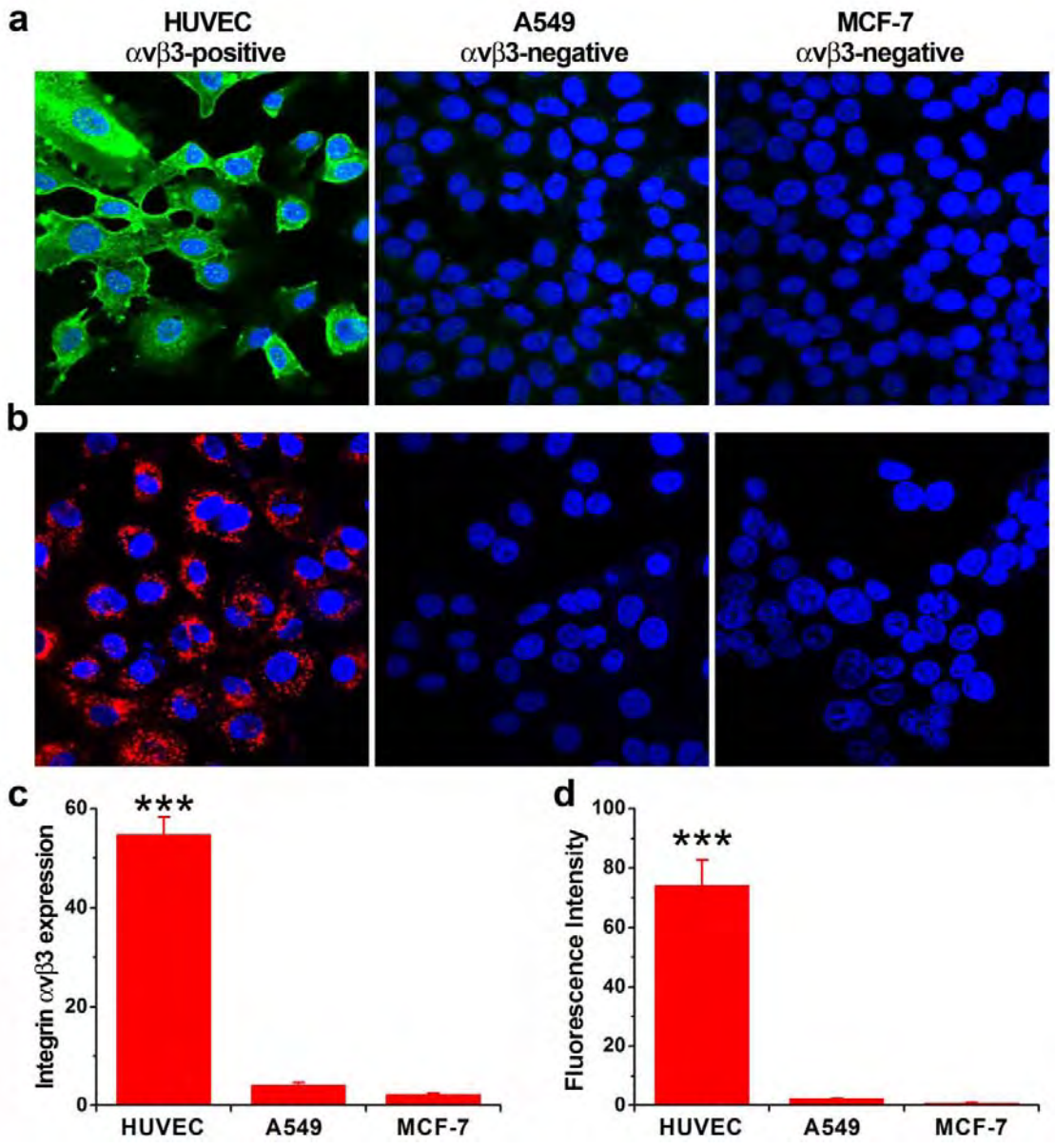

Supplementary Figure S11. Integrin αvβ3-dependent fluorescence activation by HUVEC, A549, and MCF-7 cells. (**a**) Immunocytochemistry analysis of integrin αvβ3 expression in different cells. (**b**) Representative confocal images of cRGD-UPS$_i$ nanoprobe activation in different cells. (**c**) Quantification of integrin $\alpha_v\beta_3$ expression ($N > 100$ for each group). ***$P < 0.001$, compared with other two groups. (**d**) Fluorescence intensity of different cells treated with cRGD-UPS$_i$ nanoprobes ($N > 100$ for each group). ***$P < 0.001$, compared with other two groups.

© 2013 Macmillan Publishers Limited. All rights reserved.

DOI: 10.1038/NMAT3819

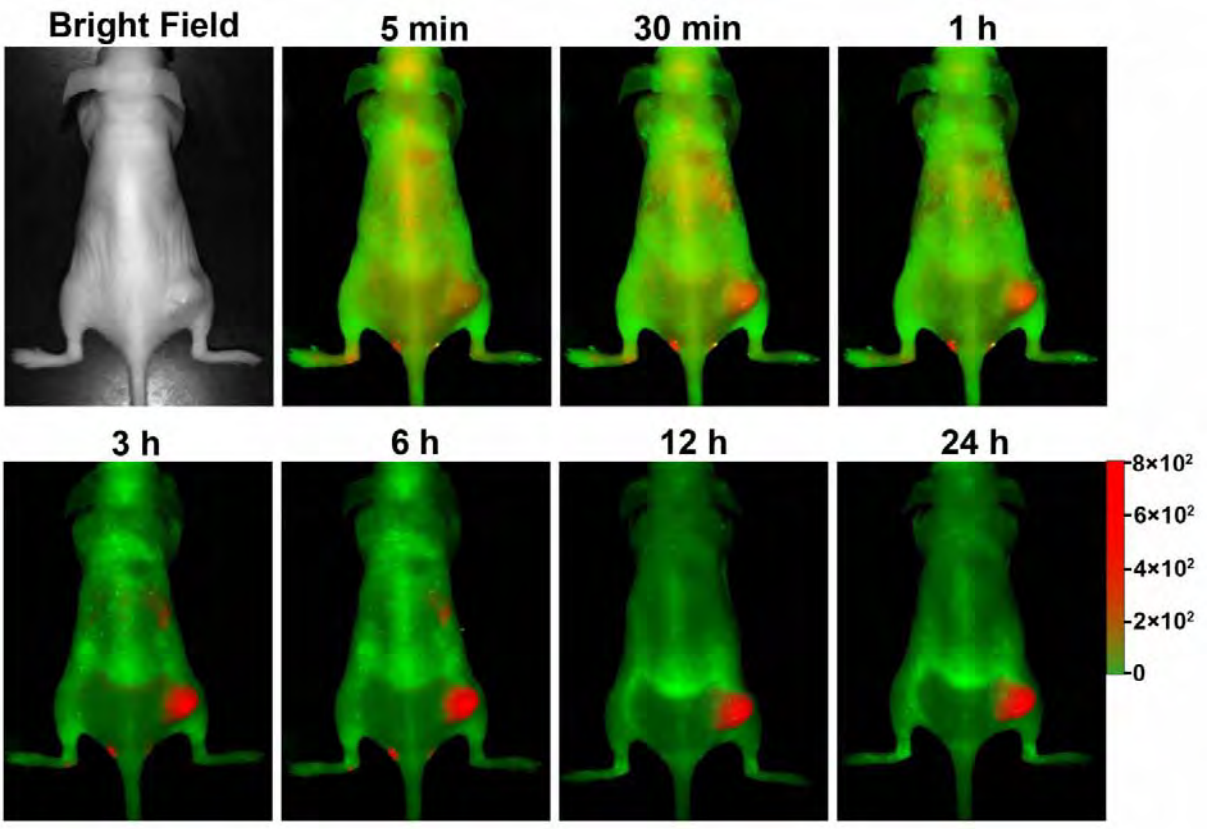

Supplementary Figure S12. Specific signal amplification of cRGD-UPS$_i$ nanoprobes for A549 tumor imaging *in vivo*. Athymic (*nu/nu*) mice bearing A549 tumors were injected with a dosage of 10 mg/kg nanoprobe and, NIR fluorescence images at selected time points were captured. The mice autofluorescence is color coded green while the unmixed nanoprobe signal is coded red.

© 2013 Macmillan Publishers Limited. All rights reserved.

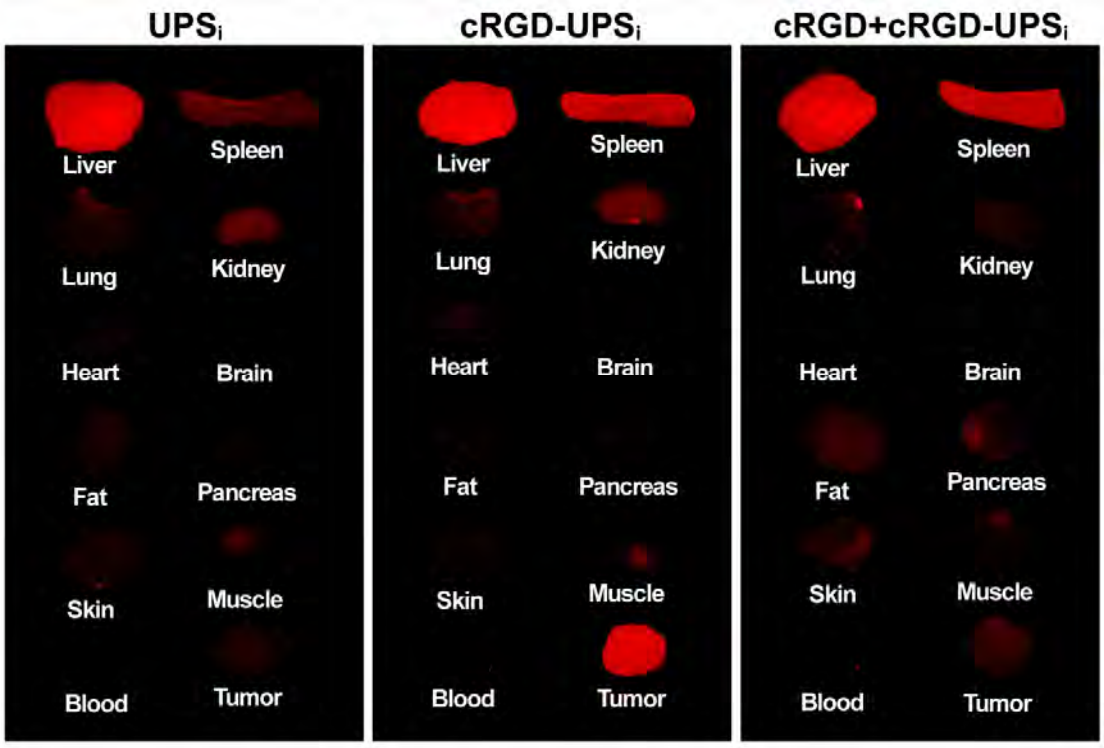

Supplementary Figure S13. Representative *ex vivo* fluorescence images of dissected tumors and organs of A549 tumor-bearing mice sacrificed at 6 h post-injection. A549 tumor-bearing mice were intravenously injected with cRGD-UPS_i or UPS_i at a dose of 10 mg/kg and, 6 h later, tumors and organs were collected for NIR imaging. In the competition group, a blocking dose of cRGDfK peptide (25 mg/kg) was injected 30 min prior to the cRGD-UPS_i nanoprobe administration.

© 2013 Macmillan Publishers Limited. All rights reserved.

DOI: 10.1038/NMAT3819

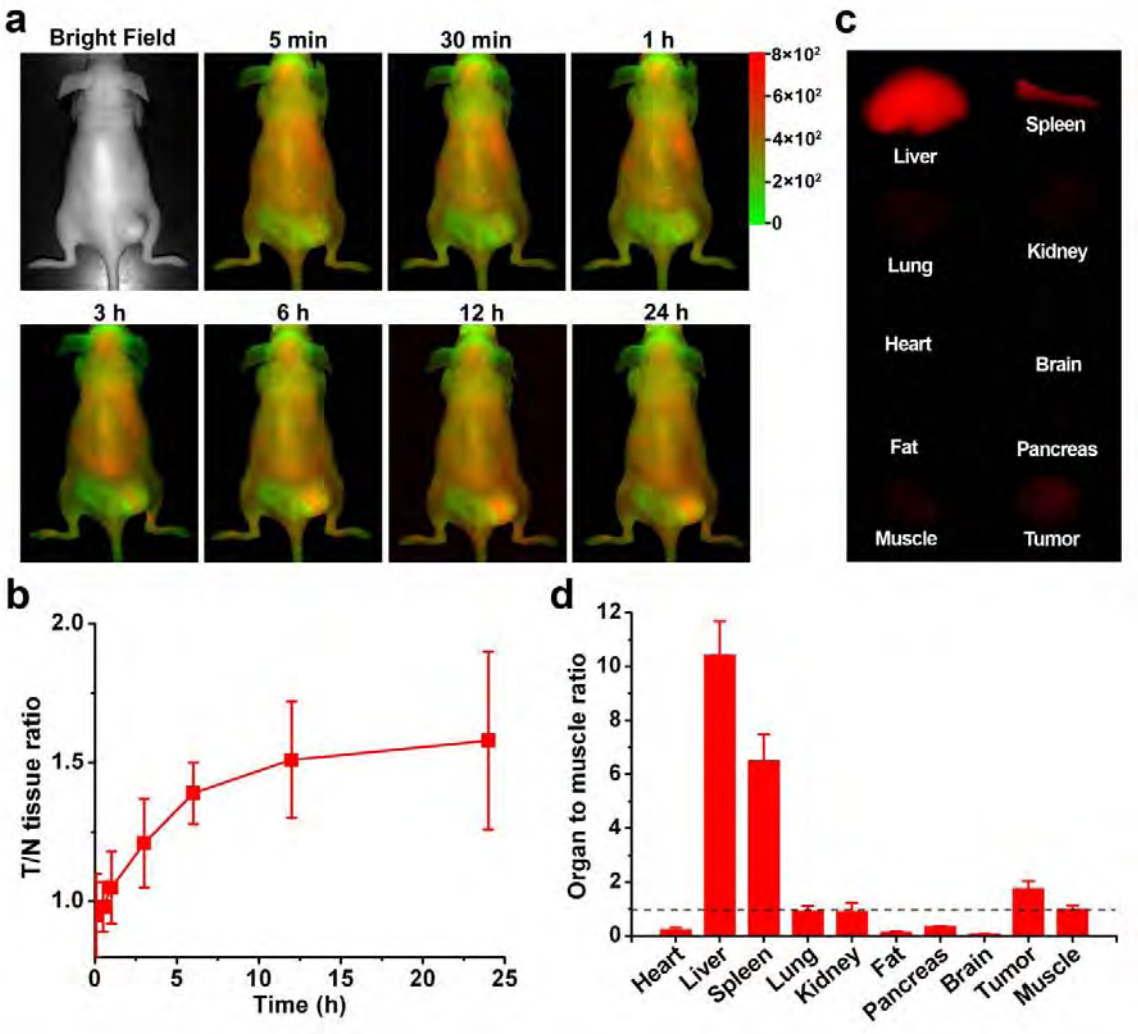

Supplementary Figure S14. cRGD-encoded, Cy5.5-labeled PEG-*b*-PDPA always-ON nanoprobe for A549 tumor imaging *in vivo* and *ex vivo*. (a) Nude mice bearing A549 tumors were injected with a dosage of 25 mg/kg always-ON nanoprobe and, NIR fluorescence images at selected time-points were captured. The mice autofluorescence is color coded green while the unmixed probe signal is coded red. (b) *In vivo* time-dependent average fluorescence intensity ratio between tumor and normal tissue after the probe injection. (c) At 24 h post-injection, mice were sacrificed and collected organs were visualized. (d) Organ to muscle ratios for always-ON nanoprobe in A549 tumor-bearing mice. The fluorescent signal of organs was normalized to the fluorescent signal in the muscle. Data are presented as mean ± s.d. (n = 3).

© 2013 Macmillan Publishers Limited. All rights reserved.

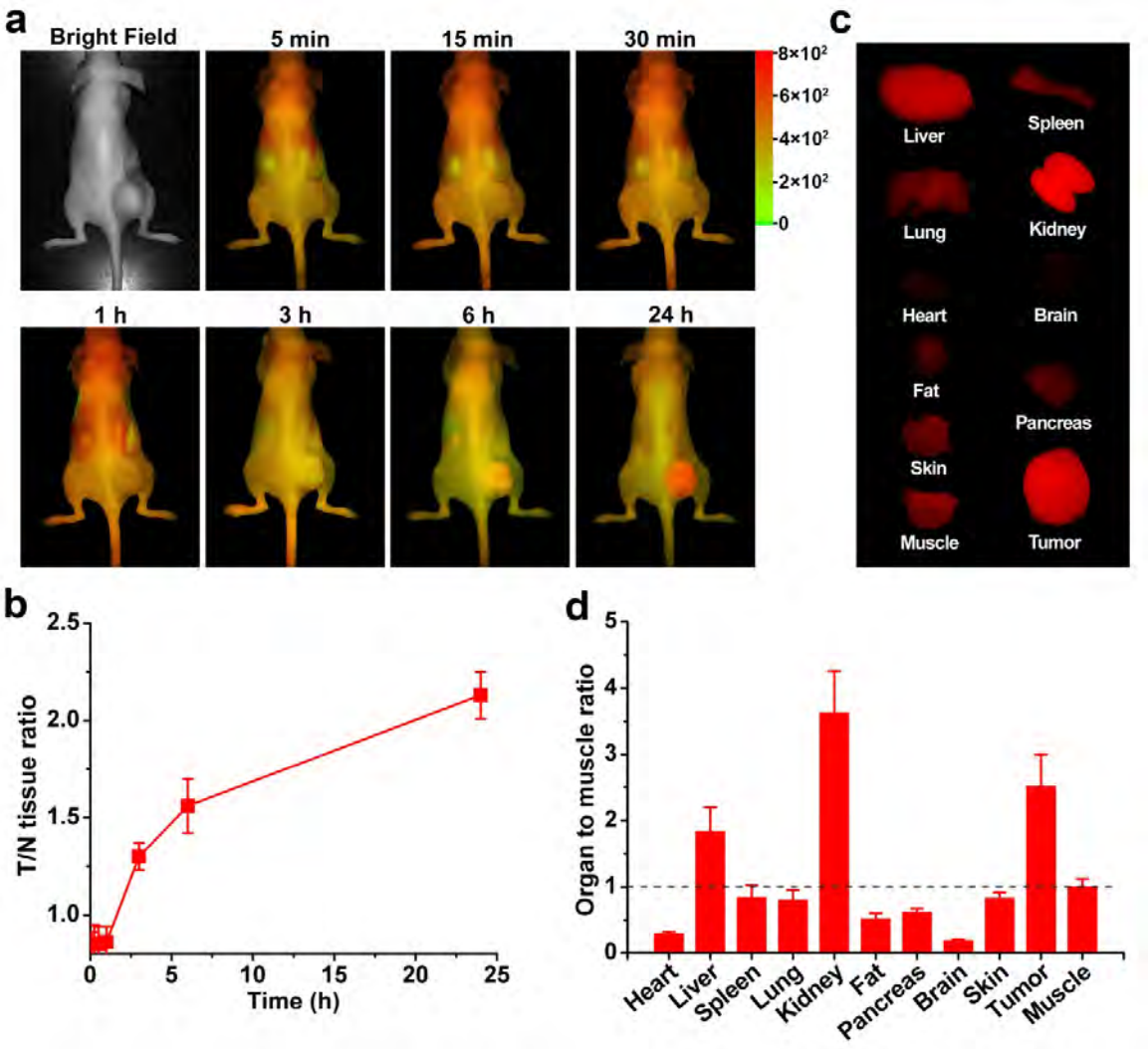

Supplementary Figure S15. IRDye®800CW-cRGD Optical Probe for A549 tumor imaging *in vivo* and *ex vivo*. (**a**) Athymic (*nu/nu*) mice bearing A549 tumors were injected with a dosage of 2 nmol/mouse IRDye®800CW-cRGD probe and, NIR fluorescence images at selected time-points were captured. The mice autofluorescence is color coded green while the unmixed probe signal is coded red. (**b**) *In vivo* time-dependent average fluorescence intensity ratio between tumor and normal tissue after the probe injection. (**c**) At 24 h post-injection, mice were sacrificed and collected organs were visualized. (**d**) Organ to muscle ratios for IRDye®800CW-cRGD probe in A549 tumor-bearing mice. The fluorescent signal of organs was normalized to the fluorescent signal in the muscle. Data are presented as mean ± s.d. (n = 3).

© 2013 Macmillan Publishers Limited. All rights reserved.

DOI: 10.1038/NMAT3819

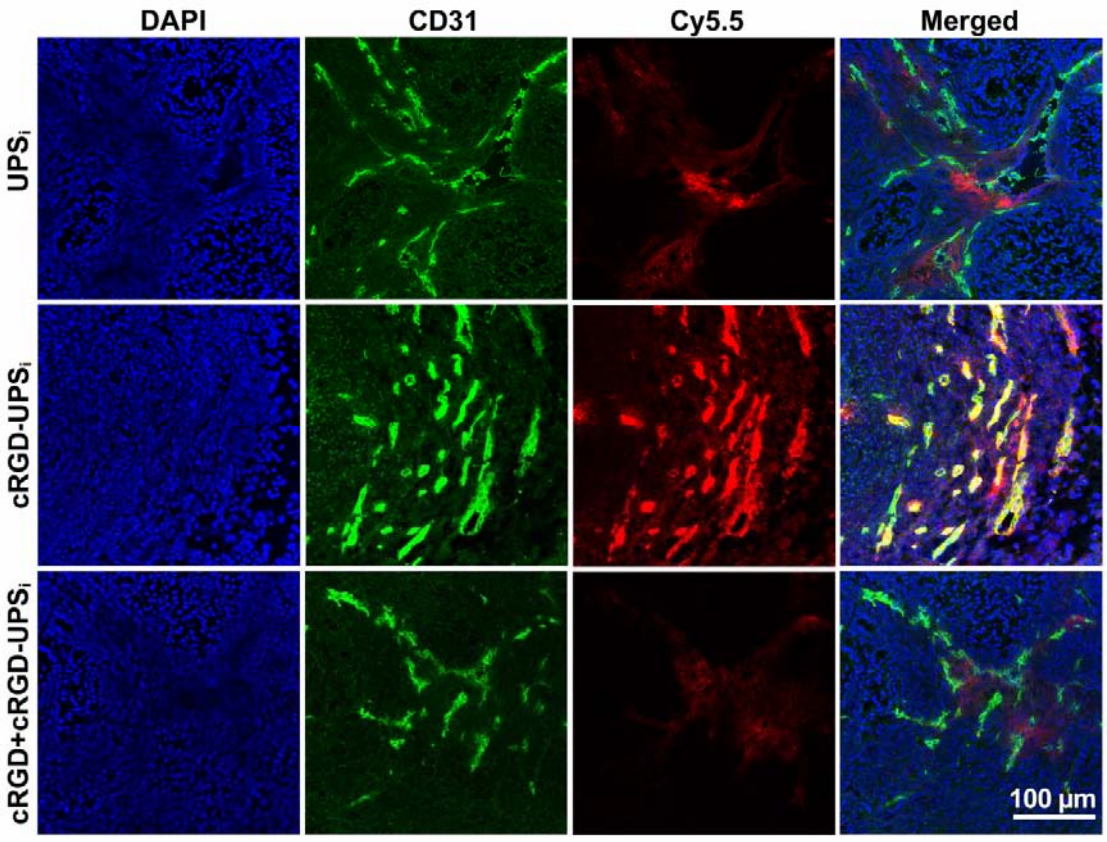

Supplementary Figure S16. Microscopy analysis of cRGD-UPS_i nanoprobes homing and activation in tumor vasculature. Tumor tissue sections from UPS_i group and cRGD-UPS_i group (6 h) were subjected to CD31 staining. Tumor vasculature staining (anti-CD31) is shown in green. The nanoprobe signal is shown in red. The cell nucleus is shown in blue. Scale bar is 100 μm.

© 2013 Macmillan Publishers Limited. All rights reserved.

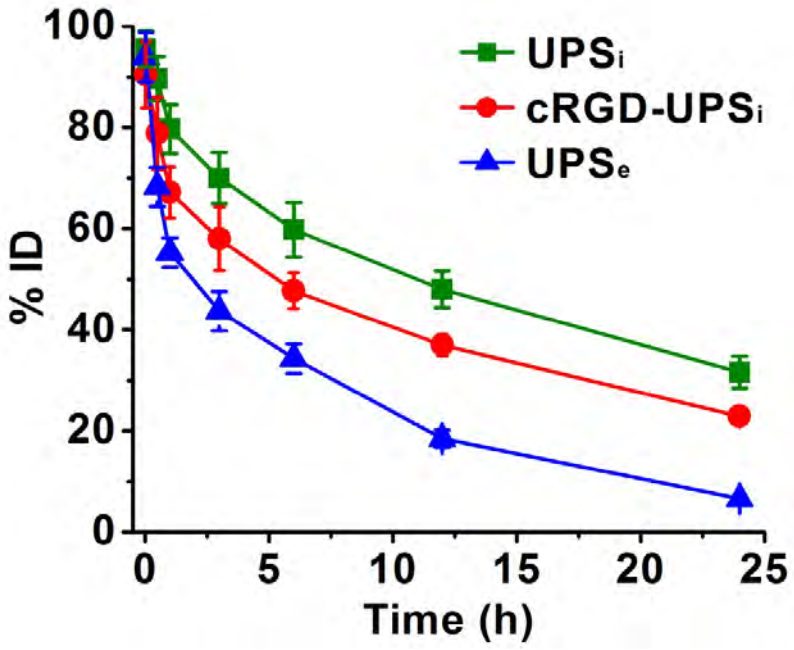

Supplementary Figure S17. *In vivo* pharmacokinetic studies of ^{3}H-labeled UPS nanoprobes in A549 tumor-bearing mice. Plasma concentration versus time curves of UPS_e, cRGD-UPS_i, and UPS_i nanoprobes (n = 4-5 per group) were obtained.

© 2013 Macmillan Publishers Limited. All rights reserved.

DOI: 10.1038/NMAT3819

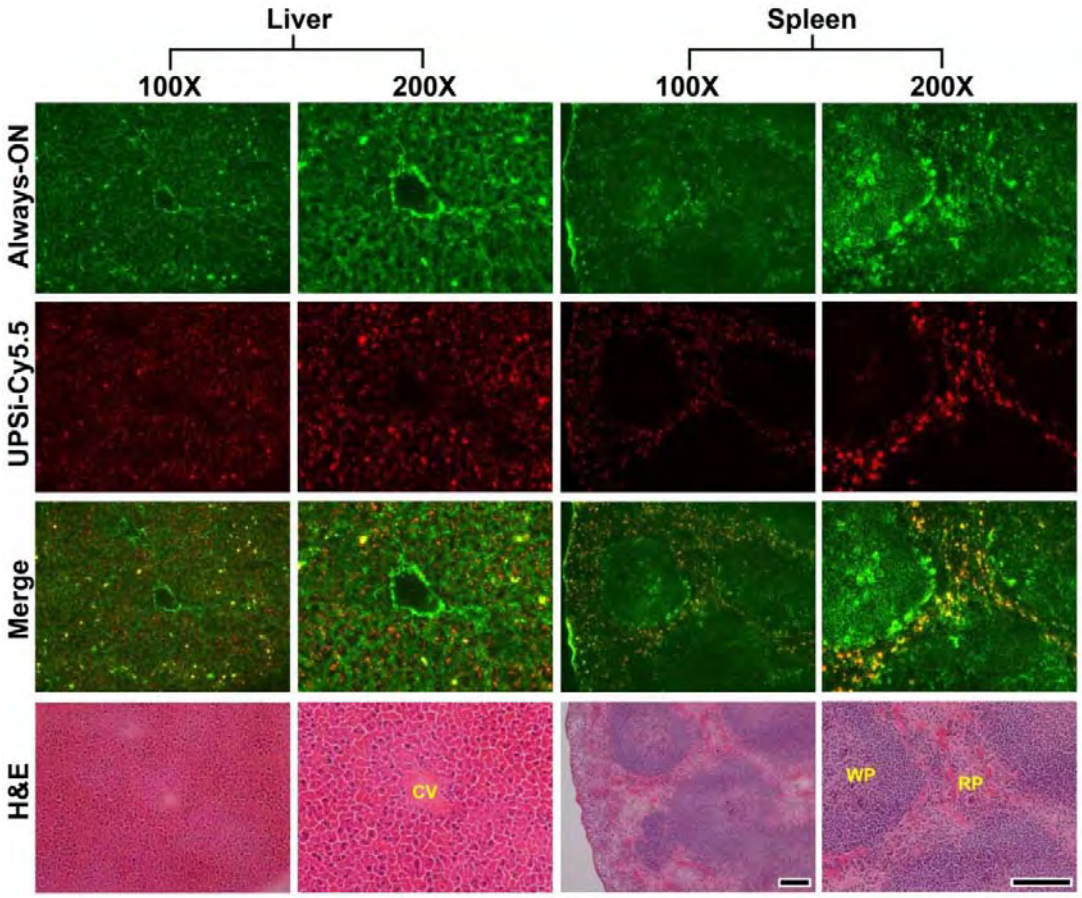

Supplementary Figure S18. Fluorescence microscopy and histology analysis of liver and spleen 6 h after co-injection of PDPA always-ON-Cy3 and UPS_i-Cy5.5 nanoprobes. The Cy3 and Cy5.5 were pseudo-colored with green and red for best illustration. The overall nanoprobe distribution was indicated by the always-ON nanoprobes, showing wide-distribution in both organs. In the liver, UPS_i activation occurred almost exclusively inside the cells (200x overlay images) with absence of signals in the extracellular space. A few high intensity spots may indicate Kupfer cells that internalized more nanoparticles. Majority of hepatocytes also took up nanoprobes, perhaps due to the relatively small size of the nanoprobes (~25 nm) and their ability to penetrate the liver fenestrae (the endothelial gap in liver sinusoids, 100-150 nm) to reach hepatocytes. The central vein (CV) in a hepatic lobule was noted in the H&E image. In the spleen, UPS_i activation occurred only sporadically in the red pulp (RP) region, which is known for the reticular mesh network and phagocytic macrophages. White pulp (WP), consisting of adenoid tissue with abundant T and B lymphocytes, is responsible for antigen processing and immune response. Lack of UPS_i activation in the white pulp may be a result of the steric shielding effect of PEG shells on the micelle surface. RP and WP were noted in the spleen H&E image. These data provide a reasonable explanation for the observed higher UPS_i signals in the liver over spleen. The scale bar is 100 μm.

© 2013 Macmillan Publishers Limited. All rights reserved.

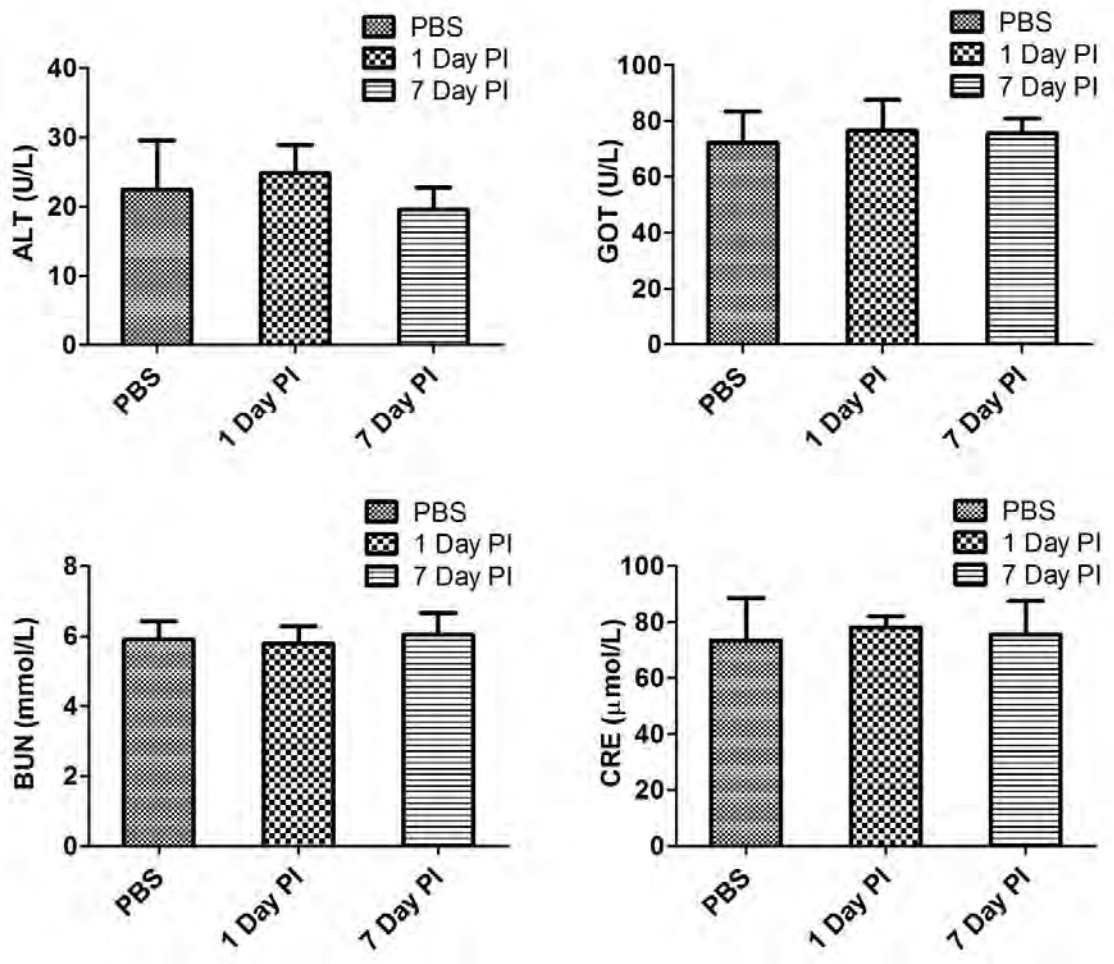

Supplementary Figure S19. Blood tests for athymic nude mice after intravenous administration of *i*UPS nanoprobes (10 mg/kg) or PBS. The results show no abnormalities in liver and kidney function over 7 day period following treatment. Data are presented as mean ± s.d. (n = 5). Abbreviations: ALT, aspartate transaminase; GOT, glutamic oxaloacetic transaminase; BUN, blood urea nitrogen; CRE, creatinine.

© 2013 Macmillan Publishers Limited. All rights reserved.

DOI: 10.1038/NMAT3819

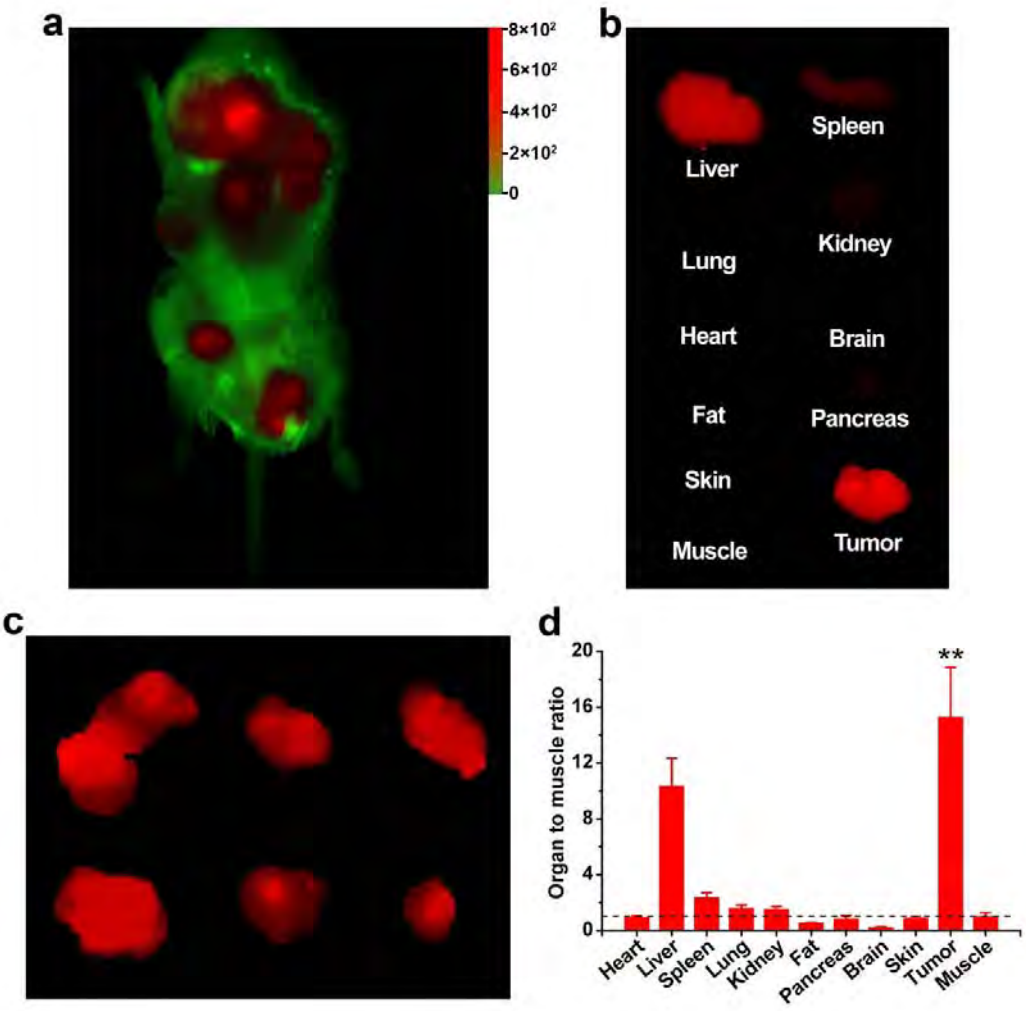

Supplementary Figure S20a. *i*UPS nanoprobes can clearly illuminate multifocal MMTV-PyMT transgenic mammary tumors with minimal background signals. (**a**) MMTV-PyMT transgenic mice bearing multiple mammary tumors were injected with a dosage of 10 mg/kg *i*UPS nanoprobe and, NIR fluorescence images at 24 h were captured using Maestro CRI imaging system. The mice autofluorescence is color-coded green while the unmixed nanoprobe signal is coded red. (**b**) At 24 h post-injection, mice were sacrificed and collected organs were visualized. (**c**) Fluorescence imaging of multiple mammary tumor nodules. (**d**) Organ to muscle ratios of fluorescence intensity at 24 h post-injection of nanoprobe. The fluorescent signal of organs was normalized to the fluorescent signal in muscle. Data are presented as mean ± s.d. (n = 4). $^{**}P < 0.01$, compared with other organs except liver.

© 2013 Macmillan Publishers Limited. All rights reserved.

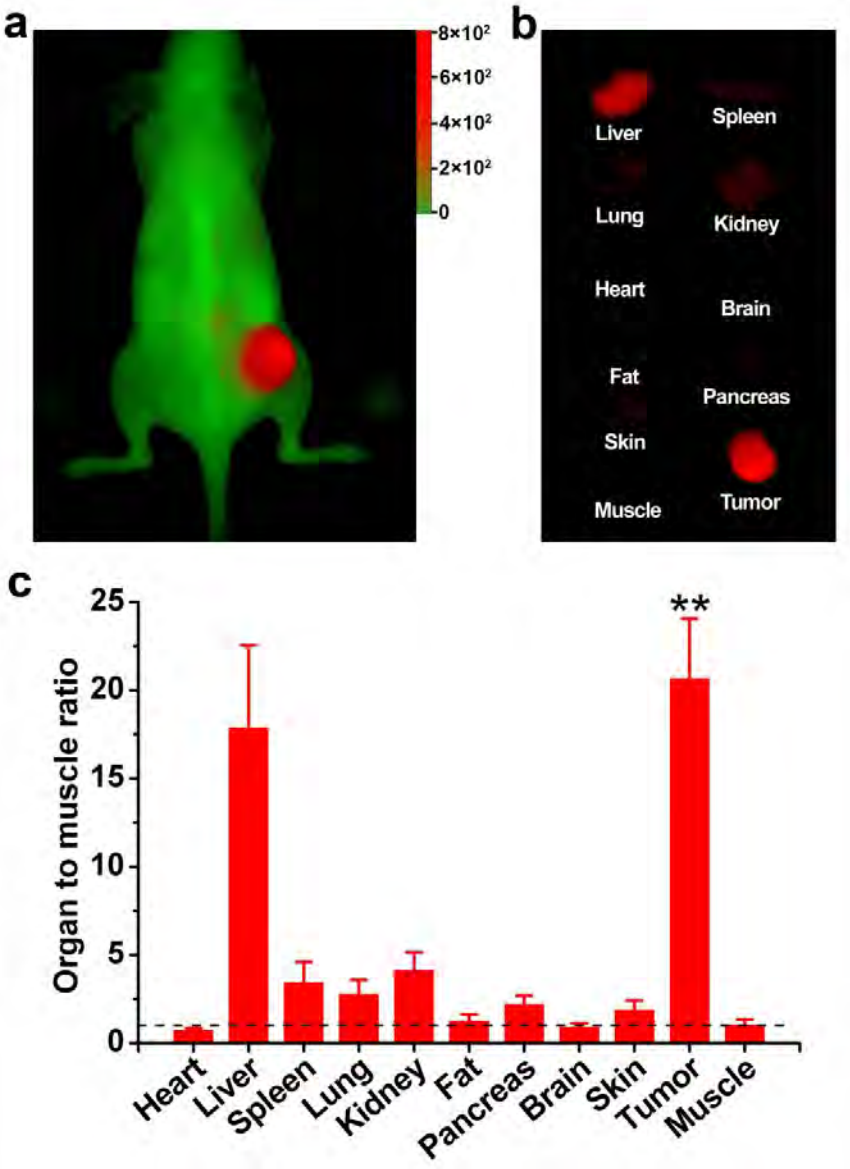

Supplementary Figure S20b. *i*UPS nanoprobes illuminate MDA-MB-231 tumor xenografts with high T/N ratio. (**a**) Nude mice bearing human MDA-MB-231 tumor xenografts were injected with a dosage of 10 mg/kg *i*UPS nanoprobe and, NIR fluorescence images at 24 h were captured using Maestro CRI imaging system. The mice autofluorescence is color coded green while the unmixed nanoprobe signal is coded red. (**b**) At 24 h post-injection, mice were sacrificed and collected organs were visualized. (**c**) Organ to muscle ratios of fluorescence intensity at 24 h post-injection of nanoprobe. The fluorescent signal of organs was normalized to the fluorescent signal in muscle. Data are presented as mean ± s.d. (n = 4). **P < 0.01, compared with other organs except liver.

© 2013 Macmillan Publishers Limited. All rights reserved.

DOI: 10.1038/NMAT3819

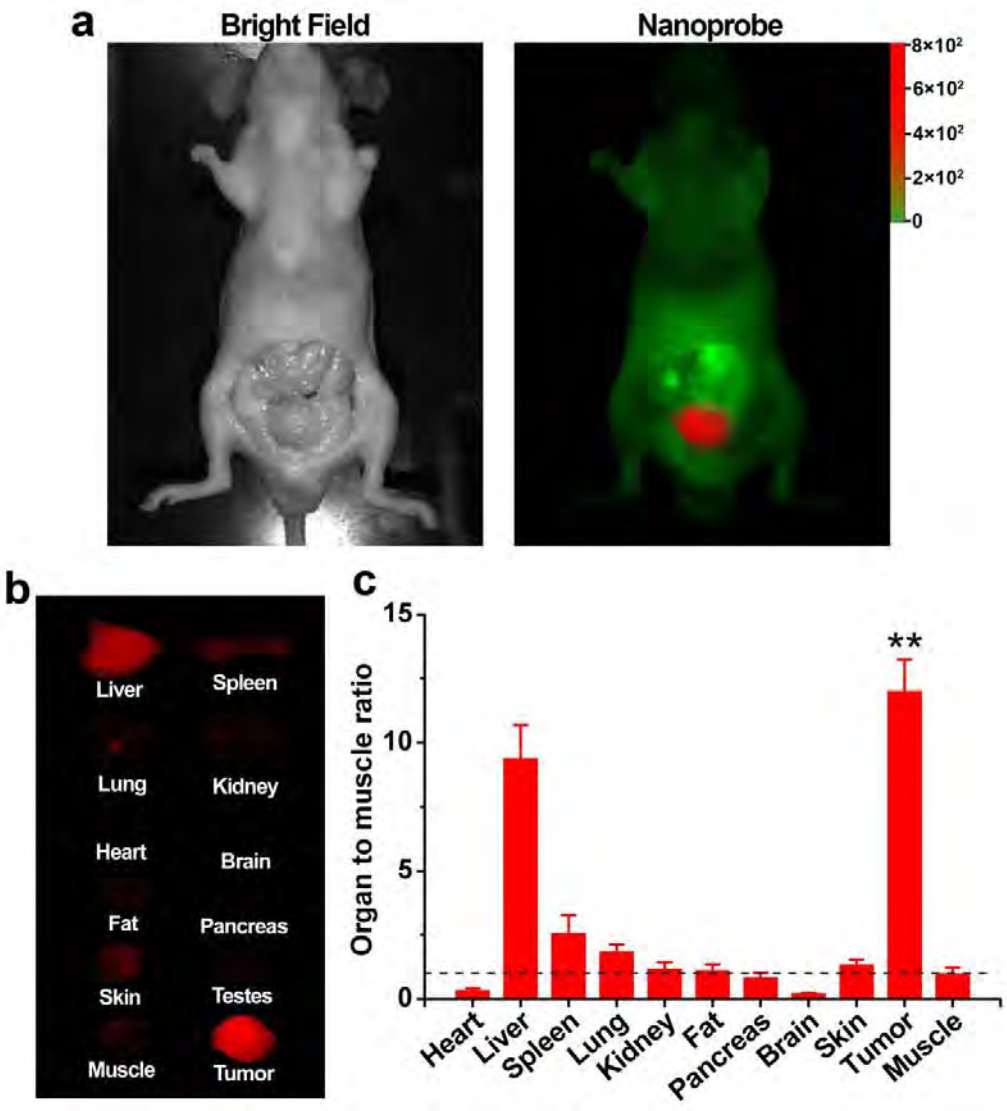

Supplementary Figure S20c. *i*UPS nanoprobes illuminate orthotopic PC-3 prostate carcinoma with high T/N contrast. (**a**) Nude mice bearing orthotopic PC-3 prostate tumors were injected with a dosage of 10 mg/kg *i*UPS nanoprobe and, NIR fluorescence images at 24 h were captured using Maestro CRI imaging system. The mice autofluorescence is color coded green while the unmixed nanoprobe signal is coded red. (**b**) At 24 h post-injection, mice were sacrificed and collected organs were visualized. (**c**) Organ to muscle ratios of fluorescence intensity at 24 h post-injection of nanoprobe. The fluorescent signal of organs was normalized to the fluorescent signal in muscle. Data are presented as mean ± s.d. (n = 4). $^{**}P < 0.01$, compared with other organs except liver.

© 2013 Macmillan Publishers Limited. All rights reserved.

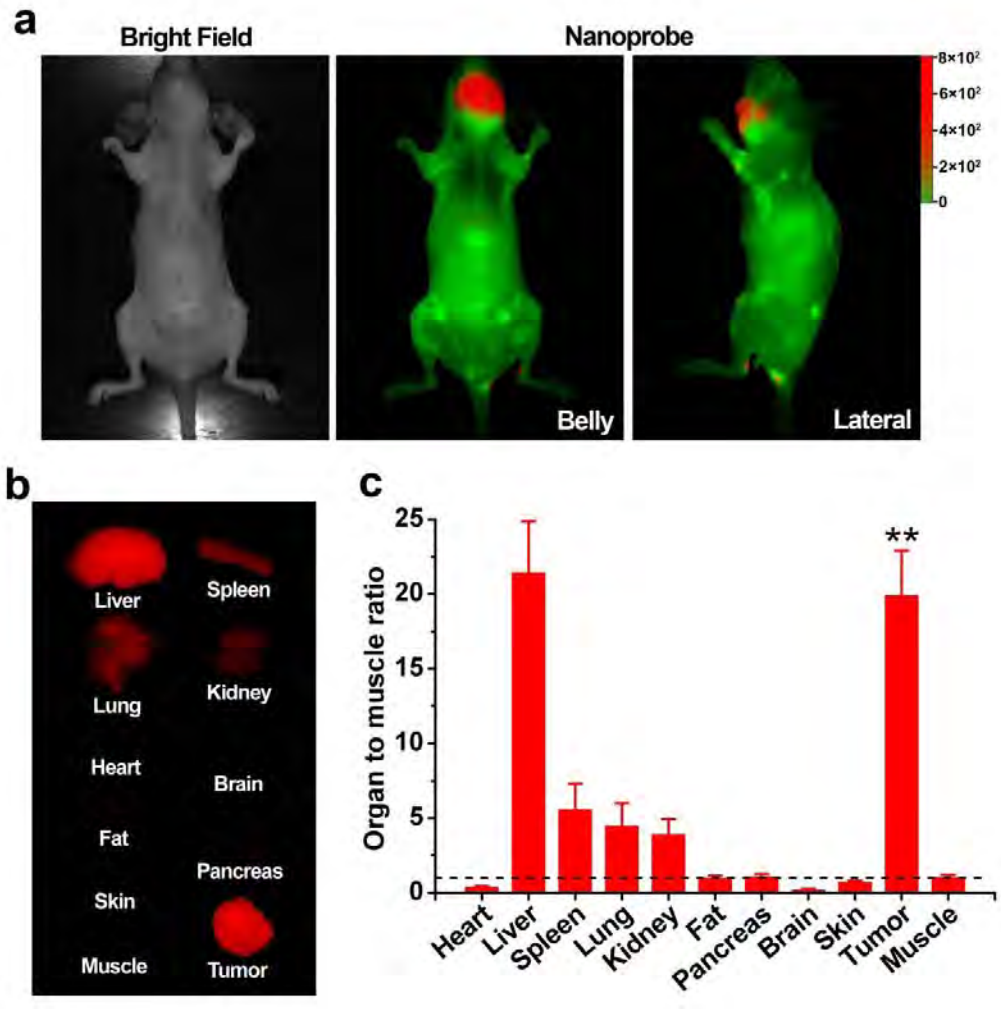

Supplementary Figure S20d. *i*UPS nanoprobes illuminate orthotopic HCC4034 head-neck tumors with high imaging contrast. (**a**) Nude mice bearing orthotopic HCC4034 head-neck tumors were injected with a dosage of 10 mg/kg *i*UPS nanoprobe and, NIR fluorescence images at 24 h were captured using Maestro CRI imaging system. The mice autofluorescence is color coded green while the unmixed nanoprobe signal is coded red. (**b**) At 24 h post-injection, mice were sacrificed and collected organs were visualized. (**c**) Organ to muscle ratios of fluorescence intensity at 24 h post-injection of nanoprobe. The fluorescent signal of organs was normalized to the fluorescent signal in muscle. Data are presented as mean ± s.d. (n = 4). **P < 0.01, compared with other organs except liver.

© 2013 Macmillan Publishers Limited. All rights reserved.

DOI: 10.1038/NMAT3819

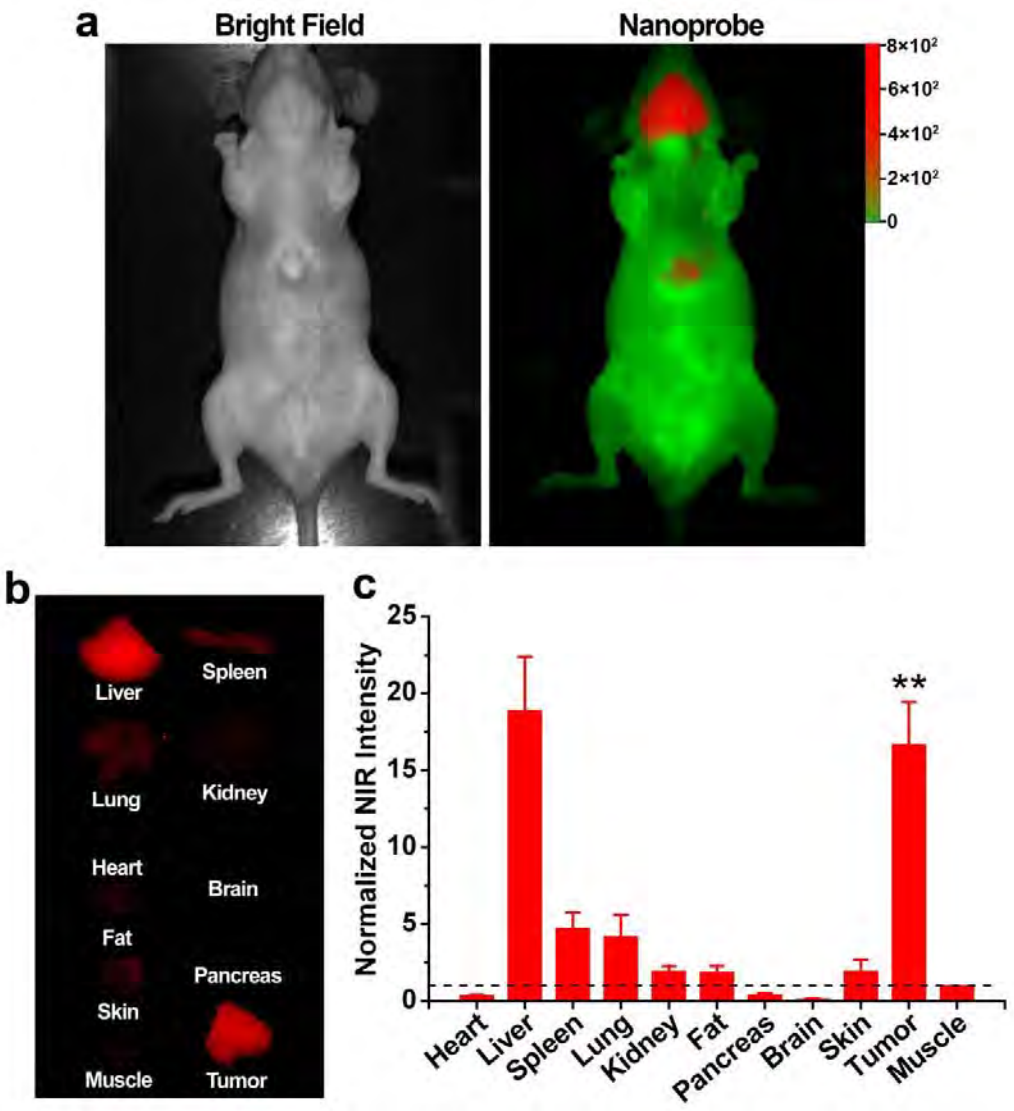

Supplementary Figure S20e. *i*UPS nanoprobes illuminate orthotopic HN5 head-neck tumors with high imaging contrast. (**a**) Nude mice bearing orthotopic HN5 head-neck carcinomas were injected with a dosage of 10 mg/kg *i*UPS nanoprobe and, NIR fluorescence images at 24 h were captured using Maestro CRI imaging system. The mice autofluorescence is color coded green while the unmixed nanoprobe signal is coded red. (**b**) At 24 h post-injection, mice were sacrificed and collected organs were visualized. (**c**) Organ to muscle ratios of fluorescence intensity at 24 h post-injection of nanoprobe. The fluorescent signal of organs was normalized to the fluorescent signal in muscle. Data are presented as mean ± s.d. (n = 4). $^{**}P < 0.01$, compared with other organs except liver.

© 2013 Macmillan Publishers Limited. All rights reserved.

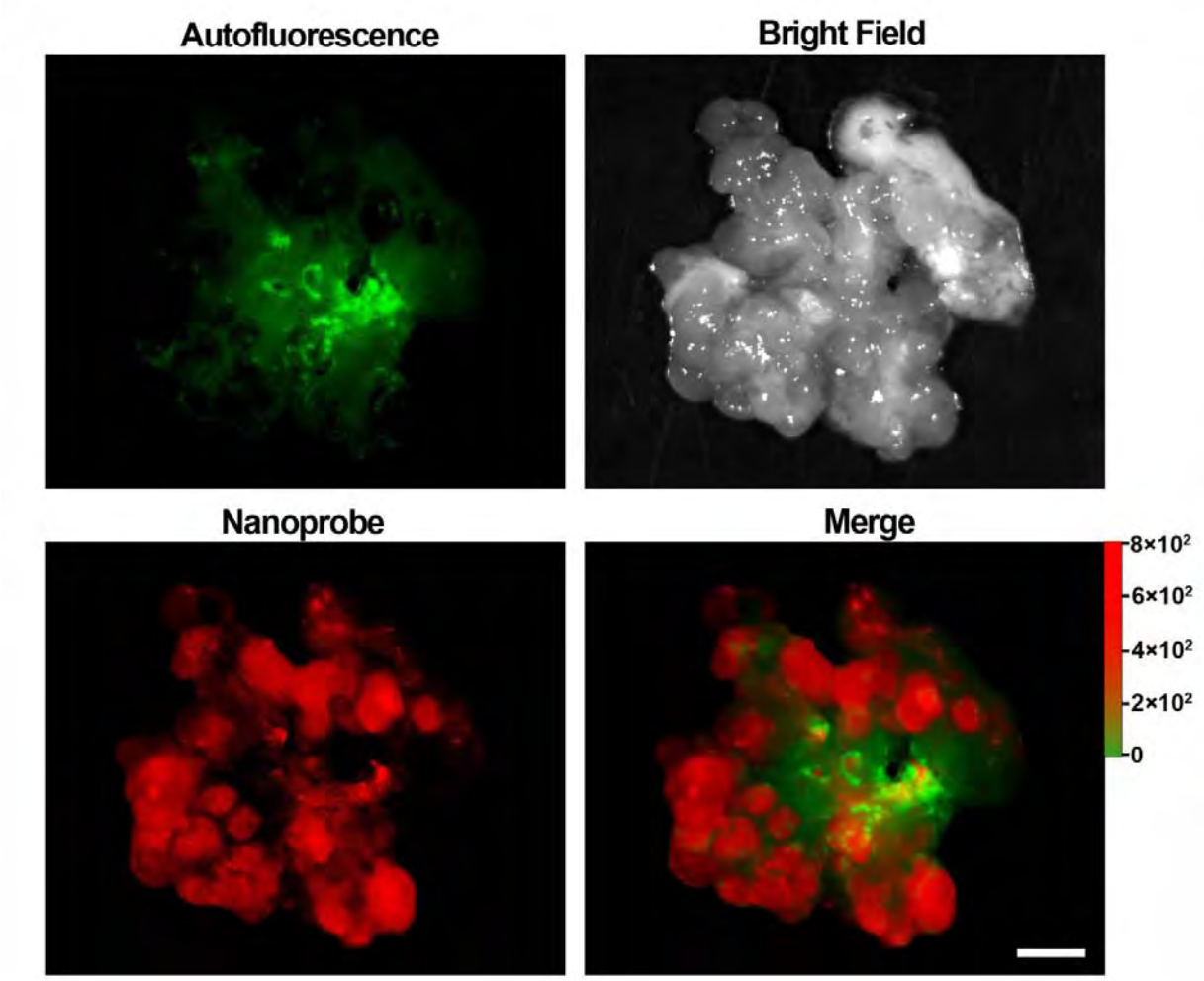

Supplementary Figure S20f. *i*UPS nanoprobes illuminate many 3LL Lewis lung cancer foci with minimal background signals. Nude mice bearing orthotopic 3LL Lewis lung cancers were injected with a dosage of 10 mg/kg cRGD-UPS_e nanoprobe and, NIR fluorescence images of excised lungs at 24 h were captured using Maestro CRI imaging system. The autofluorescence is color coded green while the unmixed nanoprobe signal is coded red. Scale bar is 2 mm. High resolution NIR images of the multiple tumor nodules (~1 mm) were visualized.

© 2013 Macmillan Publishers Limited. All rights reserved.

DOI: 10.1038/NMAT3819

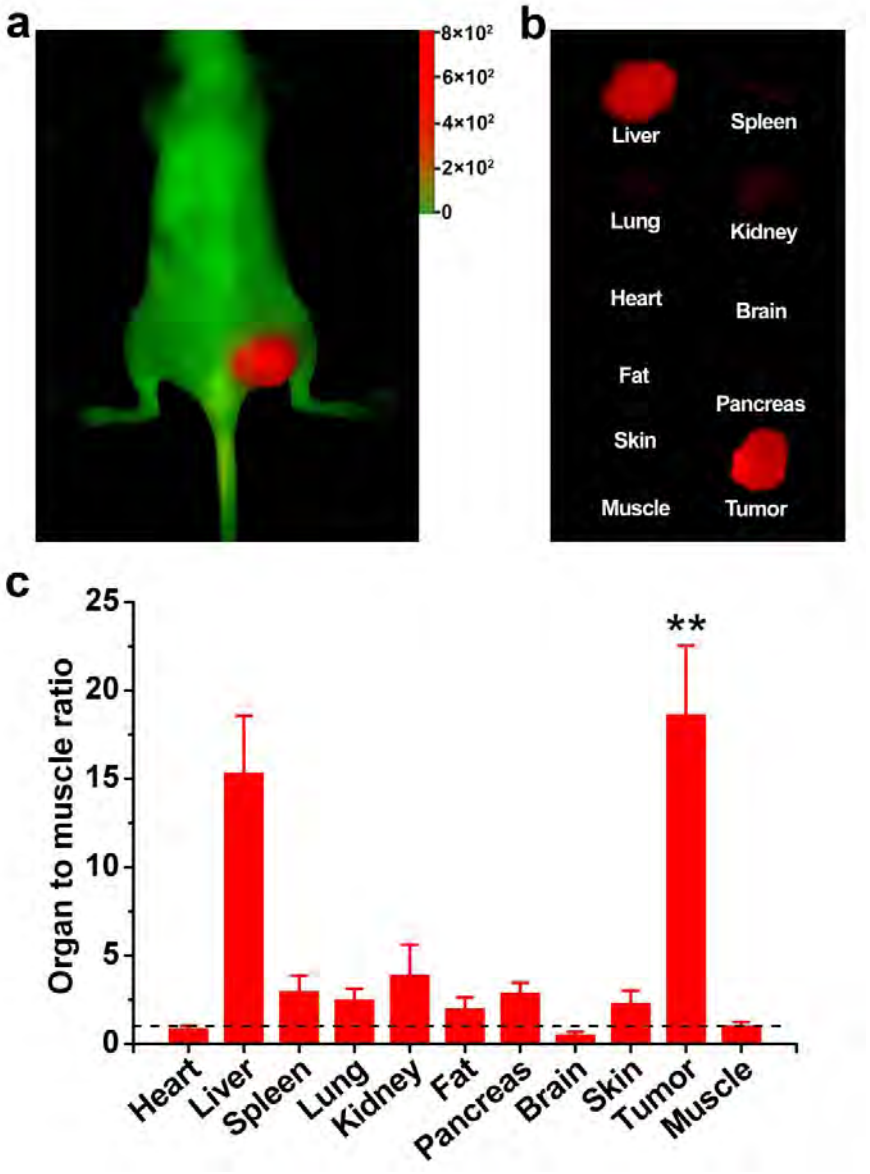

Supplementary Figure S20g. *i*UPS nanoprobes illuminate A549 lung cancer xenografts with high imaging contrast. (**a**) Nude mice bearing human A549 lung tumors were injected with a dosage of 10 mg/kg *i*UPS nanoprobe and, NIR fluorescence images at 24 h were captured using Maestro CRI imaging system. The mice autofluorescence is color coded green while the unmixed nanoprobe signal is coded red. (**b**) At 24 h post-injection, mice were sacrificed and collected organs were visualized. (**c**) Organ to muscle ratios of fluorescence intensity at 24 h post-injection of nanoprobe. The fluorescent signal of organs was normalized to the fluorescent signal in muscle. Data are presented as mean ± s.d. (n = 4). $^{**}P < 0.01$, compared with other organs except liver.

© 2013 Macmillan Publishers Limited. All rights reserved.

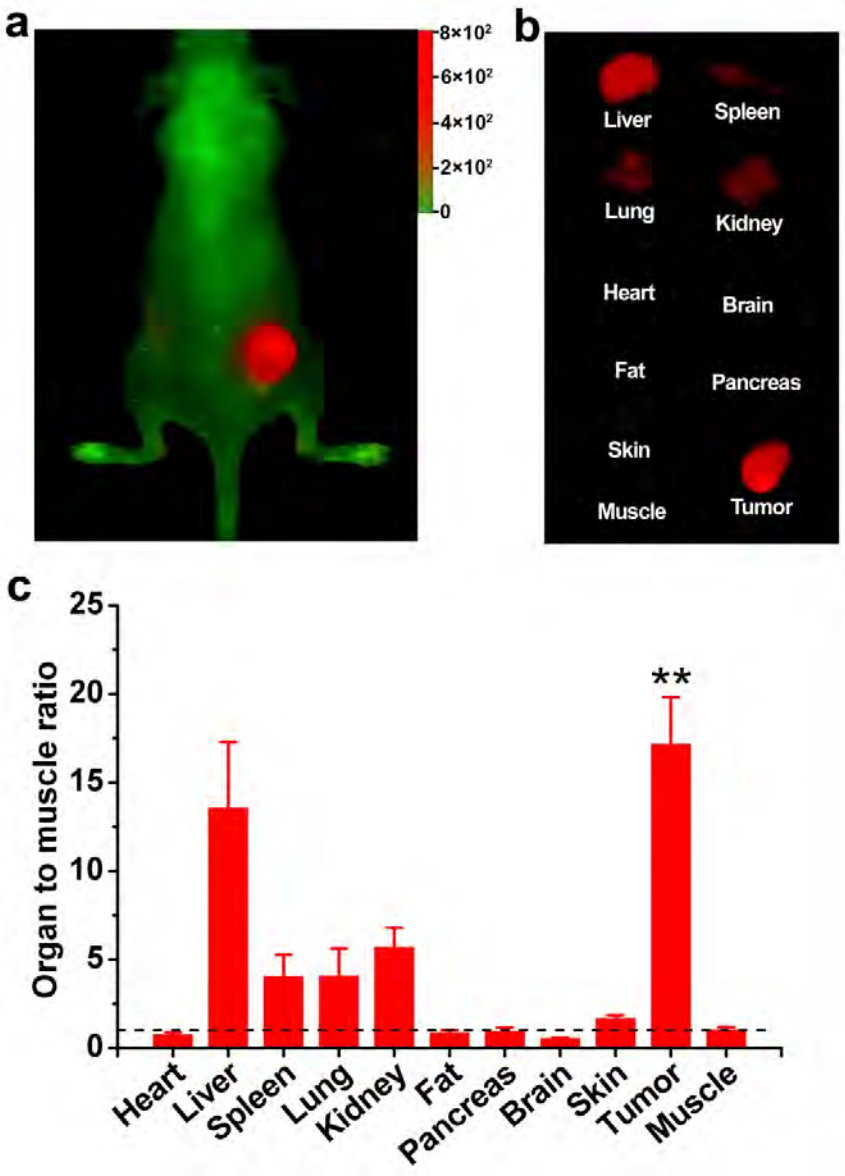

Supplementary Figure S20h. *i*UPS nanoprobes illuminate SF-188 brain cancer xenografts with high imaging contrast. (**a**) Nude mice bearing human SF-188 gliomas were injected with a dosage of 10 mg/kg *i*UPS nanoprobe and, NIR fluorescence images at 24 h were captured using Maestro CRI imaging system. The mice autofluorescence is color coded green while the unmixed nanoprobe signal is coded red. (**b**) At 24 h post-injection, mice were sacrificed and collected organs were visualized. (**c**) Organ to muscle ratios of fluorescence intensity at 24 h post-injection of nanoprobe. The fluorescent signal of organs was normalized to the fluorescent signal in muscle. Data are presented as mean ± s.d. (n = 4). $^{**}P < 0.01$, compared with other organs except liver.

© 2013 Macmillan Publishers Limited. All rights reserved.

DOI: 10.1038/NMAT3819

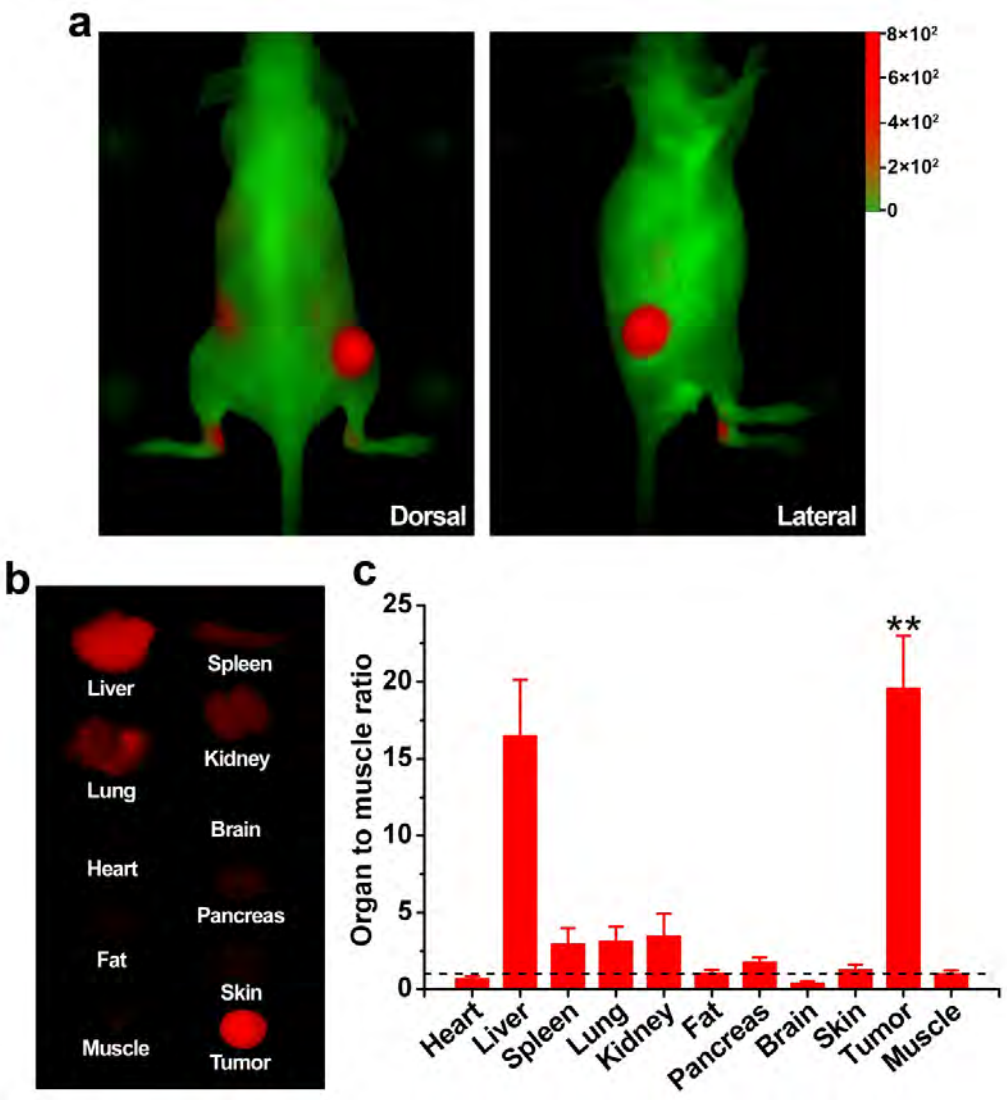

Supplementary Figure S20i. *i*UPS nanoprobes illuminate LN-229 brain cancer xenografts with high imaging contrast. (**a**) Nude mice bearing human LN-229 gliomas were injected with a dosage of 10 mg/kg *i*UPS nanoprobe and, NIR fluorescence images at 24 h were captured using Maestro CRI imaging system. The mice autofluorescence is color coded green while the unmixed nanoprobe signal is coded red. (**b**) At 24 h post-injection, mice were sacrificed and collected organs were visualized. (**c**) Organ to muscle ratios of fluorescence intensity at 24 h post-injection of nanoprobe. The fluorescent signal of organs was normalized to the fluorescent signal in muscle. Data are presented as mean ± s.d. (n = 4). $^{**}P < 0.01$, compared with other organs except liver.

© 2013 Macmillan Publishers Limited. All rights reserved.

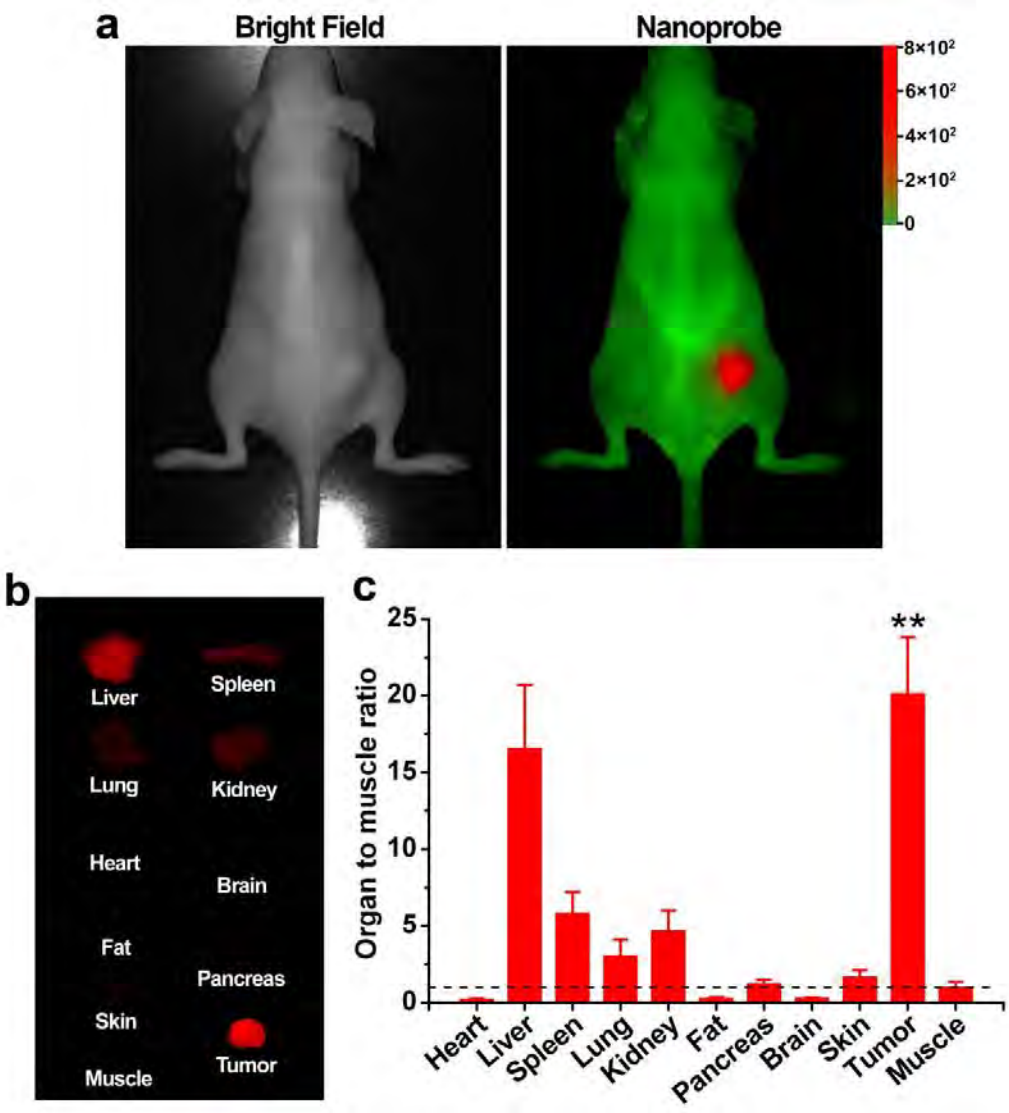

Supplementary Figure S20j. *i*UPS nanoprobes illuminate MiaPaca-2 pancreatic cancer xenografts with high imaging contrast. (**a**) Nude mice bearing human MiaPaca-2 pancreatic tumors were injected with a dosage of 10 mg/kg *i*UPS nanoprobe and, NIR fluorescence images at 24 h were captured using Maestro CRI imaging system. The mice autofluorescence is color coded green while the unmixed nanoprobe signal is coded red. (**b**) At 24 h post-injection, mice were sacrificed and collected organs were visualized. (**c**) Organ to muscle ratios of fluorescence intensity at 24 h post-injection of nanoprobe. The fluorescent signal of organs was normalized to the fluorescent signal in muscle. Data are presented as mean ± s.d. (n = 4). $^{**}P < 0.01$, compared with other organs except liver.

© 2013 Macmillan Publishers Limited. All rights reserved.